Polarimetric C-band microwave scattering from winter first-year sea ice ridges

By

Megan Shields

A Thesis submitted to the Faculty of Graduate Studies of
The University of Manitoba
in partial fulfillment of the requirements of the degree of

MASTER OF SCIENCE

Centre for Earth Observation Science
Department of Environment and Geography
University of Manitoba
Winnipeg, Canada

Abstract

Microwave scattering from sea ice ridges is poorly understood. This thesis aims to improve the current knowledge on *in situ* C-band microwave scattering from first-year sea ice (FYI) pressure ridges during winter, and how C-band backscatter can vary with changes to radar and target parameters. Remotely sensed data of ridged ice were collected at a sea ice mesocosm using a LiDAR laser scanner and a fully-polarimetric C-band scatterometer. Thesis results indicate that using an incidence angle between 30 and 50° and HV polarization will best enable distinguishing between smooth and ridged ice, while using an incidence angle of 40° and HV or HH polarization will best enable detecting variations in ridge height. Further data and analysis is needed to examine how a snow cover over a winter FYI ridge has the potential to change microwave backscatter, but it is clear that changes to the snow layer (i.e. snowfall, snow erosion, salinity content, wetness content) will affect C-band backscatter responses. Overall results indicate that a significant proportion of the variance in FYI snow-free ridge C-band backscatter can be explained by incidence angle, polarization, and ridge height, with almost 88% of the variability in backscatter attributed to ridge height.

Acknowledgments and Dedication

I would like to thank my graduate committee members Dr. Tim Papakyriakou and Dr. Paul Cooley, and especially my supervisor Dr. David Barber, for their guidance, knowledge, and ongoing support throughout the thesis process. I would like to thank the University of Manitoba Graduate Studies (UMGS), the Northern Scientific Training Program (NSTP), the Natural Sciences and Engineering Council (NSERC), the Canada Research Chairs (CRC), the Canada Excellence Research Chairs (CERC), the Canada Foundation for Innovation (CFI), and the ArcticNet Networks of Centres of Excellence for their financial support throughout this research.

I would also like to thank my family and friends, in particular Kyle, Dale, and Mary Beth, for your unwavering support throughout this process. I would like to specifically thank my colleagues Jack Landy, Kerri Warner, John Iacozza, and Randy Scharien, for their commitment and assistance with data collection in the field, and for their constant support, knowledge, and patience throughout the years.

This thesis is dedicated to Dr. Klaus Hochheim, Captain Marc Thibault, and Daniel Dubé, who tragically lost their lives pursuing Arctic science.

Table of Contents

List of Tables

List of Figures

Chapter One – Introduction

This M.Sc. thesis presents unique microwave remote sensing data of ridged sea ice collected at a sea ice mesocosm. The primary goal of this thesis is to better understand *in situ* C-band microwave scattering from first-year sea ice (FYI) pressure ridges during winter, and how C-band backscatter can vary with changes to radar and target parameters.

1.1 Rationale and Context

Over the last several decades there have been significant changes to the Arctic sea ice cover, thickness, volume, and extent, due to increased temperatures in the Arctic from an amplification of climate change consequences, such as the ice-albedo feedback effect (Comiso and Hall, 2014). Between 1979 and 2007 the summer sea ice extent decreased more than 10% per decade, which has resulted in a shift from a predominantly multiyear ice pack, to a predominantly FYI pack (Comiso, 2002; Comiso and Hall, 2014; Johannessen et al., 1999; Stroeve et al., 2012). This decline in multiyear ice has resulted in a substantial loss of ice volume and thickness throughout the Arctic ice pack (Kwok et al., 2009).

Interest in Arctic sea ice has increasingly grown in recent years, due to amplifications in global warming signatures, a reduced sea ice cover, and an increase in activities in sea ice, such as offshore exploration and drilling, and ship traffic. This increase in open water has lead to a more dynamic Arctic Ocean, and the potential for the increased creation of rubble ice and sea ice ridges. FYI ridges are important features in regards to marine transportation and navigation, climatological studies, offshore

exploration and exploitation, indigenous uses, and monitoring oil spills in sea ice. Activities in ice prefer to operate in areas of open water or thin ice, and to avoid potentially unmanageable rough ice features, such as icebergs, multiyear ice floes, and ridges (Carlstrom, 1995). Identifying and understanding areas of deformed ice, such as ridges, is necessary for navigating ships and for protecting cold ocean infrastructure.

Studying Arctic FYI ridges *in situ* is inhibited by a number of factors, including extreme weather conditions and instrumentation issues in these conditions, transportation to remote locations, and limited sunlight during parts of the year (Comiso and Hall, 2014). This is especially complicated in rubble fields that contain areas of ridging, as ships and snowmobiles will not be able to reach these locations the majority of the year due to thick ice conditions and extreme surface roughness. Using radar remote sensing to identify and understand ice ridging is a cost and time effective way to do so. In particular, using synthetic aperture radar (SAR) microwave satellite data (acquires surface data in any weather and illumination conditions) to acquire information about Arctic sea ice provides a high temporal and precise record of sea ice changes, trends, and variability (Comiso and Hall, 2014). Using smaller-scale *in situ* microwave remote sensing data provides higher resolution results than satellite data, which can be scaled to satellite resolution to increase understanding of SAR results. There have been a substantial number of sea ice microwave remote sensing studies completed that examine ridge detection from other ice types, but no studies have examined how microwave backscatter from ridges varies with changes to ridge and radar parameters, such as incidence angle, polarization, ridge height, and snow cover. The rapidly occurring changes to Arctic sea ice, and the increased potential for ridged ice features deemed

hazardous to navigation and exploration has increased the need for a better understanding of ridge features in microwave remote sensing data.

1.2 Thesis Objectives

This thesis aims to increase knowledge and understanding of C-band microwave scattering from FYI ridges. A C-Band scatterometer and LiDAR laser scanner were used to examine microwave ridge scattering at the Sea-ice Environmental Research Facility (SERF) on the University of Manitoba campus in Winnipeg, Manitoba, Canada during winter 2013-2014. Complimentary data were used from the 2012 Arctic Ice-Covered Ecosystem in a Rapidly Changing Environment (Arctic-ICE) project in the Resolute Passage, Nunavut, Canada, and the 2014 Ice Covered Ecosystem – CAMbridge bay Process Studies (ICE-CAMPS) project in Dease Strait, Nunavut, Canada. The thesis focuses on the following two research objectives:

1. To examine the relative contribution of C-band microwave scatterometer parameters (incidence angle, and linear and polarimetric parameters) relative to variable target parameters (ridge height, surface roughness, slope values, approximate air space volumes in bare ice ridges, and snow cover) on the overall backscatter of first-year ridged sea ice.
2. To determine the optimal backscatter parameter, incidence angle, and polarization, for identifying ridged ice from smooth ice, and for detecting variations in ridge height.

1.3 Thesis Outline

This thesis is written sandwich style in five chapters. Chapter one introduces the thesis objectives and rationale, and provides an outline for each chapter. Chapter two is a literature review that provides background on thermodynamic and dynamic processes of FYI, current methods of measuring sea ice surface roughness, microwave remote sensing, microwave backscatter from FYI ridges, and descriptions of the major instrumentation used for this thesis.

Chapter three is a paper titled *Polarimetric C-band microwave scattering from artificial winter first-year sea ice ridges with no snow cover*, written by Shields et al. (2015). This manuscript was submitted to the International Journal of Remote Sensing in April 2015 and is currently under review. This paper uses *in situ* data from SERF to examine C-band microwave backscatter of non-snow covered artificial FYI ridges. In this paper we (1) determine the optimal backscatter parameter, incidence angle, and polarization, for identifying non-snow covered ridged ice from smooth ice, and for detecting variations in non-snow covered ridge height; (2) examine the relative contribution of C-band microwave scatterometer parameters (incidence angle, and linear and polarimetric parameters) relative to variable target parameters (ridge height, surface roughness, slope values, and approximate air space volumes in the bare ice ridges) on the overall backscatter of first-year non-snow covered ridged sea ice.

Chapter four is titled *A remote sensing examination of snow cover over first-year sea ice ridges*. This chapter uses field data from Dease Strait (part of the ICE-CAMPS project) and the Resolute Passage (part of the Arctic-ICE project), and *in situ* data from SERF to examine snow cover over FYI ridges, and C-band microwave backscatter from

the snow layer. This chapter examines (1) snow accumulation and drifting in areas containing surface roughness features such as ridges; (2) satellite derived C-band backscatter variability throughout the Arctic melt season; and (3) how salinity content in a snow cover can change *in situ* C-band backscatter from FYI ridges.

Chapter five summarizes the thesis and the main results and conclusions are presented. Future recommendations on microwave scattering from FYI ridges that build on the findings of this thesis are discussed.

Chapter One References

Carlstrom A. (1995). Modelling microwave backscattering from sea ice for synthetic-aperture radar applications. *Chalmers University of Technology*, Technical Report 271: 1-23.

Comiso J.C. (2002). A rapidly declining perennial sea ice cover in the Arctic. *Geophysical Research Letters*, 29 (20): 17-1 – 17-4.

Comiso J.C. and Hall D.K. (2014). Climate trends in the Arctic as observed from space. *Climate Change*, 5: 389-409.

Johannessen O.M., Shalina E.V., and Miles M.W. (1999). Satellite evidence for an Arctic sea ice cover in transformation. *Science*, 286 (5446): 1937–1939.

Kwok R., Cunningham G.F., Wensnahan M., Rigor I., Zwally H.J., and Yi D. (2009). Thinning and volume loss of the Arctic Ocean sea ice cover: 2003-2008. *Journal of Geophysical Research*, 114: C07005.

Stroeve J.C., Serreze M.C., Holland M.M., Kay J.E., Malanik J., and Barrett A.P. (2012). The Arctic's rapidly shrinking sea ice cover: a research synthesis. *Climate Change*, 110 (3-4): 1005-1027.

Chapter Two – Literature Review

2.1 First-Year Sea Ice Thermodynamic and Dynamic Processes

The Arctic Ocean varies thermodynamically, creating a seasonal cycle of first-year sea ice (FYI). Ice formation occurs in the fall (usually late September) when ocean temperatures drop below the salt water freezing temperature (-1.86°C). In calm water and wind conditions small discs of ice form called frazil ice, which grow laterally. These frazil ice discs then freeze together to form a continuous sheet of ice, called nilas ice. In rough water conditions (turbulent ocean and/or strong winds) frazil or grease ice forms, but is kept in constant motion, which creates a dense suspension of frazil ice that forms round lateral slush cakes called pancake ice. These individual pancake ice floes continue to grow as frazil ice continuously suspends and attaches itself to the pancake edges. These pancake floes may also freeze together creating consolidated pancake ice. Sea ice formed in rough conditions has a greater thickness and surface and bottom roughness than ice formed in calm conditions (Petrich and Eicken, 2010).

Sea ice formed in both calm and rough conditions eventually consolidates into a coherent sea ice layer, which is when thermodynamic congelation ice growth occurs (Weeks and Ackley, 1986). Congelation ice growth is the process of water molecules freezing to the bottom of the existing ice sheet, growing the ice vertically down the water column. At the top of FYI, the ice crystals are randomly oriented, while down the ice column the ice becomes columnar (composed of vertical columnar ice crystals). During ice growth, brine is rejected from the ice sheet and then trapped in dendrites (vertically branching ice crystals) that form at the ice-water interface. Figure 2.1 summarizes ice growth and shows typical temperature and salinity profiles for winter FYI. The randomly

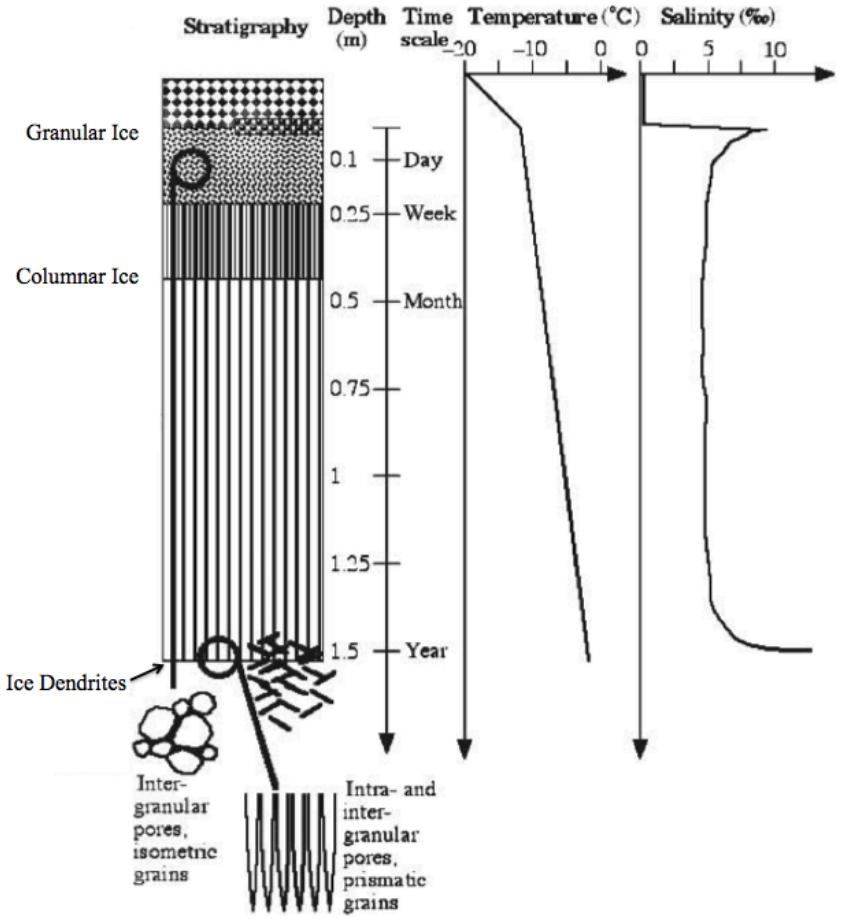

Figure 2.1. Ice growth and stratigraphy summary (modified from Petrich and Eicken, 2010). Typical temperature and salinity profiles for winter FYI are shown.

oriented ice crystals at the top of the ice, the columnar ice through the ice profile, and the dendrite ice crystals at the bottom of the ice are apparent in the stratigraphy schematic. Ice continues to grow and snow accumulates at the ice surface throughout the Arctic winter. Ice with a thicker snow cover grows more slowly than ice with a thinner snow cover, due to the insulating properties of snow, which decreases the amount of sensible heat loss from the ocean (Barry, 1996; Grenfell and Maykut, 1977; Haas, 2010). As ocean temperatures continue to drop throughout the winter, the brine-ice-salt ratio of the ice changes. Figure 2.2 is a phase diagram of sea ice for a closed volume of seawater (34 psu), which highlights phase relations within the sea ice profile. This figure shows that

as temperature continues to decrease, the mass ice fraction increases, and the mass brine fraction decreases (assuming thermodynamic equilibrium) (Petrich and Eicken, 2010). The salinity of FYI is determined by the fraction of pure ice, salts, brine, and air (Anderson, 1958). The constituents of sea ice are constantly changing and evolving temporally.

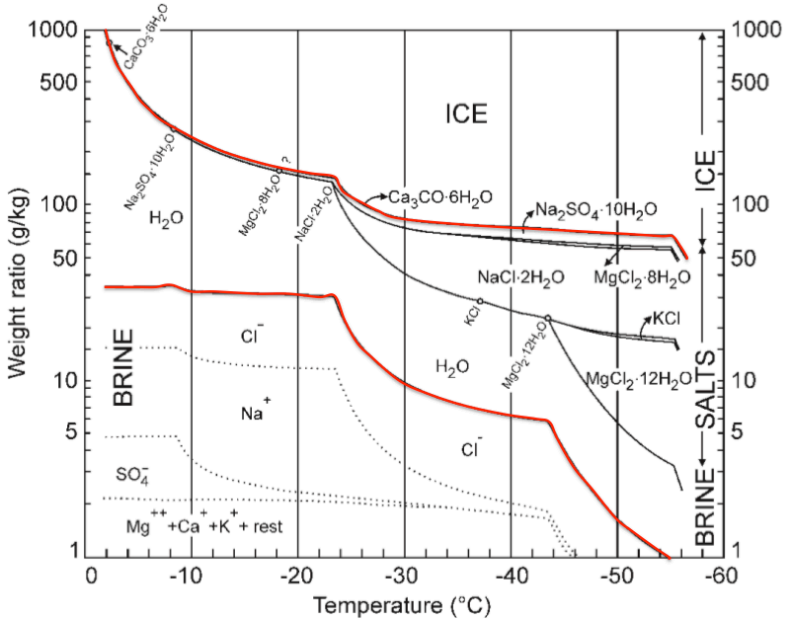

Figure 2.2. Phase diagram of sea ice for standard seawater in a closed volume where the mass fractions of all components are constant (modified from Assur, 1960). The curves represent the mass fraction of ice, salt, and liquid brine, with decreasing temperature.

When atmospheric temperatures rise above freezing in the spring, FYI has almost reached its maximum thickness, and the Arctic melt season begins. As the surface energy budget becomes positive, the snow on the surface begins to melt and pool, creating a network of melt ponds on the ice surface (Haas, 2010). These melt ponds continue to pool wider at the surface and deeper through the ice column, and in some cases right through the ice profile creating a melt (or thaw) hole. The majority of these melt pools eventually drain through thaw holes or leads in the ice. As the ice continues to warm

throughout the melt season, the permeability of the ice increases and the brine channels in the ice enlarge, creating passages for brine to be flushed from within the ice into the ocean below. Surface melt water drains into the ocean through these brine drainage channels, flushing the ice of the majority of its salinity content. The salinity of FYI decreases as ice ages, as demonstrated by Figure 2.3. Melt rates of sea ice vary with the thickness of the ice. Melt ponds form on topographic low-lying areas, and once formed, reduce surface albedo and absorb more energy than snow or ice, creating higher melt rates. In the case of ridged ice, melt rates are faster compared to level ice, due to a decreased heat flux through the ice, resulting from the greater ice thickness. Ridge keels can also increase upward turbulent fluxes of heat and reach much deeper through the water column (into warmer water). Another contributing factor to increased melt rates over ridges is the fact that the ridge sails are more directly exposed to the low incident solar radiation in the Arctic (Haas, 2010).

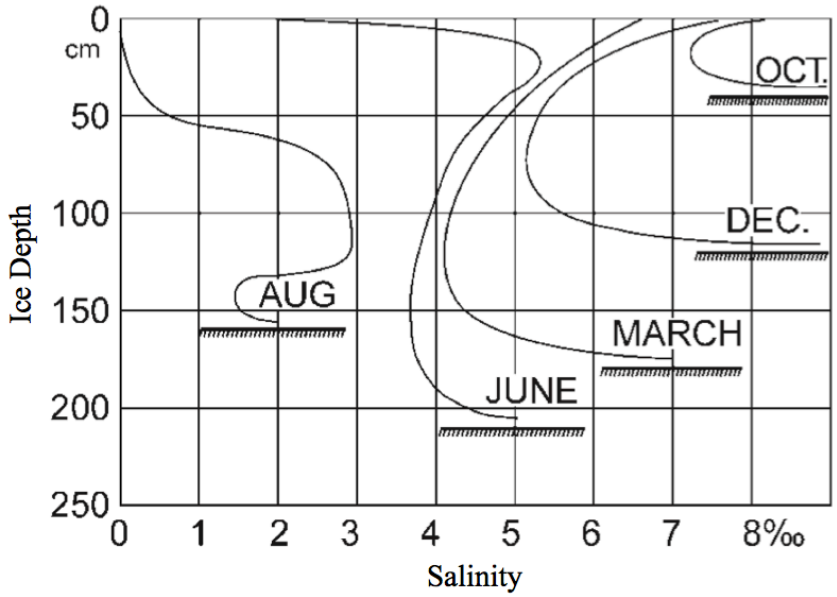

Figure 2.3. The temporal change of the C-shape salinity profiles of FYI (modified from Malmgren, 1927). The salinity content of sea ice is significantly reduced during the Arctic melt season, due to freshwater flushing from the surface and drainage of brine.

The various dynamic processes occurring across the Arctic Ocean can create significant ice topography. Ice is subject to ocean currents and atmospheric wind conditions, which can break apart ice into individual floes, separated by open water leads. These ice floes can then be forced together due to varying drift paths and speeds. When the force of floe compression becomes too large for the ice to handle, the floes crash together and sea ice pressure ridges are formed (Haas, 2010). Figure 2.4 is an illustration depicting dynamic processes that change ice thickness, such as ridge formation. Ice ridges are found in the oceans at both poles, but a significant amount more are found in the Arctic (Carsey et al., 1992).

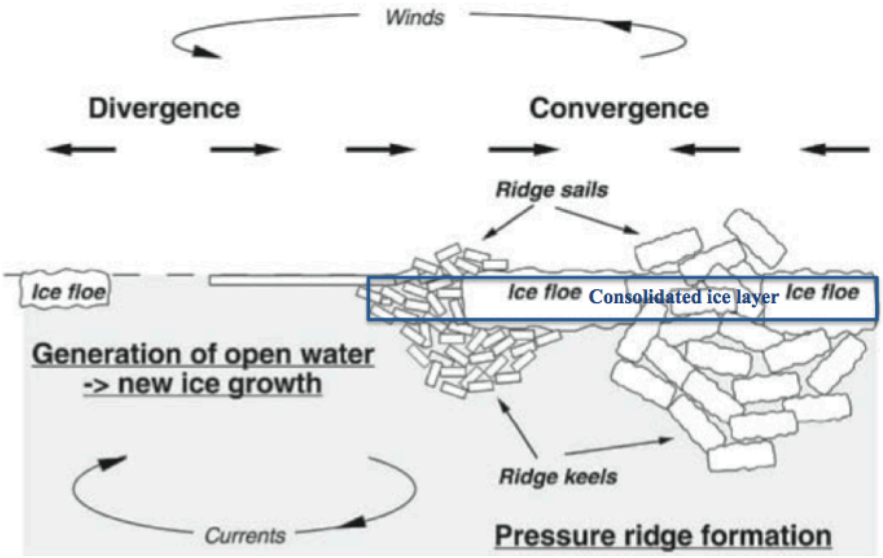

Figure 2.4. Illustration demonstrating the dynamic processes that can alter ice thickness (modified from Haas, 2010).

FYI pressure ridges form in ice that melts out each summer and reforms each fall, when relatively smooth floes of ice are compressed together by environmental driving forces, such as ocean currents and winds. When these floes are compressed and sheared together, a ridge builds up above and below the level ice surface due to a combination of crashing, bending and buckling failures. The compression of the ice floes results in

numerous ice blocks, which are usually the same thicknesses as the converging ice floes, to be piled above and below the surface, creating an ice ridge (Timco et al., 2000; Tucker et al., 1984). These ice blocks form in a linear pattern surrounded by undeformed, or slightly deformed, ice (Hudier and Larouche, 2005). Usually the middle portion of the ridge (along the water line) is re-frozen together, creating a consolidated layer of ice. In general, the sail of the ridge (the rubble ice above the water line) is one-tenth the volume of the keel of the ridge (the rubble ice below the water line). These FYI ridges are usually elongated linear features that can extend for hundreds of metres, with widths up to ten metres, and heights up to several metres (Haas et al., 1999; Timco et al., 2000; Wadhams, 2000). In areas of high convergence and compression, ridges and deformed ice can form close together, creating rubble (or ridged) ice fields (Lensu, 2003). The degree of deformation of the ice depends on the atmospheric and oceanic compressions at the surface during the time of formation (Haas et al., 1999).

The ice blocks that make up FYI ridges are angular and not uniformly oriented, which creates significant airspace between blocks on the surface that become filled with hardened, compacted snow over time due to wind. There is often a thick snow cover on the leeward side of ridges due to drifting (Carsey et al., 1992). These snowdrifts become compacted over time due to wind and weathering, creating linear snow dunes called sastrugi (Armstrong et al., 1973). Ringed seals hollow out these snow dunes as lairs in order to protect young pups from predators. In many parts of the Arctic, ringed seals make up the main diet of polar bears, and so these regions of deformed ice and ridging are ideal habitat spaces for ringed seals and polar bears (Hudier, 2006; Lensu, 2003), as well as ideal hunting locations for indigenous populations.

The ridging and rafting process creates a deformation energy sink that significantly modifies the roughness characteristics of the ice surface (Li et al., 1998). Deformed sea ice plays an important role in climate and ocean circulation models. The size, orientation, and density of ridges are significant in determining heat and momentum fluxes, and can change the fluid flow pattern and conditions at the sea ice-ocean interface (Hudier, 2006). The dynamic forces that create these ridge features, create much thicker ice above and below the surface than would normally be created through natural thermodynamic processes alone (Lubin and Massom, 2006). This gives these ridge features a substantial role in determining the amount of hydrodynamic and aerodynamic coupling between the ice, ocean, and atmosphere (Garbrecht et al., 1999; Launiainen and Vihma, 1994; Li et al., 1998; Mai et al., 1996; Vihma et al., 2003). The surface roughness of sea ice is significant in terms of determining ice dynamics, ice drift, ice deformation, and the ice thickness distribution throughout the Arctic (Lubin and Massom, 2006).

2.2 Current Measurement Methods of Sea Ice Roughness

Currently, the most common method of measuring sea ice roughness is using ice thickness measurements or estimates to interpolate surface roughness. There are several ways to measure ice thickness, the main ones of which are highlighted here.

The most direct way to measure ice thickness is to drill holes through the ice and measure *in situ*, however this method has very low spatial resolution as thickness can significantly vary locally. Another *in situ* method of measuring ice thickness is to image or video broken floes of ice as an icebreaker goes through. Thickness can be determined

by the camera height from the surface and the length of the profile of the ice as ice fragments are turned over to their cross profile (Haas, 2010). Another method is to obtain draft estimates of sea ice using ice profiling sonar or upward-looking sonar attached to oceanographic moorings or military submarines, in order to measure small-scale thickness distributions (Melling and Riedel, 2004; Rothrock et al., 2008; Wadhams and Davis, 2000). Small pulse radar or ultrasonic sounding wavelengths can be used to measure ice thickness for relatively small areas of the Arctic. Electromagnetic induction (EMI) sounding can also be used when the electrical underground conductivity is measured, and ice thickness is then interpolated (Haas, 2010). Using sonar, EMI sounding, pulse radar, or direct *in situ* measurements of ice thickness, can only provide ice thickness distribution measurements for small, localized areas in the Arctic.

For measuring large-scale ice thickness across the Arctic Ocean, space-borne sensors can be used. Using radar and laser satellite altimetry can provide estimates of ice thickness by acquiring ice freeboard and snow surface elevation measurements (the ice thickness measurement is based on assumptions of snow thickness, and snow and ice density, so only an estimate can be produced) (Kwok et al., 2004; Laxon et al., 2003; Zwally et al., 2008). Thin versus thick ice can be distinguished using techniques that examine thermal infrared images (from thermal infrared satellites (i.e. AVHRR and MODIS) or microwave brightness temperatures (from passive microwave sensors (i.e. SSM/I)) (Haas, 2010), but exact measurements of ice thickness to interpolate surface roughness can not be calculated using this method. Using synthetic aperture radar (SAR) provides a precise way to distinguish between thin and thick ice, as well as to determine

areas of first-year and multiyear ice (Haas, 2010). The ERS and RADARSAT satellite systems are active microwave sensors that use SAR.

A precise way to measure small-scale surface roughness of sea ice is to use a laser scanning system that operates in the visible spectrum. This can provide millimetre to centimetre scale resolution of the topographic surface. Using a laser scanning system along with active microwave radar can provide detailed measurements of an ice surface (locally), which can be used along with an active microwave space-borne sensor, such as RADARSAT-2, to measure and understand surface roughness of sea ice.

2.3 Microwave Remote Sensing

Microwaves have wavelengths ranging from one millimetre to approximately one metre (this range varies based on the field of study), and frequencies that range from approximately 1 to 300 GHz (Carsey et al., 1992). Microwaves can interact with earth's surface in one of, or a combination of four ways; absorption, transmission, reflection, or scattering. Characteristics of the surface, such as surface roughness, volumetric inhomogeneity, incidence angle of the electromagnetic wave, and wavelength, determine the partitioning of energy at the surface (Parashar et al., 1977). Sea ice scatters incoming microwave energy.

When electromagnetic energy is reflected from a smooth surface, the energy is returned coherently in the specular direction. Smooth surfaces act as specular reflectors, where the incoming energy is reflected in one outgoing direction, where the angle of reflection equals the angle of incidence. When electromagnetic energy is scattered from a slightly rough surface, most of the energy is reflected coherently in the specular

direction, while some of the energy is scattered in other directions. When electromagnetic energy is scattered from a rough surface, almost all of the energy is scattered inhomogeneously in all directions, while some of this energy is scattered in the backscatter direction, which is the direction from which the energy came (Carlstrom, 1995). A rough surface is defined by the incoming wavelength and the incidence angle of the radar, compared to the height variations of the surface roughness. Rough surfaces act as diffuse reflectors, where a significant portion of the incoming energy is reflected back in the direction of the energy source. Backscatter is defined as the intensity of the energy received back from the surface target, based on the scattering characteristics of the target area. In general, smooth surfaces result in very low backscatter and produce dark radar targets, while rough surfaces result in high backscatter and produce bright radar targets (Lubin and Massom, 2006).

SAR and scatterometers are active remote sensing instruments that emit microwave pulses towards a target and then record the backscattered energy received back to the instrument (Carlstrom, 1995). These radars have the ability to transmit microwaves to a target surface, and then measure the intensity of the backscatter received by the radar as a function of the radars incidence angle, polarization, and frequency, as well as the geometric and dielectric properties of the surface, and the environmental conditions at the surface (Elachi, 1988; Lubin and Massom, 2006; Onstott et al., 1979; Ulaby et al., 1986). The backscatter received by a scatterometer (effectively an *in situ* radar) is expressed as the backscattering coefficient (σ°) in decibels (Carsey et al., 1992). The backscattering coefficient is the ratio of the power scattered (relative to isotropic, or uniform, scattering surface targets), and the estimated calibrated return power of a radar

pulse. Essentially, the backscatter coefficient is determined by the incoming and backscattered electric fields (Carlstrom, 1995). σ° is known as the scattering coefficient when examining backscatter in a SAR image (Lee and Pottier, 2009). This scattering coefficient is the averaged radar cross section per unit area, which is expressed in decibels (Richards, 2009). The radar cross section is a measure of a targets ability to reflect radar energy, defined as the cross section of a uniform scatterer that creates the same amount of scattered power density as the target in a particular direction. The radar cross section is a function of many parameters, such as wave frequency, wave polarization, and the geometric and dielectric properties of the target (Lee and Pottier, 2009). The radar cross section per unit area is used to measure backscatter from a number of different backscattering signatures in one area, the size of the area equalling one pixel in the satellite image (Carsey et al., 1992).

When microwaves interact with a target, the target can absorb a portion of the incident energy, while the rest of the energy is reradiated as a new energy wave (Lee and Pottier, 2009). There can also be volume scattering within the target before the return electromagnetic wave is released. This sub-surface scattering can occur when some of the incident wave penetrates the surface slightly, and scattering occurs within the volume of a roughness feature at the surface (i.e. for ridges, an ice block at the surface of the sail). The strength of energy scattering at the surface heavily depends on the surface roughness and the dielectric constant of the surface. The dielectric constant is a measure of the electromagnetic absorption, reflection, and scattering within a material (Morey et al., 1984). Dielectric materials cannot conduct electricity, but can transmit electric fields.

When examining volume scattering, individual scattering may occur at different dielectric discontinuities within the volume (Richards, 2009).

Polarization is also an important parameter when examining backscatter from a target. Polarization is the direction in which microwaves are emitted and received. Scattering properties of the same surface can be different for different polarizations. The polarization of a wave of energy is defined by the orientations of the magnetic and electric field vectors. The incident and scattered waves can have the same polarization (called copolarized), where microwaves are emitted and received in the same direction (either horizontally or vertically), or they can have different polarizations (called cross-polarized), where microwaves are emitted and received in opposite directions (i.e. emitted in the horizontal direction and received in the vertical direction) (Richards, 2009). There are four possible polarizations with a fully-polarimetric radar; VV, HH, HV, and VH.

SAR and scatterometers are useful for examining microwave backscatter, as they can measure scattering characteristics based on the wavelength of the radar, can detect surface roughness, and have diurnal and all weather acquisition capabilities. Space-borne imaging SAR instruments have the advantage of covering large surface areas and obtaining time series data over a long period of time, but are a disadvantage in terms of only collecting data at one frequency and limited incidence angles and polarizations (Melling, 1998; Winebrenner et al., 1998). Scatterometers have the advantage of being able to collect surface characteristics at extremely small-spatial scales, collect data of the same surface at a range of incidence angles (so that the surface can be characterized more completely), and being able to reduce the heterogeneity of the target surface (due to a

much smaller sensor footprint), but have the disadvantages of covering small surface areas and not acquiring surface images. Imaging SAR sensors measure returns from the entire area of a footprint and estimate backscatter of the entire footprint, while scatterometers provide point measurements of the target surface throughout the instrument footprint (Carsey et al., 1992). More comprehensive observations of microwave surface scattering are collected with radar scatterometers compared to satellite imagery, but resolution and coverage are not as detailed.

2.4 C-band Scatterometer

A scatterometer is a non-imaging radiometrically-calibrated instrument that measures the scattering coefficient as a function of the radar incidence angle (Carlstrom, 1995; Onstott et al., 1979). The radar incidence angle is the incident radar beam (incoming energy wave) normal to the target surface (Lubin and Massom, 2006). Scatterometers are designed to obtain accurate measurements of scattering from terrestrial and ocean surfaces (Carsey et al., 1992), by emitting electromagnetic waves towards a target using an antenna, and then receiving backscattered waves using either the same antenna or a separate one (Parashar et al., 1977; Richards, 2009). Polarimetric surface scatterometers can acquire data at high temporal resolutions with good spatial resolutions (Geldsetzer et al., 2007).

The footprint of the scatterometer antenna and the incidence angle determine how many independent samples are collected per scan. The larger the incidence angle, the more independent samples are collected, as the azimuth angle widens. A fast Fourier transform is used to process each scatterometer scan. During each scan, copolarized and

cross-polarized backscatter values are collected. Total power is calculated by adding the copolarized and cross-polarized backscatter coefficients and is a measure of the unpolarized response that would be acquired by the scatterometer. This parameter can be useful for analyzing results related to incidence angle, shadowing, or the dielectric properties of the target surface (Woodhouse, 2006). The average covariance matrix of the scattering amplitudes within a particular height scan line are used to derive polarimetric parameters, such as the depolarization ratio, the copolarized phase difference, and polarimetric ratios. The depolarization ratio is the ratio of the cross-polarized returns to both copolarized returns (Onstott, 1992). The VVHH phase difference (also called the polarimetric phase difference) is a measure of the phase difference between the two polarizations (VV and HH). Essentially this is a measure of coherence between the copolarized data. High VVHH phase difference values are representative of a high correlation between the two polarization states, while low VVHH phase difference values are representative of a low correlation between the two polarization states. HV/HH and VV/HH are polarimetric ratios that allow for the properties of the different polarizations to be emphasised, instead of the absolute backscatter intensity. These ratio parameters represent more of the geometric properties of the target, compared to the dielectric values at the surface (Woodhouse, 2006). Generally a higher HV/HH ratio means that there is more volume scattering occurring at the surface.

A fully-polarimetric C-band microwave scatterometer was used for this thesis (shown in Figure 2.5). It emits pulses with a center frequency of 5.5 GHz and a bandwidth of 500 MHz. The scan data collected were post-processed in IDL software

using a calibration file. The calibration reference file (used for the normalized radar cross-section and polarimetric parameters) was collected separately using a trihedral corner reflector placed in the antennas far field.

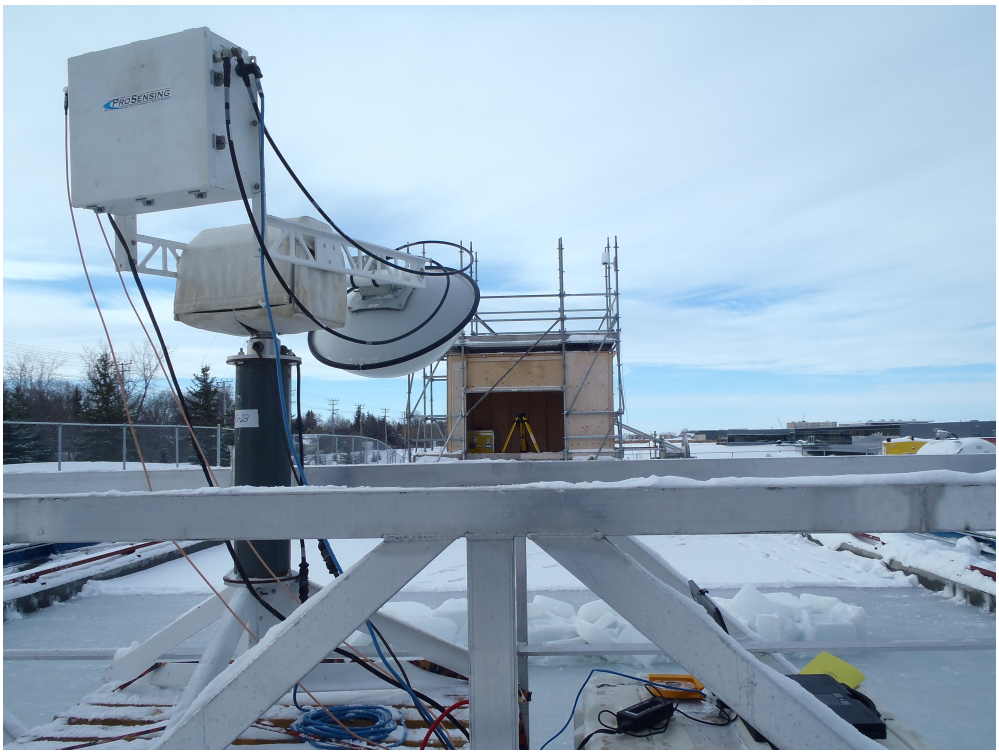

Figure 2.5. The fully-polarimetric C-band microwave scatterometer set up during the winter 2013-2014 Sea-ice Environmental Research Facility (SERF) study. The scatterometer antenna is encased in the white radar dome.

2.5 Terrestrial LiDAR Laser Scanner

LiDAR is an acronym for Light Detection and Ranging, and is an active remote sensing mapping and modeling technology that uses laser light (Renslow, 2012). A Leica ScanStation C10 discrete-pulse terrestrial laser scanner (shown in Figure 2.6) was used to scan FYI ridges from multiple sides in order to create three-dimensional (3D) digital point cloud models of each ridge. The time of flight for each laser pulse emitted by the scanner are recorded once reflected and returned to the scanner from the surfaces of

surrounding objects, creating the 3D model. The laser pulses do not penetrate snow and ice surfaces, making LiDAR an accurate tool for mapping surface topography (Landy et al., 2014). The scanner was heated in a custom-built heater case prior to scanning in order to heat it to its operational temperature. The scanner emits pulses at frequencies up to 50 kHz and at a wavelength of 532 nm. High Definition Surveying (HDS) targets were set up and collected with each scan as control points (creating an arbitrary coordinate system), so that the scans could then be meshed together to create high-resolution 3D point cloud models. The point cloud data collected were post-processed using Cyclone 9.0, Quick Terrain (QT) Modeler 7.1.6, and ArcGIS 10.2.2 software.

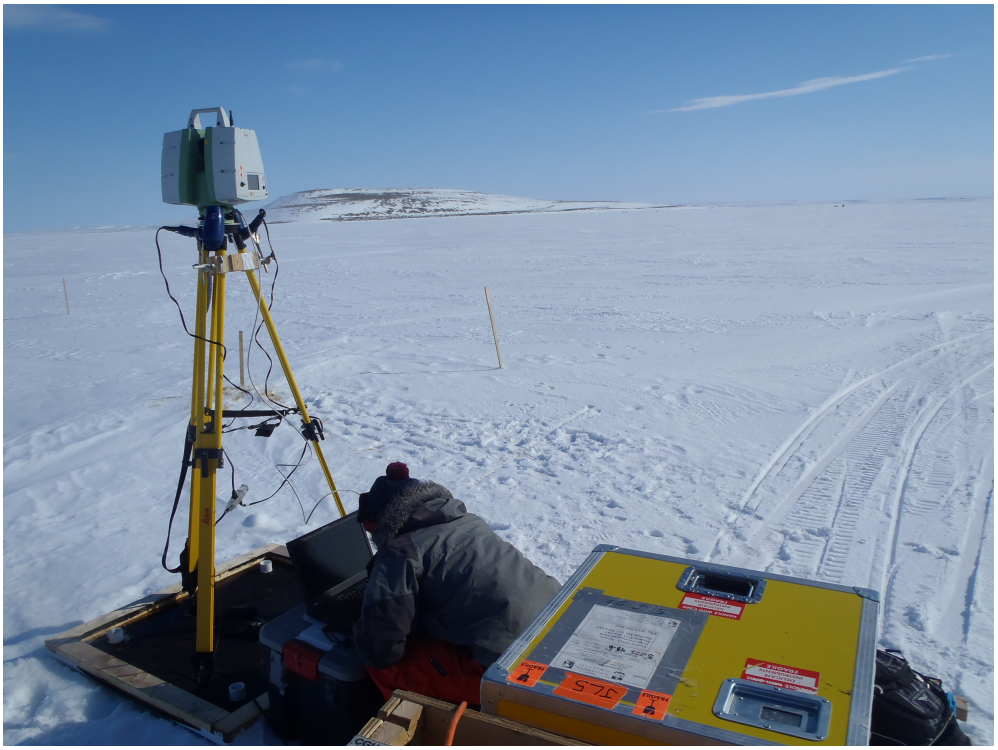

Figure 2.6. The LiDAR laser scanner set up during the 2012 Arctic-ICE project.

2.6 Ridged Sea Ice Scattering

As shown in Section 2.1, sea ice is a heterogeneous and complex dielectric medium that is made up of freshwater ice, liquid brine inclusions, and air. The brine content of sea ice, and its temperature, salinity, and density, are major determinants of the dielectric properties of the ice (Carlstrom and Ulander, 1995). The combination of these dielectric properties and parameters in sea ice, such as the ice permittivity, the volume fraction of constituents, the make up of brine pockets, and the ice temperature and salinity, make sea ice a complex medium for examining surface scattering (Carsey et al., 1992). Sea ice microwave signatures are influenced by the propagation and attenuation of microwaves, which in turn are determined by the dielectric properties of the ice and snow on the target surface (Petrich and Eicken, 2010). The dielectric constant is usually calculated using brine volume, ice density, and the dielectric properties of the ice and brine (Arcone et al., 1986; Onstott and Shuchman, 2004; Stogryn, 1971). Vant et al. (1978) showed the dielectric constant to have an almost linear relationship with the volumetric content of brine. The physical ice conditions, environmental conditions, and the snow cover over the ice particularly influence microwave signatures of sea ice (Lubin and Massom, 2006).

Early works by Carsey et al. (1992) determined that the ideal radar incidence angle range is 20 to 70° for examining sea ice backscatter. At incidence angles outside of this range, scattering responses intersect each other, causing an inaccurate backscatter response. In this ideal incidence angle range, different sea ice types (i.e. ridges, deformed ice, smooth ice, multiyear ice) can be distinguished from one another (Onstott et al., 1979). Grandell et al. (1993) determined that examining a combination of

copolarized and cross-polarized backscatter responses at a range of incidence angles produces the most precise results. Polarization, along with emission and scattering properties, can be important parameters for discriminating between ice types (Carlstrom, 1995; Lubin and Massom, 2006). Microwave data from ridges produces best results when collected at lower frequencies (P, L, S or C bands) (Askne and Johansson, 1988; Holt et al., 1990). Data for this thesis were collected at C-band frequency, as C-band microwaves only penetrate ice up to a maximum of a few centimetres, and backscatter from FYI is dominated by ice surface scattering (Kim et al., 1985).

When examining backscatter of FYI, surface roughness is usually the dominant backscatter mechanism, however dielectric discontinuities (between freshwater ice, air, and liquid brine inclusions), radar wavelength, polarization, and incidence angle, and the orientation of surface features, also contribute to the response of microwave signatures (Carsey et al., 1992; Lubin and Massom, 2006; Weeks and Ackley, 1986). When the elongated part of ridges are oriented parallel to radar, they have weaker backscatter returns, while when they are oriented perpendicular to radar, they have stronger backscatter returns (Carlstrom, 1997; Carlstrom and Ulander, 1995).

Surface scattering of sea ice mainly depends on surface roughness, inhomogeneity within the ice, and the bulk dielectric constant, while backscatter responses of sea ice mainly depend on surface roughness and volume scattering (Carsey et al., 1992). Ridges have strong backscatter due to their extreme surface roughness and tilted ice blocks (ice blocks are piled randomly and therefore contain gaps and overhangs). Ridge features add to the radiometric variability and complexity of the ice surface (Carlstrom, 1995; Carsey et al., 1992). The convergence process of ridge formation and the protruding nature of

ridges on the ice surface usually causes increased weathering, which increases the porosity and lowers the salinity and density of the ice, therefore increasing volume scattering in the backscatter response (Carlstrom and Ulander, 1995; Onstott, 1992; Tucker et al., 1992). Backscatter from ridges can depend on parameters such as air and brine inclusions in the ice, but also on discontinuities in the dielectric constant due to the surface composition. When volume scattering occurs, the dielectric inhomogeneity will result in a loss of energy within the volume. Volume scattering within ridges occurs in the surface blocks of the sail. When examining rough ice backscatter, volume scattering must be taken into account as it can result in depolarization (a rotation of the polarization of the incoming wave) (Richards, 2009). When the dielectric constant of the scattering medium is large, no volume scattering will occur since there will be extremely little transmission into the medium (Carsey et al., 1992).

Microwave backscatter can also depend on the correlation length of the roughness at the surface. Correlation is a function of closeness, so adjacent positions will always be highly correlated, while correlation decreases with increased position distances. The correlation length of surface roughness is defined as horizontal variations in surface height (height variations based on position). FYI ridges have short correlation lengths, since their surface heights vary significantly based on horizontal position (Richards, 2009). Carlstrom (1995) found that there was a high correlation between the backscattering coefficient and the root mean square height, as well as the slope parameter. This was attributed to a large amount of specular reflections from blocks oriented at particular angles.

As mentioned in Section 2.1, FYI is constantly changing over time and throughout the seasons, meaning that the scattering characteristics of the ice also change throughout the seasons and as the ice ages. The microwave signatures of pressure ridges change with time, since the physical composition of the ice changes, and snow accumulates and then melts on the ice surface (Carsey et al., 1992). The behavior of ridge backscatter can change significantly as temperature fluctuations occur throughout different seasons of the year (Richards, 2009). During the Arctic melt season (late spring and early summer), the ice blocks that make up ridges are ablated, so that the originally sharp-edged blocks become more rounded, and the blocks become moist due to increasing temperatures, which can decrease the backscatter returns from the blocks (Carsey et al., 1992). At the beginning of the melt season, temperature variations can be significant and the air-ice/snow interface can vary between melting and freezing temperatures in the span of a few hours, leading to surface melting and recrystallization of ice, changing the physical composition of the ice surface (Hudier and Larouche, 2005). As the ice becomes increasingly desalinated throughout the melt season, there can be an increase in volume scattering within the ice blocks (Carlstrom, 1995). As previously mentioned, during the Arctic melt season surface melting causes increased connectivity of brine channels, which leads to the desalination of sea ice, increasing air space and porosity in the ice (Carsey et al., 1992). This phenomenon can significantly affect microwave backscatter. When the liquid water content of sea ice is over 8% a negligible amount of the emitted waves are transmitted into the medium and volume scattered, resulting in backscatter becoming highly dependent on surface roughness (Hudier, 2006).

Snow cover also has the potential to affect microwave surface scattering. A dry snow cover on a ridge contains ice grains and air, while a wet snow cover contains ice grains, air, and liquid water and/or brine (Carlstrom, 1995; Carsey et al., 1992). In the Arctic winter, the snow covering the ice surface is dry, allowing significant transmission of microwave energy to the ice surface, while in the Arctic spring and summer, snow is wet and can scatter incoming microwave energy before it reaches the ice surface (Guneriussen, 1997). When the wetness content of the snow is high, surface scattering from the snow plays a significant role, while when the wetness content of the snow is low (only a few percent), backscatter intensity can decrease due to attenuation (Carlstrom, 1995). The permittivity of ice and air is significantly lower than the permittivity of water, so the water content of the snow decides the dielectric properties of wet snow. The melting and freezing processes cause a metamorphism of the snow composition, changing the density of the snow, and therefore the response of the snow to microwaves (Carsey et al., 1992). This thesis focuses on winter scattering from ridges, so there will be no melt or melt-freeze temperature fluctuations at the surface, and therefore should be zero to non-significant small amounts of surface scattering from the snow layer.

Backscatter from ridges was not modelled until 1987, when Johansson and Askne designed a model that combined scattering from rough surfaces of ice blocks with specular reflections from randomly oriented blocks. Manninen (1992) extended this model to incorporate ice block size distribution and block orientation into the backscatter response. Manninen's model focused on rough scattering from ice blocks, and only examined specular reflections as a second order contributor. In 1995, Carlstrom and Ulander proposed a backscatter model for deformed sea ice, including ridges, which

focused on height variations across the surface. Carlstrom (1997) further extended this model to include specular reflections from perfectly oriented ice blocks, as well as random scattering from the rough surfaces of differently oriented ice blocks. All models of FYI ridge backscatter are based on Maxwell's equations of classical electrodynamics (Gauss' Law for electric fields, Gauss' Law for magnetic fields, Faraday's Law of magnetic induction, and Ampere's Law (including Maxwell's displacement current)), which explain the electric and magnetic fields in a propagating wave, and how these fields change with time and surface interactions (Winebrenner et al., 1992). All of these backscatter models, and all that have been proposed since, are modelled from scattering coefficient responses from SAR satellite imagery, while none have used a scatterometer to examine *in situ* scattering. Very few studies in general have examined *in situ* microwave backscatter from ridges.

Onstott (1992) discovered that rough surfaces have a slight decrease in the backscatter coefficient with an increasing radar incidence angle, and that the backscatter coefficients for the HH and VV polarizations are very similar (smooth surfaces result in a divergence of the backscattering coefficient for HH and VV polarizations as the incidence angle increases). Carlstrom (1997) found that at low incidence angles one side of ice blocks dominates backscatter, while at high incidence angles backscatter includes increased scattering from multiple sides of ice blocks. Hudier and Larouche (2005) further discovered the there is a strong decrease in the backscatter coefficient for rough surfaces between incidence angles of 10 to 30°. This section summarizes what is currently known about microwave scattering from sea ice ridges.

2.7 Chapter Summary and Conclusion

This chapter reviewed literature that examined what is currently known about microwave scattering of FYI ridges, while having provided an overview of the seasonal cycle of FYI, the formation of ridges, the current methods of measuring sea ice surface roughness, microwave remote sensing, and provided an introduction to the major instrumentation used in this thesis. It is clear that ice surface roughness is a result of complicated thermodynamic and dynamic processes, and is continuously changing. Measuring extreme ice roughness precisely has proven difficult. Previous studies that have examined how microwaves interact with ridges have only examined generalized results, and have not examined parameters associated with microwave signatures, as the backscatter returned to the sensor is a combination of snow scattering, surface scattering at the snow-ice interface, volume scattering within the ice blocks, and heavily depends on air temperature and parameters of the radar instrument. A better understanding of how radar and target parameters affect microwave backscatter is needed for a variety of applications, including marine transportation and navigation, climatological studies, offshore oil and gas exploration, and monitoring oil spills in sea ice.

Using microwave images acquired by satellites provides an easy and accessible way of identifying areas of deformed sea ice, without having to use alternate more costly, time consuming, and small-scale methods (such as on-ice surveys and low-level aerial surveys). SAR imagery can be used to identify and track large areas of deformed sea ice for hazard identification purposes for ice infrastructure and ship traffic (Barker et al., 2008), however, only large ridges can be identified in SAR imagery, where smaller ridges within the image pixel are also contributing to the backscatter response (Haas et al., 1999;

Karvonen et al., 2004). Smaller scale *in situ* studies are needed to better understand ridge responses in SAR imagery. Results from this thesis will provide new *in situ* information on FYI ridges that could be scaled to satellite resolution for use in ridge detection and monitoring.

In the next chapters, the relative contribution of C-band backscatter will be examined to better understand how radar and surface target parameters change the overall C-Band backscatter of ridged sea ice.

Chapter Two References

Anderson D.L. (1958). A model for determining sea ice properties. *Arctic Sea Ice. U.S. National Academy of Sciences – National Research Council*, 598: 148-152.

Arcone S.A., Gow A.J., and McGrew S.J. (1986). Structure and dielectric properties at 4.8 and 9.5 GHz of saline ice. *Journal of Geophysical Research*, 91 (C12): 14281-14303.

Armstrong T., Roberts B., and Swithinbank C. (1973). Illustrated glossary of snow and ice. *Scoot Polar Research Institute, University of Cambridge*, 69.

Askne J. and Johansson R. (1988). Ice ridge observations by means of SAR. *Proceedings of IGARSS 1988 Symposium, IEEE*, 801-803.

Assur A. (1960) Composition of sea ice and its tensile strength. *SIPRE Research Report*, 44.

Barker A., Abrea R.D., and Timco G.W. (2008). Satellite detection and monitoring of sea ice rubble ice fields. *Proceedings 19th IAHR International Symposium on Ice*, 1: 419-430.

Barry R.G. (1996). The parameterization of surface albedo for sea ice and its snow cover. *Progress in Physical Geography*, 20: 63–79.

Carlstrom A. (1995). Modelling microwave backscattering from sea ice for synthetic-aperture radar applications. *Chalmers University of Technology*, Technical Report 271: 1-23.

Carlstrom A. (1997). A microwave backscattering model for deformed first-year sea ice and comparisons with SAR data. *IEEE Transactions of Geoscience and Remote Sensing*, 35: 378-391.

Carlstrom A. and Ulander L.M.H. (1995). Validation of backscatter models for level and deformed sea-ice in ERS-1 SAR images. *International Journal of Remote Sensing*, 16: 3245-3266.

Carsey F.D., Barry R.G., and Weeks R.F. (1992). Introduction. In: Carsey F.D., Microwave remote sensing of sea ice. *American Geophysical Union*, 1-7.

Elachi C. (1988). Spaceborne radar remote sensing: applications and techniques. *Institute of Electrical and Electronics Engineers*, 255.

Garbrecht T., Lupkes C., Augstein E., and Wamser C. (1999). The influence of a sea ice ridge on low-level air flow. *Journal of Geophysical Research*, 104 (20): 24499–24507.

Geldsetzer T., Mead J.B., Yackel J.J., Scharien R.K., and Howell S.E.L. (2007). Surface-based polarimetric C-band scatterometer for field measurements of sea ice. *IEEE Transactions on Geoscience and Remote Sensing*, 45 (11): 3405-3416.

Grandell J., Pallonen J., Hallikainnen M., and Toikka M. (1993). Scatterometer measurements of arctic sea ice at C-band. *Laboratory of Space Technology, Helsinki University of Technology*, 853-854.

Grenfell T.C. and Maykut G.A. (1977). The optical properties of ice and snow in the Arctic Basin. *Journal of Glaciology*, 18: 445-463.

Guneriussen T. (1997). Backscattering properties of a wet snow cover derived from ERS-1 SAR data. *International Journal of Remote Sensing*, 18 (2): 375-392.

Haas C. (2010). Dynamic versus thermodynamics: the sea ice thickness distribution. In: Thomas D.N. and Dieckman G.S., Sea ice. *John Wiley and Sons Limited*, (4): 113-151.

Haas C., Liu Q., and Martin T. (1999). Retrieval of Antarctic sea-ice pressure ridge frequencies from ERS SAR imagery by means of *in situ* laser profiling and usage of a neural network. *International Journal of Remote Sensing*, 20 (15-16): 3111-3123.

Holt B., Crawford J., and Carsey F. (1990). Characteristics of sea ice during the Arctic winter using multifrequency aircraft radar imagery. In: Ackley S.F. and Weeks W.F. Sea ice properties and processes. *U.S. Army Cold Regions Research and Engineering Laboratory*, 244.

Hudier E. (2006). Low back-scattering bands paralleling pressure ridges on first year sea-ice. *IEEE*, 6: 772-725.

Hudier E. and Larouche P. (2005). A potential of polarimetric SAR data in mapping first year sea ice pressure ridges from the coherent and non-coherent components of HH and VV channels. *European Association of Remote Sensing Laboratories Proceedings*, 4: 130-138.

Johansson R. and Askne J. (1987). Modeling of radar backscattering from low-salinity ice with ridges. *International Journal of Remote Sensing*, 8: 1667-1677.

Karvonen J., Similä M., Haapala J., Haas C., and Mäkynen M. (2004). Comparison of SAR data and operational sea ice products to EM ice thickness measurements in the Baltic Sea. *Proceedings, IEEE International Geoscience and Remote Sensing Symposium (IGARSS'04), Anchorage, Alaska. (IGARSS)*, 5: 3021–3024.

Kim Y.S., Moore R.K., Onstott R.G., and Gogineni S. (1985). Towards identification of optimum radar parameters for sea-ice monitoring. *Journal of Glaciology*, 31 (109): 214-219.

Kwok R., Zwally H.J., and Yi D. (2004). ICESat observations of Arctic sea ice: a first look. *Geophysical Research Letters*, 31: L16401.

Landy J.C., Ehn J., Shields M., and Barber D.G. (2014). Surface and melt pond evolution on landfast first-year sea ice in the Canadian Arctic Archipelago. *Journal of Geophysical Research*, 119 (5): 3054-3075.

Launaiinen J. and Vihma T. (1994). On the surface heat fluxes in the Weddell Sea. In: Johannessen M., Muench R.D., and Overland J.F. Polar oceans and their role in shaping the global environment. *American Geophysical Union*, 85: 399-419.

Laxon S., Peacock N., and Smith D. (2003). High interannual variability of sea ice thickness in the Arctic region. *Nature*, 425: 947–950.

Lee J.S. and Pottier E. (2009). Polarimetric radar imaging: from basics to applications. *CRC Press*, 1-422.

Lensu M. (2003). The evolution of ridged ice fields. *Helsinki University of Technology Ship Laboratory*, 1-140.

Li S., Cheng Z., and Weeks W.F. (1998). Extraction of intermediate scale sea ice deformation parameters from SAR ice motion products. In: Tsatsoulis C. and Kwok R. Analysis of SAR data of the polar oceans: recent advances. *Springer-Verlag Berlin*, 69-90.

Lubin D. and Massom R. (2006). Polar remote sensing (atmosphere and oceans). *Springer-Praxis Books in Geophysical Science*, 1: 309-616.

Mai S., Wamser C., and Kottmeier C. (1996). Geometric and aerodynamic roughness of sea ice. *Boundary-Layer Meteorology*, 77: 233-248.

Malmgren F. (1927). On the properties of sea ice. *Norwegian North Pole Expedition "Maud" 1918–1925*, 1: 1–67.

Manninen A.T. (1992). Effects of ice ridge properties on calculated surface backscattering in BEPERS-88. *International Journal of Remote Sensing*, 13: 2469-2487.

Melling H. (1998). Detection of features in first-year pack ice by synthetic aperture radar (SAR). *International Journal of Remote Sensing*, 19: 1223-1249.

Melling H. and Riedel D.A. (2004). Draft and movement of pack ice in the Beaufort Sea: a time-series presentation April 1990–August 1999. *Canadian Technical Reports on Hydrographic Oceanic Science*, 238: 24.

Morey R.M., Kovacs A., and Cox G.F.N. (1984). Electromagnetic properties of sea ice. *Cold Regions Science and Technology*, 9 (1): 53-75.

Onstott R.G. (1992). SAR and scatterometer signatures of sea ice. In: Carsey F.D., Microwave remote sensing of sea ice. *American Geophysical Union*, 73-104.

Onstott R.G., Moore R.K., and Weeks W.F. (1979). Surface-based scatterometer results of arctic sea ice. *IEEE Transactions on Geoscience Electronics*, GE-17 (3): 78-85.

Onstott, R.G., and Shuchman R. (2004). SAR measurements of sea ice. *Synthetic Aperture Radar Marine User's Manual*. Washington, DC: National Oceanic and Atmospheric Administration.

Parashar S.K., Haralick R.M., Moore R.K., and Biggs A.W. (1977). Radar scatterometer discrimination of sea ice types. *IEEE Transactions on Geoscience Electronics*, GE-15 (2): 83-87.

Petrich C. and Eicken H. (2010). Growth, structure and properties of sea ice. In: Thomas D.N. and Dieckman G.S., Sea ice. *John Wiley and Sons Limited*, (2): 23-77.

Renslow M.S. (2012). Manual of airborne topographic LiDAR. *American Society for Photogrammetry and Remote Sensing*.

Richards J.A. (2009). Remote sensing with imaging radar. *Springer-Verlag Berlin Heidelberg*, 1-320.

Rothrock D.A., Percival D.B., and Wensnahan M. (2008). The decline in arctic sea ice thickness: separating the spatial, annual, and interannual variability in a quarter century of submarine data. *Journal of Geophysical Research*, 113: C05003.

Strogryn A. (1971). Equations for calculating the dielectric constant of saline water. *IEEE Transactions in Microwave Theory and Techniques*, 19: 733-736.

Timco G.W., Croasdale K., and Wright B. (2000). An overview of first-year sea ice ridges. *Canadian Hydraulics Centre Technical Report HYD-TR-047*, 5 (112): 1-157.

Tucker W.B., Perovich D.K., Gow A.J., Weeks W.F., and Drinkwater M.R. (1992). Physical properties of sea ice relevant to remote sensing. In: Carsey F.D. Microwave remote sensing of sea ice. *American Geophysical Union*, 9-28.

Tucker W.B., Sodhi D.S., and Govoni J.W. (1984). Structure of first-year pressure ridge sails in the Prudhoe Bay region. In: Barnes P.W., Schell D.M., and Reimnitz E. The Alaskan Beaufort Sea: ecosystems and environments. *New York Academic Press*, 115-135.

Ulaby F.T., Kouyate F., Brisco B., and Lee Williams T.H. (1986). Textural information in SAR images. *IEEE Transactions of Geoscience and Remote Sensing*, 24 (2): 235-245.

Vant M.R., Ramseier R.O., and Makios V. (1978). The complex-dielectric constant of sea ice at frequencies in the range 0.1-40 GHz. *Journal of Applied Physics*, 49: 1264-1280.

Vihma T., Hartmann J., and Lupkes C. (2003). A case study of on-ice air flow over the marginal sea-ice zone. *Boundary-Layer Meteorology*, 107: 189-217.

Wadhams P. (2000). Ice in the ocean. *Gordon and Breech*, 364.

Wadhams P. and Davis N.R. (2000). Further evidence of ice thinning in the Arctic Ocean. *Geophysical Research Letters*, 27: 3973–3975.

Weeks, W. F., and Ackley S.F. (1986). The growth, structure and properties of sea ice. In: Untersteiner N. The geophysics of sea ice, NATO ASI Ser. B, *Springer, New York*, (146): 9-164.

Winebrenner D.P., Bredow J., Fung A.K., Drinkwater M.R., Nghiem S., Gow A.J., Perovich D.K., Grenfell T.C., Han H.C., Kong J.A., Lee J.K., Mudaliar S., Onstott R.G., Tsang L., and West R.D. (1992). Chapter 8: microwave sea ice signature modeling. In: Carsey F.D. Microwave remote sensing of sea ice. *American Geophysical Union*, 137-175.

Winebrenner D.P., Long D.G., and Holt B. (1998). Mapping the progression of melt onset and freeze-up on arctic sea ice using SAR and scatterometry. In: Tsatsoulis C. and Kwok R. Analysis of SAR data of the polar oceans: Recent advantages. *Springer-Verlag Berlin*, 129-144.

Woodhouse I.A. (2006). Introduction to microwave remote sensing. *CRC Press – Taylor and Francis Group*.

Zwally H.J., Yi D., Kwok R., and Zhao Y. (2008). ICESat measurements of sea ice freeboard and estimates of sea ice thickness in the Weddell Sea. *Journal of Geophysical Research*, 113: C02S15.

Chapter Three – Polarimetric C-band Microwave Scattering from Artificial Winter First-Year Sea Ice Ridges with No Snow Cover

This paper was submitted April 6, 2015 as a manuscript to the International Journal of Remote Sensing.

Shields M.E., Warner K., Scharien R., and Barber D.G. Polarimetric C-band microwave scattering from artificial winter first-year sea ice ridges with no snow cover. *International Journal of Remote Sensing*, (in review).

Abstract

Microwave backscatter from sea ice ridges is poorly understood. Identifying and recognizing these features through microwave backscattering signatures, measured either *in situ* or by satellites, has important implications for a variety of applications, including offshore industry, marine mammal habitat, navigation, and natural resource exploration. This paper uses *in situ* data from the Sea-ice Environmental Research Facility to examine C-band microwave backscatter of non-snow covered sea ice ridges, and how they respond based on changes to ridge and radar parameters that affect microwave backscatter intensity. A C-band microwave scatterometer was used to measure backscatter from 11 artificial ridges built during three experiments. High-resolution terrestrial LiDAR models were used to precisely measure ridge height relative to freeboard, ridge volume, macro and micro-scale surface roughness, slope angles of sail blocks, and ridge slopes. Results show that using an incidence angle in the range of 30° to 50° and HV polarization will best enable discrimination between smooth and ridged ice, and that using an incidence angle of 40° and a polarization of HV or HH will best enable detection of variations in ridge height. Results also show that the variance in backscatter comes primarily from incidence angle, ridge height, and polarization, with 88% of the variability in backscatter attributed to ridge height. The backscatter coefficient was found to increase with average ridge height up to a maximum of 0.50 m, after which it becomes more variable. Ridge height is determined to be the significant parameter affecting C-band microwave scattering for first-year sea ice ridges with no snow cover during winter.

3.1 Introduction

Arctic sea ice plays an important role in enhancing heat fluxes towards the pole, and regulating radiant energy absorption and emission, as well as other large-scale global climate processes (Carsey et al., 1992). There have been dramatic changes to the sea ice cover, thickness, volume, and extent, in all sectors of the Arctic (Comiso and Hall, 2014; Johannessen et al., 1999). These changes are both affected by and have effects on the physical and meteorological processes operating across the ocean-sea ice-atmosphere (OSA) interface. This paper examines sea ice ridges, which are important ice features in regards to marine transportation and navigation, climatological studies, offshore oil and gas exploration, and monitoring oil spills in sea ice. Ice operations prefer to operate in areas of open water or thin ice, and to avoid potentially unmanageable thick ice features, such as icebergs, multiyear ice floes, and ridges (Carlstrom, 1995).

First-year sea ice (FYI) ridges form when otherwise smooth floes are compressed together by ocean currents and winds. When these floes are compressed and sheared together, ice blocks are piled above (sail) and below (keel) the level ice surface due to a combination of crashing, bending and buckling failures. In general, the sail of the ridge is one-tenth the volume of the keel (Timco et al., 2000). These ice blocks, usually the same thickness as the converging ice floes, form in a linear pattern surrounded by undeformed, or slightly deformed ice (Hudier and Larouche, 2005; Tucker et al., 1984). Usually the middle portion of the ridge (along the water line) is re-frozen together, creating a consolidated layer of ice. These FYI ridges are elongated linear features that can extend for hundreds of metres, with widths up to ten metres, and heights up to several metres (Haas et al., 1999; Timco et al., 2000; Wadhams, 2000). In areas of high

convergence and compression, ridges and deformed ice can form close together, creating rubble (or ridged) ice fields (Lensu, 2003). The degree of deformation of the ice depends on the atmospheric and ocean forced compressions at the surface during the time of formation (Haas et al., 1999). The ice blocks that make up FYI ridges are angular and not uniformly oriented, which creates significant airspace between blocks within a non-snow covered ridge.

Understanding the effects of FYI ridges on either *in situ* or satellite derived microwave backscatter is needed for a variety of applications; i.e. habitat studies, modeling ice drift, navigating vessels through ice-infested waters, assessing threats to offshore platforms, and identifying ice loads near and against ice infrastructure (Lensu, 2003). The convergence process of ridge formation and the protruding nature of ridges on the ice surface causes increased weathering, increasing the porosity, and lowering the salinity and density of the ice, which then increases the volume scattering contribution to backscatter (Carlstrom and Ulander, 1995; Tucker et al., 1992; Onstott, 1992). FYI ridges have strong backscatter relative to undeformed sea ice, due to extreme surface roughness and randomly oriented tilted ice blocks, which results in surface roughness dominating scattering, although volume scattering can contribute significantly to backscatter.

The ensemble backscatter signature from ridged ice is a combination of snow scattering, surface scattering at the snow-ice interface, volume scattering within the surface ice blocks, dielectric discontinuities (between freshwater ice, air, and liquid brine inclusions), the orientation of surface features, and is dependent on air temperature and radar wavelength, polarization, and incidence angle (Carlstrom, 1995; Lubin and

Massom, 2006; Onstott, 1992; Tucker et al., 1992; Weeks and Ackley, 1986). The purpose of this study was to determine which parameters (radar or ridge) make a significant contribution to C-band backscatter signatures. This study used data collected during the winter season (ice was never in a melting state) with no snow cover, in an attempt to determine how parameters other than snow and temperature affect C-band backscatter from ridges.

Microwave backscattering from sea ice ridges is poorly understood, and there is limited research that successfully determines how backscatter changes when ridge and radar parameters are changed. The majority of studies have compared microwave backscatter of ridges to other ice types (i.e. smooth ice, multiyear ice, slightly deformed ice), while few studies have used scatterometer measurements or modelling experiments to examine microwave scattering from ridges for satellite validation (such as Carlstrom (1997) and Onstott et al. (1979)), but no studies have examined in depth how specific individual parameters (i.e. incidence angle, polarization, ridge height) can affect microwave backscatter from FYI ridges.

This paper uses artificial ridges built at the Sea-ice Environmental Research Facility (SERF), located on the University of Manitoba campus, to address the relative contribution of C-band microwave scatterometer parameters (incidence angle, linear and polarimetric parameters) relative to variable target parameters (ridge height, surface roughness, slope values, and approximate air space volumes in the bare ice ridges) on the overall backscatter from first-year ridged sea ice. Results from this paper will provide new *in situ* information on sea ice ridges that could be scaled to satellite resolution for use in ridge detection and monitoring.

3.2 Data and Methods

3.2.1 Study Area

Data for this study were collected at SERF in Winnipeg, Manitoba, Canada during December 2013 and February 2014. SERF contains an artificial ice tank that is 18.3 m long, 9.1 m wide, and 2.4 m deep. Artificial seawater was created and then frozen by the natural freezing temperatures of a Winnipeg winter. Two mesocosm-scale studies were carried out as part of this study, one from December 16-20, 2013, and one from February 11-15, 2014. Artificial ridges were built on the naturally grown smooth ice surface to mimic natural pressure ridges in the Arctic. The majority of ice blocks were cut out of the ice in an area outside of the experimentation area, and containers were used to freeze the artificial seawater to create the remaining blocks. The difference in salinity values between the blocks frozen in containers and the blocks cut out of the ice were on average 1.4 ± 1.9‰, and can be considered negligible, since the ice block salinities represent values that would be seen in the Arctic. From December 16-20, 2013 two experiments were run, experiment A from December 16-18, and experiment B from December 19-20. During each experiment an artificial sea ice ridge was built on a snow free ice surface and sampled at four ridge heights. From February 11-15, 2014 one experiment was run exactly the same as the December experiment (called experiment C), except only three ridge heights were sampled. For all three experiments there was no snow cover on the ice surface and ridges. At each ridge height, a C-band scatterometer was used to scan the same points across the ridge at a range of incidence angles, a terrestrial LiDAR laser scanner was used to scan the ridge to create a three-dimensional point cloud model, and physical ice samples were taken. Figure 3.1 shows the experimental design, and Figure

3.2 a photograph of the C-band scatterometer and LiDAR laser scanner scanning the third ridge height for experiment A. The aluminum gantry was used to adjust for incidence angle, and an automated tracker on the scatterometer provided range and azimuth adjustment.

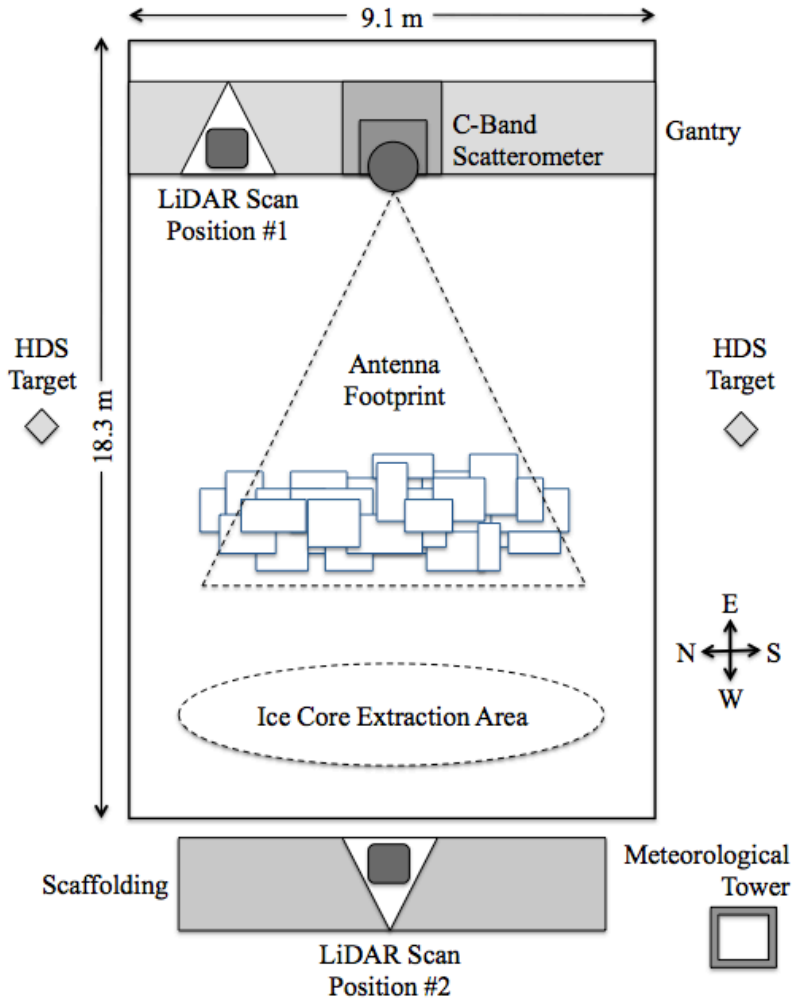

Figure 3.1. Sampling set up for the three sea ice pressure ridge experiments at SERF (not to scale).

Figure 3.2. A photograph of the third ridge height for experiment A, taken on December 17th, 2013. The laser scanning system is set up on the left side of the gantry (on the yellow tripod) and the C-band scatterometer is set up in the middle of the gantry, with the radar antenna encased in the white dome.

During experiments A, B, and C, ridge backscatter data were collected at eleven ridge heights (from smooth ice up to an average height of 0.76 m), at five incidence angles (20, 30, 40, 50, and 60°), at the non-polarized backscatter response total power, and at seven polarimetric backscatter responses (VV, HH, HV, VV-HH phase difference, depolarization ratio, HV/HH, and VV/HH), creating 440 combinations of unique backscatter data.

3.2.2 Target Parameters

A Leica ScanStation C10 discrete-pulse terrestrial laser scanner was used to scan each ridge from two positions in order to create a three-dimensional (3D) digital point cloud model. The time of flight for each laser pulse emitted by the scanner are recorded

once reflected and returned to the scanner from the surfaces of surrounding objects, creating the model. The laser pulses do not penetrate snow and ice surfaces, making LiDAR a precise tool for mapping surface topography (Landy et al., 2014). For each ridge, two 2 mm resolution scans were completed, one from scaffolding on the west side of the tank, and one from the gantry over the east side of the tank (see Figure 3.1). The scanner emits pulses at frequencies up to 50 kHz and at a wavelength of 532 nm. High Definition Surveying (HDS) targets were set up and collected with each scan as control points (creating an arbitrary coordinate system), so that the scans could then be meshed together to create a 3D point cloud model. The point cloud data collected was cleaned up (precipitation and unwanted artefacts removed) and post-processed using Cyclone 9.0 and Quick Terrain (QT) Modeler 7.1.6 software. The post-processed models were used to measure average ridge heights, surface roughness, slope values, and approximate air space volumes in the bare ice ridges.

Using the point cloud models, 100 vertical heights were measured relative to freeboard in metres across each individual ridge, in order to obtain enough height measurements to precisely represent the entire ridge. The volume of each ridge, including the airspace, was measured using the models. As each ridge was constructed, the approximate block volumes were calculated and these block volumes were then subtracted from the ridge volumes in order to calculate the approximate air space volume in the ridge. These volume measurements are considered an approximation, as the sail ice blocks are not perfect geometric shapes. It is important to note the amount of air space in non-snow covered ridges, as more air space increases the chance that there will be multiple scattering returns (as microwaves can rebound off of multiple block facets).

Slope angles were measured once for each individual block facing the scatterometer antenna that had the potential to affect scattering, and numerous times across the face of each ridge oriented towards the antenna, to determine the small and large-scale angles of the ridges. The angles were calculated using the surface normal and the smooth ice surface, in order to examine if the overall slopes of the blocks and ridges relative to the antenna created any variance in microwave backscatter. These slope angles represent a measure of the angle of tilt of each block (or ridge) relative to the scatterometer antenna.

Measuring the small and large-scale roughness of sea ice is important for determining how much roughness is contributing to the variability of the backscatter. Landy et al. (2015) present a method for removing large-scale topography from a sea ice surface in order to examine small-scale roughness that is inclined relative to the scatterometer antenna. For a ridge this would be the small-scale roughness of the relatively smooth sail block surfaces. In the case of this study however, the effect of small-scale roughness from the surfaces of ice blocks on the overall scattering response can be considered negligible, due to the fact that the overall surface is extremely rough, and large-scale roughness will consistently dominate the backscatter response.

A meteorological tower set up beside SERF had a YSI 44212 Thermilinear Probe, containing a Vaisala capacitive relative humidity sensor and 44212 thermistor housed in a 41003-X 10 plate grill radiation shield, which measured air temperature and relative humidity approximately 2.2 m above the ground every minute during the sampling periods. At each ridge height, 10 ice block salinity samples were taken, and ice block surface temperatures were measured up to 10 times across the ridge. A summary of

meteorological and physical ice parameter ranges and averages from the sampling dates are shown in Table 3.1. Geophysical parameters of the artificial ridges are considered to be simulations of young ice ridge formation in terms of salinity, ridge height, and block size (Onstott, 1992).

Table 3.1. Averages and ranges of meteorological and sail ice block parameters from experiments A, B and C. During some sampling days the sail ice blocks were too cold to drill a temperature probe into, and so there are no maximum or average ice temperature readings for the experiments.

	Air Temperature Mean (°C)	Relative Humidity Mean (%)	Sail Block Temperatures (°C)	Sail Block Salinities (‰)
Experiment A Min/Max	-24.36 to -11.91	57 - 84.6	≥-15.22 to -3.76	5.8 - 25.9
Experiment B Min/Max	-26.25 to -15.03	55.3 - 80.0	≥-21.26 to -16.00	5.0 - 17.7
Experiment C Min/Max	-24.42 to -12.43	47.8 - 89.5	≥-16.90 to -12.23	2.9 - 9.4
Experiment A Average	-17.38 ±3.602	72.5 ± 7.74		10.6 ± 3.4
Experiment B Average	-20.22 ± 3.553	70.9 ± 6.39		10.6 ± 3.2
Experiment C Average	-18.18 ± 2.549	71.3 ± 11.1		6.2 ± 1.6

3.2.3 Radar Parameters

Polarimetric backscatter calibration and data processing were achieved using the methods detailed in Geldsetzer et al. (2007). The microwave data were collected at C-band frequency, which has a penetration depth of only a few centimetres at maximum for winter FYI (Kim et al., 1985). The C-band scatterometer used for this study was a fully-polarimetric radar that emits pulses with a center frequency of 5.5 GHz and a bandwidth of 500 MHz. The antenna was located 2.14 m above the smooth ice surface adjacent to the ridges. Each ridge height scan made at each incidence angle was sampled using an azimuth width of 30°. At each incidence angle five scans were taken and then averaged. Scans of a smooth ice surface were also taken at the same incidence angles for comparison purposes.

When the elongated part of ridges are located perpendicularly to the radar, strong dihedral backscattering occurs due to the much smoother ice alongside the ridge (Johansson and Askne, 1987), resulting in weaker backscattering returns (Carlstrom, 1997; Carlstrom and Ulander, 1995). The data collected for this study were collected with the long axes of the ridges oriented orthogonally to the radar, so that ridge orientations did not play a role in backscatter responses.

3.2.4 Statistical Analysis

Descriptive statistical analysis was run on all of the data to determine significant variables and trends. Optimal backscatter parameters and incidence angles were determined for discriminating between ridged and smooth ice, as well as for detecting variations in ridge height. A principal components analysis (PCA) was run on data from each of the three experiments, as well as all three together. Independent variables incidence angle, polarization, and ridge height, and the dependent variable backscatter coefficient, were used to determine which independent variables are significant in changing the backscatter received by the scatterometer. Multiple regression analyses (MRA) were run on each of experiments A-C, as well as all three datasets combined, using the independent variables incidence angle, polarization, and ridge height, and the dependent variable backscatter coefficient, to further examine the relationship the independent variables have with the dependent variable. A step-wise MRA was also run on the data from each experiment, as well as the entire dataset combined.

3.3 Results and Discussion

3.3.1 Contribution of Target Parameters to Backscatter

Some basic measurements of each ridge calculated using the LiDAR post-processed models, and an intensity image of what the ridge looked like (on the ridge side facing the scatterometer antenna where the scattering responses were generated) are shown in Figure 3.3 for experiment A, Figure 3.4 for experiment B, and Figure 3.5 for experiment C. The experiment A ridges were a maximum of 4.8 m long, the experiment B ridges a maximum of 3.9 m long, and the experiment C ridges a maximum of 4.4 m long.

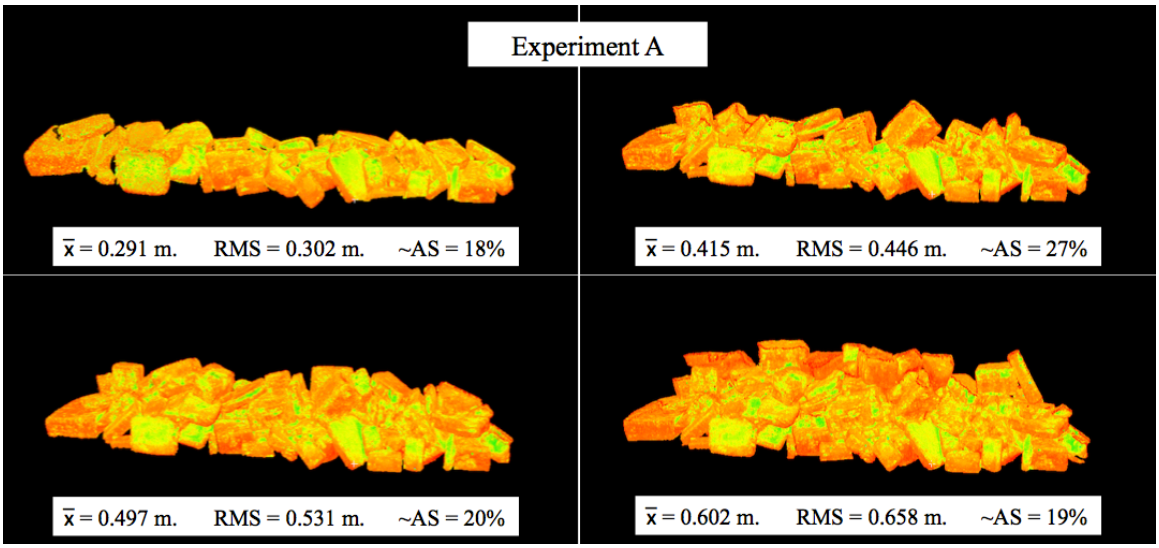

Figure 3.3. The four ridge heights for experiment A. The images are displayed by intensity and show the side of the ridges that were scanned with the C-band scatterometer. X-bar represents the average ridge height, RMS represents the root mean square ridge height, and ~AS represents the approximate air space volume in the ridges.

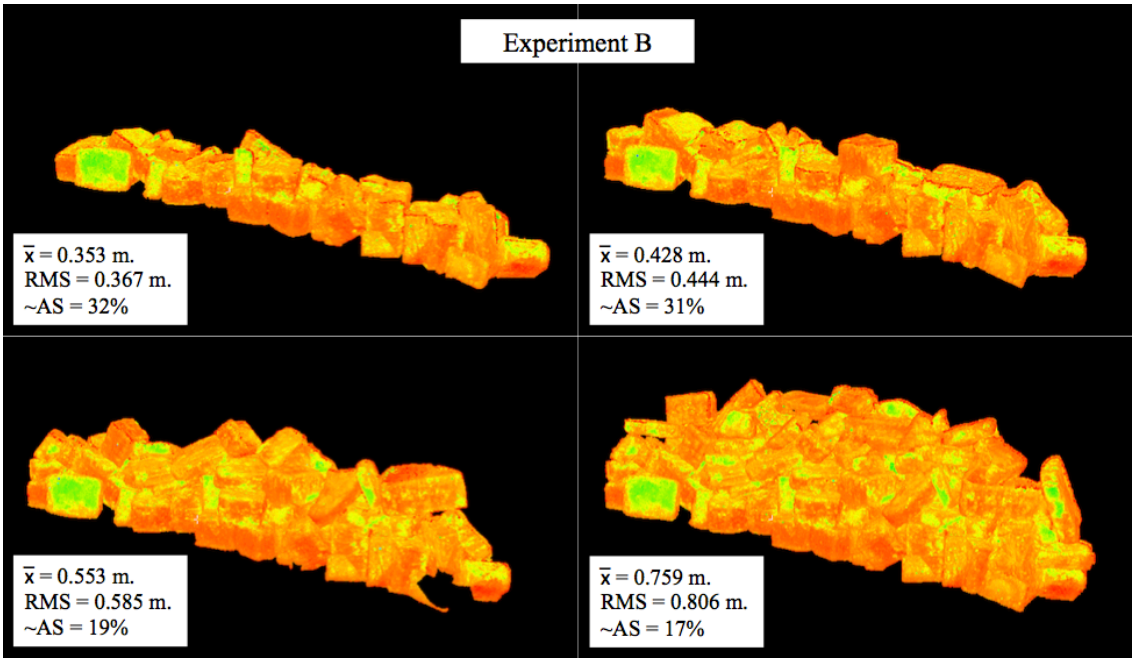

Figure 3.4. The four ridge heights for experiment B. The images are displayed by intensity and show the side of the ridges that were scanned with the C-band scatterometer. X-bar represents the average ridge height, RMS represents the root mean square ridge height, and ~AS represents the approximate air space volume in the ridges.

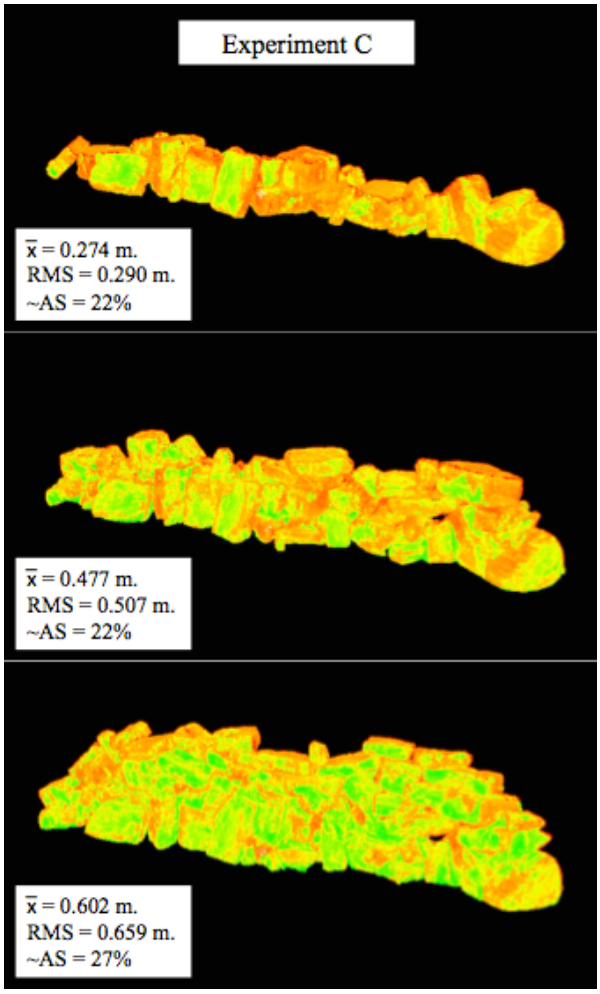

Figure 3.5. The three ridge heights for experiment C. The images are displayed by intensity and show the side of the ridges that were scanned with the C-band scatterometer. X-bar represents the average ridge height, RMS represents the root mean square ridge height, and ~AS represents the approximate air space volume in the ridges.

Average ridge height and the RMS ridge height (represented by x-bar and RMS respectively in Figures 3-5), both measured relative to freeboard, were calculated for each ridge. The approximate air space volumes (represented by ~AS in Figures 3-5) ranged from 17 to 32% of the ridge volume for the 11 ridges. The amount of air space in the non-snow covered ridges are based on the construction of each ridge, and would be significant if higher backscatter responses were correlated with larger air space volumes

(increased multiple scattering returns in the backscatter response), or vice versa, however no evidence was found of this in this study.

For all three experiments, 60% of the block facets facing the radar were tilted towards the radar antenna (61.7% for experiment A, 56.9% for experiment B, and 60.7% for experiment C). The individual ice block slopes are shown in Table 3.2. Slope values were similar for the various ridges in the different experiments, with similar ranges and average values within a 16° range. The average overall slope angle of the ridges were 29.4° for experiment A, 22.9° for experiment B, and 17.8° for experiment C, indicating that the ridges were constructed in a similar and comparable fashion, and that slope angle will not significantly affect backscatter results when comparing responses from these ridges.

Table 3.2. Individual ice block slopes for each experiment, which represent the degree of tilt relative to the scatterometer antenna.

	Minimum (°)	**Maximum (°)**	**Average (°)**	**RMS (°)**
Experiment A	0.895	88.9	36.3	46.1
Experiment B	1.19	75.1	20.7	25.7
Experiment C	1.89	84.2	28.1	35.6

Ridge height was examined by holding polarization and incidence angle constant for all data combinations. In 80% of the data the backscatter signal increased on average 15.3 dB from a smooth ice surface up to an average ridge height of approximately 0.50 m, while the other 20% of the data exhibited a more variable increasing trend (i.e. backscatter increased from a ridge height of 0 to 0.29 m, then slightly decreased from 0.29 to 0.42 m, and then increased (to a value greater than at 0.29 m) from 0.42 to 0.50 m). This is the expected result since the backscatter coefficient increases as surface roughness increases (Carlstrom, 1995; Carsey et al., 1992). Once the ridges reach a

height greater than ~0.50 m the backscatter returns become variable. As the ridge is built up it eventually fills the radar field of view, or resolution cell, and once this is filled entirely with blocks, the scatterometer will see the same set of sail blocks in each scan. When the ridge reaches this point, examining the ridge height parameter is no longer relevant. This is likely why the changes to the backscatter coefficient become smaller as ridge height increases (i.e. the radar field of view is becoming increasingly full of sail blocks). Some of the variability seen could also be attributed to the fact that a greater ridge height means more randomly oriented surfaces, increasing diffuse reflections, creating a large range of backscatter signatures. Figure 3.6 shows the average change in backscatter between increasing ridge heights for each experiment, with the standard deviation of the average shown by error bars. Something to note is that there are similar values in backscatter change for all polarizations.

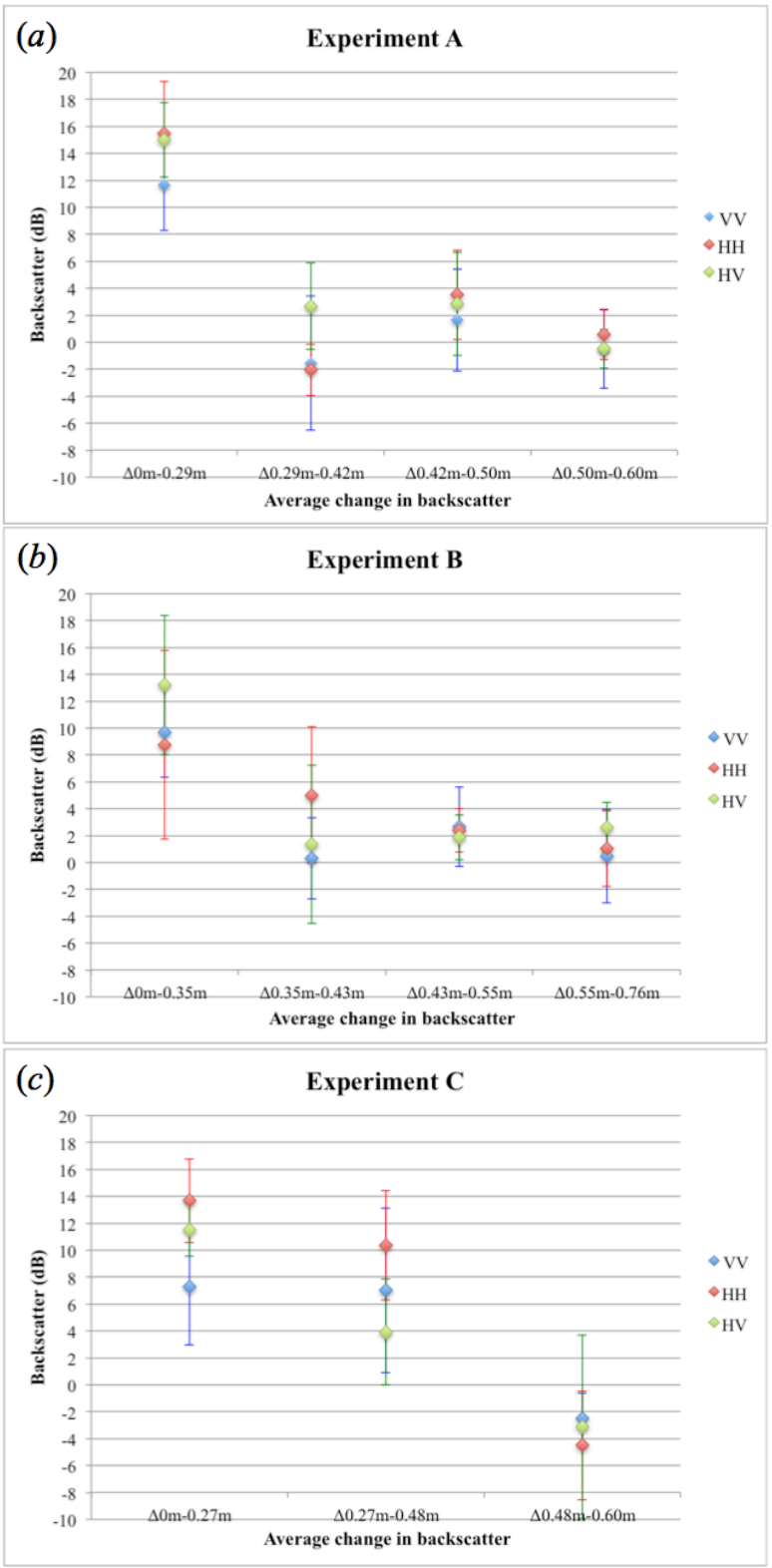

Figure 3.6. The average changes in backscatter between ridge heights for (*a*) experiment A, (*b*) experiment B, and (*c*) experiment C. The average backscatter coefficient for each height is the average of all of the backscatter coefficients for each incidence angle. The vertical error bars represent standard deviations.

3.3.2 Contribution of Radar Parameters to Backscatter

Incidence angle was examined by holding ridge height and polarization constant for all data combinations. There is a slight decreasing trend in the backscatter coefficient as incidence angle increases (starting at 20° and finishing at 60°). For smooth ice scans, the backscatter coefficient on average decreased 5.0 dB from 20 to 60°. The average decrease in the backscatter coefficient for ridged ice was 3.0 dB (4.0 dB for VV polarization, 1.7 dB for HH polarization, and 3.4 dB for HV polarization). Figure 3.7 shows the HH backscatter coefficient values for experiments A-C, as well as the trend lines for each ridge height. The slight decreasing trend with increasing incidence angle is highlighted as expected (Onstott, 1992).

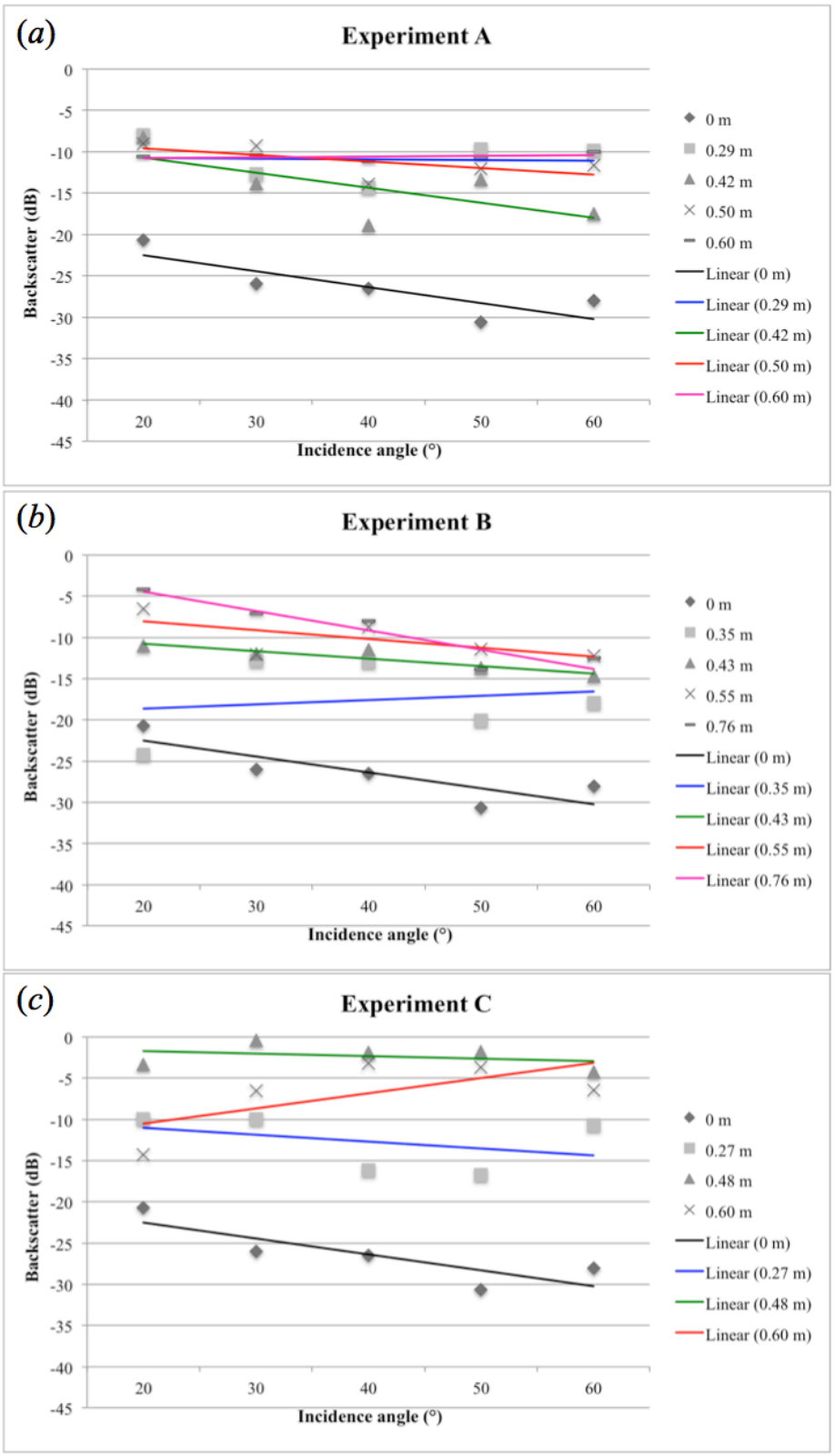

Figure 3.7. The HH backscatter coefficient values for (*a*) experiment A, (*b*) experiment B, and (*c*) experiment C. Each symbol represents a ridge height, and the linear lines represent the incidence angle trend for each ridge height.

Polarization was examined by holding ridge height and incidence angle constant for all data combinations. HV polarization was consistently the lowest backscatter return for the three polarizations, while 80% of the time VV polarization was lower than HH. In the incidences where VV was lower than HH, it was an average of 3.9 dB lower, while when HH was lower than VV, it was only an average of 1.0 dB lower. Normally HV polarization is the lowest backscatter value, and VV is greater than HH when scanning sea ice (and this was the case at all incidence angles for the smooth ice sheet during this study), but once a ridge was added to the radar field of view, HH was higher than VV in the majority of the scans. Figure 3.8 displays a backscatter plot of the ridge from experiment B with an average height of 0.55 m, which shows the backscatter coefficient for each polarization at each incidence angle. For this ridge HH is always greater than VV, and HV was consistently lower. In this study, each polarization produced different backscatter results, but the results were consistent across the different ridges.

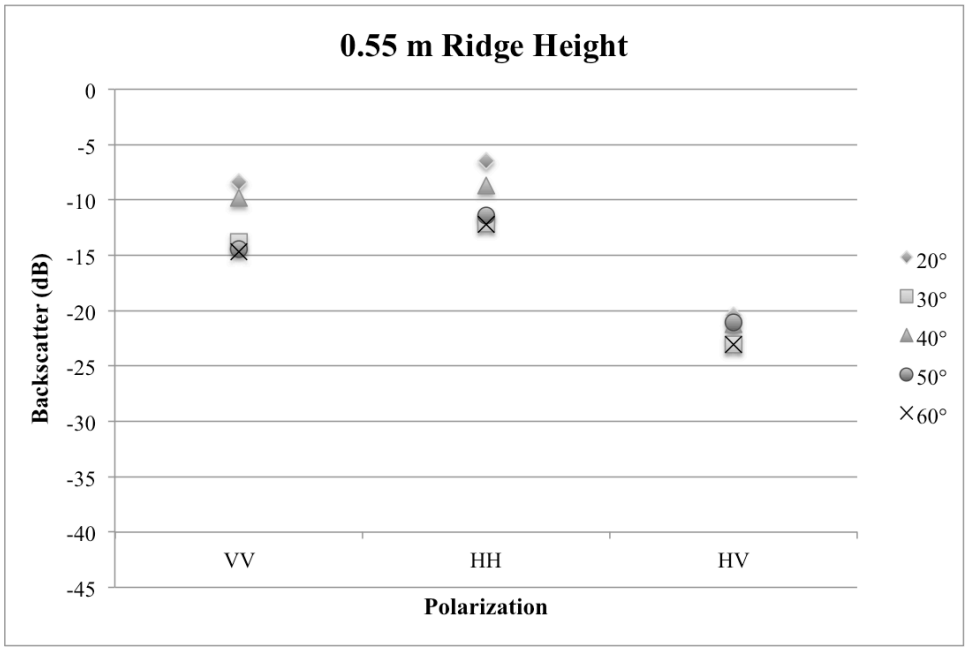

Figure 3.8. Backscatter coefficient plot from the experiment B ridge with an average height of 0.55 m. Symbols represent each incidence angle studied.

All collected backscatter parameters were examined to determine which parameter is optimal for distinguishing ridged ice from smooth ice. In the cold season, both co and cross-polarized signatures are useful for distinguishing between ice types (i.e. ridge, multiyear, smooth), and for comparing different types of the same ice (Onstott and Shuchman, 2004, and Parashar et al., 1977). The polarization backscatter parameters (i.e. VV, HH, and HV) are the best for distinguishing ridges from smooth ice. Each polarization was examined with each ridge height and from this it was determined that the cross-polarization HV is the best backscatter parameter for distinguishing ridges from smooth ice, as there were the largest differences in the backscatter coefficient between the different ice types with HV polarization. Table 3.3 displays the average, maximum, and minimum backscatter increase from smooth to ridged ice for experiments A-C for each polarization. For experiments A-C, HH polarization could be used to distinguish between smooth and ridged ice, except in one outlier case during experiment B, where the backscatter coefficient decreased 3.5 dB from smooth ice to an ice surface containing a small ridge. VV polarization could also be used in most cases to identify ridges from smooth ice, but had smaller increases in the backscatter coefficient than HV and HH polarizations.

Table 3.3. The average, maximum, and minimum backscatter increase from smooth to ridged ice for each polarization for the experiment A-C dataset.

σ° Polarization	Average σ° Increase (dB)	Maximum σ° Increase (dB)	Minimum σ° Increase (dB)
HV	17.0	24.2	6.8
HH	15.6	28.8	6.4*
VV	11.2	18.3	0.9

*The minimum HH increase does not include the outlier case, where σ° decreased 3.5 dB.

Through the examination of each data combination and the use of descriptive statistics, it was determined that using an incidence angle of 30, 40, or 50° produces the best discrimination between smooth ice and ridged ice. HV polarization had the greatest average increase in the backscatter coefficient at 40°, with an increase of 19.2 dB, as well as the maximum increase in the backscatter coefficient at 40°, with an increase of 24.2 dB. HH polarization had the largest increase and the maximum increase in the backscatter coefficient at 50°, with an average increase of 19.1 dB, and a maximum increase of 28.8 dB. VV polarization had the largest increase, and the maximum increase in the backscatter coefficient at 30°, with an average increase of 12.5 dB, and a maximum increase of 18.3 dB. Figure 3.9 shows plots of the backscatter coefficient for each experiment at an incidence angle of 40°. Based on the results of this study, using HV polarization and an incidence angle between 30 and 50° will produce the most precise results for distinguishing between smooth and ridged ice.

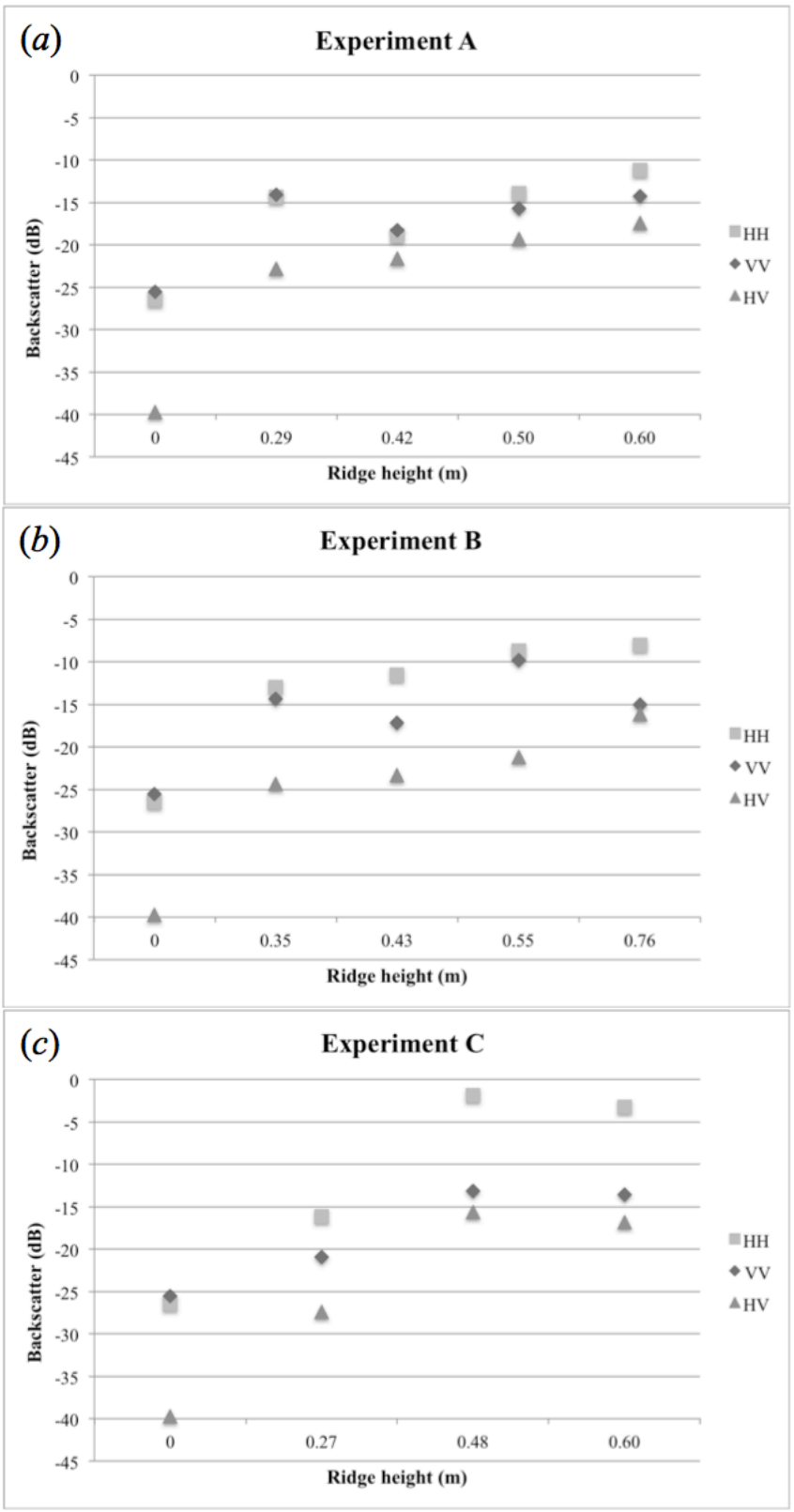

Figure 3.9. Plots of the HH, VV, and HV backscatter coefficients at an incidence angle of 40° for (*a*) experiment A, (*b*) experiment B, and (*c*) experiment C.

We determined that the polarization backscatter parameters (i.e. VV, HH, and HV) are the most precise for detecting variations in ridge height compared to the other polarimetric backscatter parameters examined in this paper, as there is a noticeable change in the backscatter coefficient when ridge height is changed. Each polarization was further examined with all combinations of ridge heights in order to determine that the cross-polarization (HV) and the co-polarization (HH) are the most precise backscatter parameters for identifying differences in ridge height, as there were the largest differences in backscatter between ridge heights with these polarizations. On average the HV backscatter coefficient increased 2.7 dB with increasing ridge height during experiments A-C, with a maximum increase of 14.4 dB between a ridge height of 0.27 and 0.48 m in experiment C. The HH backscatter coefficient increased on average 2.2 dB during experiments A-C, with a maximum increase of 20.8 dB between a ridge height of 0.35 m in experiment B and a height of 0.48 m in experiment C.

Each data combination was also examined to determine the optimal incidence angle for detecting variations in ridge height. It was determined that using an incidence angle of 30 or 40° produces the most precise results for identifying differences in ridge height. These incidence angles produce the largest differences in the backscatter coefficient between the combinations of ridge heights from experiments A-C for each polarization. HV and HH polarizations had the greatest average increase in the backscatter coefficient with increasing ridge height at 40°, while VV polarization had the greatest average increase at 30°. Based on the results of this study, using an incidence angle of 40° and a polarization of HV or HH will produce the most precise results for

detecting variations in ridge height. The differences between ridge heights at an incidence angle of 40° are displayed in Figure 3.9.

3.3.3 PCA and MRA Results

The R-square value from the MRA, which is the proportion of variance in backscatter explained by the independent variables (incidence angle, ridge height, and polarization), was 0.68 for experiment A, 0.75 for experiment B, and 0.63 for experiment C. The adjusted R-squared values were 0.67 for experiment A, 0.75 for experiment B, and 0.61 for experiment C. The average root mean squared error was 5.0 for the three experiments, showing that a significant proportion of the variance in the backscatter coefficient comes from these three independent variables.

The coefficients outputs from the MRA for each experiment and all of the experiments combined are shown in Table 3.4. The B values of the regression equation are used for predicting the dependent variable from the independent variable. For example, in the experiment A data in Table 3.4 the coefficient for incidence angle is -0.72, meaning that for every unit increase in incidence angle a 0.72 decrease in backscatter is predicted (with all other variables held constant). In each experiment, the ridge height coefficient is significantly greater than the incidence angle and polarization coefficients, with B values of greater than 21, meaning that ridge height is predicted to significantly change backscatter. An alpha value of 0.05 was used, where values less than 0.05 represent a significant linear relationship between the independent and dependent variables, meaning that the relationship deviates significantly from zero. The coefficient for incidence angle is not significantly different from zero in experiments A

and C, but is significantly different in experiment B and all of the experiments combined. All of the rest of the coefficients for the remaining variables are less than 0.05 and are therefore significantly different from zero. The 95% confidence interval for B can be used to examine the amount that the estimates of the coefficients values could vary. In experiments A, C, and all of the experiments combined, the largest 95% confidence interval range is ridge height, while for experiment B the largest range was the constant. In all cases greater Beta values are associated with greater t values and lower p-values. These results show that ridge height contributes the greatest to a change in backscatter for this dataset.

Table 3.4. Coefficients outputs from the MRA for each experiment and all of the experiments combined. The model column lists the constant (the predicted value of backscatter when all other variables are 0), and each independent variable. The unstandardized coefficients columns list the B values and the standard errors associated with the coefficients. The standardized coefficients columns list the Beta values, which are the coefficients values that would occur if all of the variables were standardized in the regression analysis. The t and Sig. columns list the t-statistic values and their associated 2-tailed p-values, which are used to test whether a coefficient is significantly different from zero. An alpha value of 0.05 was used. The 95% confidence interval for B columns list the lower and upper bounds for the coefficients.

Experiment A		Unstandardized Coefficients		Standardized Coefficients			95.0% Confidence Interval for B	
Model		B	Std. Error	Beta	t	Sig.	Lower Bound	Upper Bound
1	(Constant)	-17.053	2.203		-7.740	.000	-21.446	-12.660
	Incidence Angle	-.072	.037	-.132	-1.964	.053	-.145	.001
	Ridge Height	26.422	2.500	.708	10.570	.000	21.438	31.407
	Polarization	-3.828	.635	-.404	-6.026	.000	-5.095	-2.562
Experiment B		Unstandardized Coefficients		Standardized Coefficients			95.0% Confidence Interval for B	
Model		B	Std. Error	Beta	t	Sig.	Lower Bound	Upper Bound
1	(Constant)	-14.120	2.009		-7.029	.000	-18.126	-10.115
	Incidence Angle	-.109	.034	-.189	-3.231	.002	-.176	-.042
	Ridge Height	22.476	1.901	.693	11.822	.000	18.685	26.267
	Polarization	-4.876	.583	-.490	-8.358	.000	-6.039	-3.713
Experiment C		Unstandardized Coefficients		Standardized Coefficients			95.0% Confidence Interval for B	
Model		B	Std. Error	Beta	t	Sig.	Lower Bound	Upper Bound
1	(Constant)	-18.223	3.354		-5.433	.000	-24.942	-11.504
	Incidence Angle	-.038	.057	-.054	-.668	.507	-.153	.076
	Ridge Height	31.035	3.550	.709	8.743	.000	23.924	38.146
	Polarization	-4.321	.991	-.354	-4.362	.000	-6.306	-2.337
All Ridges (Experiments A-C)		Unstandardized Coefficients		Standardized Coefficients			95.0% Confidence Interval for B	
Model		B	Std. Error	Beta	t	Sig.	Lower Bound	Upper Bound
1	(Constant)	-14.930	1.744		-8.563	.000	-18.371	-11.489
	Incidence Angle	-.068	.027	-.131	-2.477	.014	-.121	-.014
	Ridge Height	21.008	2.052	.542	10.238	.000	16.958	25.058
	Polarization	-3.959	.473	-.443	-8.377	.000	-4.892	-3.027

In each case, the step-wise MRA results for each experiment removed the independent variables incidence angle and polarization, and the independent variable ridge height remained in the model.

The total variance outputs from the PCA from experiments A, B, and C using incidence angle, polarization, and ridge height to examine the backscatter coefficient, are shown in Table 3.5. For all three experiments only one component was extracted in each case, which was ridge height. When the data from all three experiments were combined (11 ridges in total), ridge height was the only component extracted, with a total extraction sums of squared loadings value of 1.71 and a percentage of variance of 42.8. This means that ridge height explains approximately 88% of the variability in the data, and is the only principal component in all of the datasets.

Table 3.5. The total variance outputs from the principal components analyses for Experiments A, B, and C. Components are the backscatter coefficient, incidence angle, polarization, and ridge height. For each component output there is an eigenvalue (in the initial eigenvalues columns, the total column sums up to the number of components). These eigenvalues represent the amount of variance in all of the variables accounted for by that component, and any eigenvalues over 1 are considered significant components. The percentage of variance column lists the ratio of variance accounted for by each component to the total variance (with all components included). The cumulative column shows the percentage of variance for each component and any components before it (cumulates down the column). The extraction sums of squared loadings column lists the extracted components.

Experiment A	Initial Eigenvalues			Extraction Sums of Squared Loadings		
Component	Total	% of Variance	Cumulative %	Total	% of Variance	Cumulative %
1	1.826	45.638	45.638	1.826	45.638	45.638
2	1.000	25.000	70.638			
3	1.000	25.000	95.638			
4	.174	4.362	100.000			
Experiment B	Initial Eigenvalues			Extraction Sums of Squared Loadings		
Component	Total	% of Variance	Cumulative %	Total	% of Variance	Cumulative %
1	1.870	46.738	46.738	1.870	46.738	46.738
2	1.000	25.000	71.738			
3	1.000	25.000	96.738			
4	.130	3.262	100.000			
Experiment C	Initial Eigenvalues			Extraction Sums of Squared Loadings		
Component	Total	% of Variance	Cumulative %	Total	% of Variance	Cumulative %
1	1.795	44.864	44.864	1.795	44.864	44.864
2	1.000	25.000	69.864			
3	1.000	25.000	94.864			
4	.205	5.136	100.000			

PCA were also run using other backscatter parameters as the dependent variable, with incidence angle and ridge height as the independent variables, to determine if ridge height is still the only principal component with different backscatter output parameters. Polarimetric parameters HV/HH, VV/HH, depolarization ratio, and VV-HH phase difference were used as dependent (target) variables and run in a separate PCA. The non-polarimetric parameter total power was also run as the output variable in a PCA. For each PCA all of the ridge data from each experiment (A, B, and C) were combined and

then analyzed. In each case only one principal component was extracted, which again was ridge height.

Ridge height is the only principal component in this dataset for all of the polarimetric parameters examined (VV, HH, HV, HV/HH, VV/HH, depolarization ratio, and VV-HH phase difference), as ridge height explains nearly 88% of variability in backscatter using the parameters in this study.

3.4 Conclusions

The goal of this paper was to use *in situ* data from a sea ice mesocosm facility (SERF) to examine C-band microwave scattering of artificially constructed sea ice ridges and how they respond based on changes to microwave and target parameters. The main conclusions are as follows.

High-resolution terrestrial LiDAR models can be used to precisely measure ridge heights relative to freeboard, ridge volume estimates, macro and micro-scale surface roughness, slope angles of sail blocks, and general slopes of the ridges. Target parameters of salinity, small-scale surface roughness, slope values, and approximate air space volumes in the bare ice ridges were found to be non-significant to the variability in microwave scattering.

As proven by the MRA, a significant proportion of the variance in the backscatter response comes from the incidence angle, ridge height, and polarization parameters. R-squared values representing the proportion of variance in backscatter explained by these three parameters were 0.68 for experiment A, 0.75 for experiment B, and 0.63 for experiment C.

Ridge height was the only principal component for each experiment, as well as all of the experiments combined, meaning that ridge height explains nearly 88% of variability in backscatter when incidence angle, polarization, and ridge height are used as independent variables. When different polarimetric (VV/HH, HV/HH, VV-HH phase difference, and depolarization ratio) and non-polarimetric (total power) parameters are used as the output variable, ridge height is still the only principal component extracted.

With a radar incidence angle range of 20 to 60° at 10° increments, there is a slight decreasing trend in the backscatter coefficient as incidence angle increases. Based on the results of this study, using an incidence angle between 30 and 50° will best enable distinguishing between smooth and ridged ice, while using an incidence angle of 40° will best enable detecting variations in ridge height.

A combination of copolarized and cross-polarized ridge backscatter responses were examined and it was found that HV polarization values were lowest 100% of the time, and VV polarization values were generally lower than HH polarization values (VV<HH 80% of the time) over ridges. When average change in backscatter between ridge heights was examined there were similar values in backscatter change for each polarization, which suggests that as long as polarization is held constant, or all polarizations are examined, polarization is likely not a significant contributing parameter to changing backscatter values in the case of ridges (strong volume scatterers such as ridges generally show no preferential scattering based on polarization). Based on the results of this study, using HV polarization will best enable distinguishing between smooth and ridged ice, while using a polarization of HV or HH will best enable detecting variations in ridge height.

Ridge height is the parameter that contributes most significantly to the backscatter response. The backscatter signal consistently increased on average 15.3 dB from a smooth ice surface up to an average ridge height of ~0.50 m 80% of the time in the three experiments used for this paper. Once the ridge heights were greater than ~0.50 m the backscatter returns were more variable, likely mainly due to an increasingly filled radar field of view. Also contributing to this variability could be the increased amount of randomly oriented surfaces, and the greater potential for volume scattering. The changes to the backscatter coefficient values become smaller with increasing ridge heights.

When examining ridges in cold temperatures with no snow cover, on average for this study, 69% of the variance in the backscatter responses can be explained by incidence angle, polarization, and ridge height, with almost 88% of the variability in the backscatter attributed to ridge height. Ridge height is the significant parameter affecting C-band microwave scattering for snow-free FYI ridges during winter. The experimental data collected at SERF in December 2013 and February 2014 provides a base of knowledge of how backscatter values change when specific ridge and radar parameters are changed.

Acknowledgments

This research was supported through funding from the Natural Science and Engineering Research Council of Canada (NSERC), a Canada Excellence Research Chair (CERC), a Canada Research Chair (CRC), and the Canada Foundation for Innovation (CFI). The authors would like the thank Jack Landy and John Iacozza for their continued support throughout the project, as well as the research team involved in the 2013-2014 SERF experiments. This work is a contribution to the Arctic Science Partnership (ASP) and the ArcticNet Networks of Centres of Excellence. This paper is dedicated to Dr. Klaus Hochheim, Captain Marc Thibault, and Daniel Dubé, who tragically lost their lives pursuing Arctic science.

Chapter Three References

Carlstrom A. (1995). Modelling microwave backscattering from sea ice for synthetic-aperture radar applications. *Chalmers University of Technology*, Technical Report 271: 1-23.

Carlstrom A. (1997). A microwave backscattering model for deformed first-year sea ice and comparisons with SAR data. *IEEE Transactions of Geoscience and Remote Sensing*, 35: 378-391.

Carlstrom A. and Ulander L.M.H. (1995). Validation of backscatter models for level and deformed sea-ice in ERS-1 SAR images. *International Journal of Remote Sensing*, 16: 3245-3266.

Carsey F.D., Barry R.G., and Weeks R.F. (1992). Introduction. In: Carsey F.D., Microwave remote sensing of sea ice. *American Geophysical Union*, 1-7.

Comiso J.C. and Hall D.K. (2014). Climate trends in the Arctic as observed from space. *Climate Change*, 5: 389-409.

Geldsetzer T., Mead J.B., Yackel J.J., Scharien R.K., and Howell S.E.L. (2007). Surface-based polarimetric C-band scatterometer for field measurements of sea ice. *IEEE Transactions on Geoscience and Remote Sensing*, 45 (11): 3405-3416.

Haas C., Liu Q. and Martin T. (1999). Retrieval of Antarctic sea-ice pressure ridge frequencies from ERS SAR imagery by means of *in situ* laser profiling and usage of a neural network. *International Journal of Remote Sensing*, 20 (15-16): 3111-3123.

Hudier E. and Larouche P. (2005). A potential of polarimetric SAR data in mapping first year sea ice pressure ridges from the coherent and non-coherent components of HH and VV channels. *European Association of Remote Sensing Laboratories Proceedings*, 4: 130-138.

Johannessen O.M., Shalina E.V., and Miles M.W. (1999). Satellite evidence for an Arctic sea ice cover in transformation. *Science*, 286 (5446): 1937–1939.

Johansson R. and Askne J. (1987). Modeling of radar backscattering from low-salinity ice with ridges. *International Journal of Remote Sensing*, 8: 1667-1677.

Kim Y.S., Moore R.K., Onstott R.G., and Gogineni S. (1985). Towards identification of optimum radar parameters for sea-ice monitoring. *Journal of Glaciology*, 31 (109): 214-219.

Landy J.C., Ehn J., Shields M., and Barber D.G. (2014). Surface and melt pond evolution on landfast first-year sea ice in the Canadian Arctic Archipelago. *Journal of Geophysical Research*, 119 (5): 3054-3075.

Landy J.C., Isleifson D., Komarov A.S., and Barber D.G. (2015). Parameterization of centimeter-scale sea ice surface roughness using terrestrial LiDAR. *IEEE Transactions on Geoscience and Remote Sensing*, 53 (3): 1271-1286.

Lensu M. (2003). The evolution of ridged ice fields. *Helsinki University of Technology Ship Laboratory*, 1-140.

Lubin D. and Massom R. (2006). Polar remote sensing (atmosphere and oceans). *Springer-Praxis Books in Geophysical Science*, 1: 309-616.

Onstott R.G. (1992). SAR and scatterometer signatures of sea ice. In: Carsey F.D., Microwave remote sensing of sea ice. *American Geophysical Union*, 73-104.

Onstott R.G., Moore R.K. and Weeks W.F. (1979). Surface-based scatterometer results of arctic sea ice. *IEEE Transactions on Geoscience Electronics*, GE-17 (3): 78-85.

Onstott, R., and Shuchman R. (2004). SAR Measurements of Sea Ice. *Synthetic Aperture Radar Marine User's Manual*. Washington, DC: National Oceanic and Atmospheric Administration.

Parashar S.K., Haralick R.M., Moore R.K., and Biggs A.W. (1977). Radar scatterometer discrimination of sea ice types. *IEEE Transactions on Geoscience Electronics*, GE-15 (2): 83-87.

Timco G.W., Croasdale K. and Wright B. (2000). An overview of first-year sea ice ridges. *Canadian Hydraulics Centre Technical Report HYD-TR-047*, 5 (112): 1-157.

Tucker W.B., Perovich D.K., Gow A.J., Weeks W.F., and Drinkwater M.R. (1992). Physical properties of sea ice relevant to remote sensing. In: Carsey F.D. Microwave remote sensing of sea ice. *American Geophysical Union*, 9-28.

Tucker W.B., Sodhi D.S. and Govoni J.W. (1984). Structure of first-year pressure ridge sails in the Prudhoe Bay region. In: Barnes P.W., Schell D.M. and Reimnitz E. The Alaskan Beaufort Sea: Ecosystems and environments. *New York Academic Press*, 115-135.

Wadhams P. (2000). Ice in the ocean. *Gordon and Breech*, 364.

Weeks, W. F., and Ackley S.F. (1986). The growth, structure and properties of sea ice. In: The geophysics of sea ice, NATO ASI Ser. B, edited by N. Untersteiner, Springer, New York (146): 9-164.

Woodhouse I.A. (2006). Introduction to microwave remote sensing. *CRC Press – Taylor and Francis Group*.

Chapter Four – A Remote Sensing Examination of Snow Cover Over First-Year Sea Ice Ridges

4.1 Introduction and Background

Snow cover plays a significant role throughout the Arctic system, particularly on sea ice. Snow cover contributes to the chemical, physical, and thermodynamic processes that are conducted across the ocean-sea-ice-atmosphere (OSA) interface (Barber and Nghiem, 1999; Maykut, 1982). In particular, snow cover plays a primary role in moderating or inhibiting gas, energy, mass, heat fluxes, and radiation transfer to the sea ice layer (Arons and Colbeck, 1995, Eicken *et al*., 1995; Eicken, 2003; Iacozza and Barber, 2010; Maykut, 1986). Snow cover has low optical transmissivity, creating high reflectivity (high albedo), and low thermal diffusivity (snow is a poor conductor of heat due to its large air content), meaning that snow will reflect up to 85% of incoming short-wave radiation, and significantly decrease the amount of sensible heat loss from the ocean, decreasing the rate of ice growth (Barry, 1996; Geiger, 1957; Grenfell and Maykut 1977; Sturm et al., 2002). The reduced conductive heat flux (due to the insulating properties of snow) and moderation of incoming short-wave radiation created by a snow cover, can significantly affect the magnitude and rate of ice formation, thickness, ablation, and melt (Barber et al., 1998; Curry et al., 1995; Iacozza and Barber, 2010; Maykut, 1978). A snow cover over sea ice controls the surface energy balance of the OSA and is highly variable spatiotemporally (Fuller et al., 2014; Maykut, 1986). The thermal conductivity of snow can be variable depending on the snow structure and density (Langlois et al., 2007), but a snow cover will consistently impede ice growth, delay ablation, and retard melt onset.

The roughness of an ice surface and the meteorological and physical conditions at the ice surface will determine the temporal evolution of a snow cover over sea ice. Snow cover will generally be thicker over rougher ice (as protruding ice from the surface will create a feature for wind-blown snow to pile up against), and will usually be thicker over older ice, due to increased accumulation time (Iacozza and Barber, 2010). Chapter 2 described first-year sea ice (FYI) ridge formation and discussed how sail blocks are angular and not uniformly oriented. This creates significant airspace between blocks on the surface that become filled with hardened, compressed snow over time due to wind and weathering. There is often a thick snow cover on the leeward side of pressure ridges due to drifting (Carsey et al., 1992). The snowdrifts along ridges become compacted over time due to wind and weathering, creating linear snow dunes called sastrugi (Armstrong et al., 1973; Hudier, 2006). Snow covers are generally very thick over pressure ridges, but in some cases can be thinner due to wind scouring. These thick snow covers over ridges have the potential to significantly affect microwave scattering.

Using microwave radar to measure backscatter properties of sea ice is useful due to its all weather and lighting capabilities, and due to distinctions between sea ice, snow, and open water electromagnetic properties (Barber, 2005). Sea ice microwave signatures are influenced by the propagation and attenuation of microwaves, which is determined by the dielectric properties of the ice and snow on the target surface (Petrich and Eicken, 2010). The physical ice conditions, environmental conditions, and the snow cover over the ice particularly influence microwave signatures of sea ice (Lubin and Massom, 2006). Microwave signature interaction with FYI is dominated by surface scattering at or near the ice surface (Onstott, 1992). Beaven et al. (1995) and Lytle et al. (1993) found

through laboratory studies of snow and non-snow covered smooth sea ice sheets that a snow cover increases the microwave backscatter response. Onsott (1992) found similar results in an Arctic study. An increase in dry snow cover did not significantly further change the backscatter response. Beaven et al. (1995) and Lytle et al. (1993) concluded that this backscatter increase was caused by salinity entering the snow layer, and an increase in the small-scale surface roughness due to the snow layer. In the case of ridges, the increased small-scale roughness that a snow layer creates will be insignificant in terms of backscatter responses, due to the large-scale roughness of the ridge, which will dominate. Also with ridges there will be zero to minimal brine expulsion at the surface of the sail blocks.

The impact snow on sea ice has on microwave scattering is determined by the temperature of the environment and the ice, and therefore the season. FYI is constantly changing over time and throughout the seasons, meaning that the scattering characteristics of the ice also change throughout the seasons and as the ice ages. The microwave signatures of ridges change with time, since the physical composition of the ice changes, and snow accumulates and then melts on the ice surface (Carsey et al., 1992; Onstott, 1992). The behavior of ridge scattering signatures can change significantly as temperature fluctuations occur throughout different seasons of the year (Richards, 2009). This chapter mainly examines winter ridges where temperatures are consistently below freezing, and briefly touches on ridge backscatter throughout the Arctic melt season. Essentially, scattering from the snow layer is dependent on salinity and liquid water content, which is temperature dependent.

At C-band, homogeneous dry snow is effectively "invisible" to microwaves due to low dielectric permittivity and small snow grains, allowing microwave energy to pass directly through the snow layer and then scatter at the snow-ice interface (Barber and Nghiem, 1999; Nghiem et al., 1995). At the snow-ice interface there is often a saline layer of depth hoar that contributes to the scattering response along with the sea ice surface (Barber and Nghiem, 1999; Crocker, 1992). In general, the small increases in backscatter that can occur from a dry snow cover can be considered negligible.

During the Arctic melt season snow becomes wet and often saline. When the wetness content of the snow is high, surface scattering from the snow plays a significant role, while when the wetness content of the snow is low (only a few percent), backscatter intensity will decrease due to attenuation (Carlstrom, 1995). The permittivity of ice and air is significantly lower than the permittivity of water, so the water content of the snow decides the dielectric properties of wet snow. The melting and freezing processes cause a metamorphism of the snow composition, changing the density of the snow, and therefore the response of the snow to microwaves (Carsey et al., 1992). During the melt season, a brine-enriched slush layer forms on the surface, due to brine expulsion and melting of the snowpack (Onstott, 1992). This slush layer further increases C-band microwave backscatter due to the increased salinity content. In the case of FYI ridges, the sail blocks become coated with moist snow, and in some cases this snow layer can mask the backscatter from the rough ice blocks, creating a very significant change in backscatter (Onstott, 1992). In general, microwave scattering from a wet snow cover depends on the wetness and salinity content at the surface.

In summary, a dry snow cover on a pressure ridge contains ice grains and air, while a wet snow cover contains ice grains, air, and liquid water and/or brine (if brine expulsion or flooding has occurred) (Carlstrom, 1995; Carsey et al., 1992). In the Arctic winter, the snow covering the ice surface is dry, allowing significant transmission of microwave energy to the ice surface, while in the Arctic spring, snow is wet and can scatter incoming microwave energy before it reaches the ice surface (Guneriussen, 1997).

This thesis examines C-band microwave scattering from FYI ridges during the winter season where no melt-freeze cycles are present, and therefore no metamorphism of the snow composition (snow is consistently dry). Microwave backscatter responses from FYI are a function of the physical snow and ice properties at the surface (i.e. surface roughness, orientation, and liquid water content), as well as a function of radar parameters (i.e. incidence angle, wavelength, and polarization) (Fuller et al., 2014; Onstott, 1992). Chapter 3 used *in situ* data from the Sea-ice Environmental Research Facility (SERF) to examine variations in C-band microwave backscatter from artificial sea ice ridges with changes in incidence angle, polarization, and ridge height. This chapter examines backscatter variations when a snow cover is added to the ridge, which was studied during experiment C at SERF (February 2014). A C-band scatterometer was used during the SERF study, which has a set wavelength, but the capability to collect data at multiple incidence angles and polarizations.

In May and June of 2012 a remote sensing study was completed in the Resolute Passage, Nunavut, Canada as part of the Arctic Ice-Covered Ecosystem in a Rapidly Changing Environment (Arctic-ICE) project, in order to examine landfast sea ice surface deformation in rubble ice fields. The objective of the study was to characterize sea ice

morphology and large-scale surface roughness during the cold, early melt, and advanced melt seasons, and then locate these small surface features in RADARSAT-2 satellite imagery. In May 2014 a laser scanning snow topography study was carried out in Dease Strait, Nunavut, Canada as part of the Ice Covered Ecosystem – CAMbridge bay Process Studies (ICE-CAMPS) project, in order to examine how the surface topography of slightly deformed ice changed throughout the month of May in Dease Strait. The LiDAR topographic surface measurements were acquired as a complementary dataset to a snow and ice thickness transect dataset.

This chapter uses data from the artificial ridge SERF study during February 2014 (described in Chapter 3), the remote sensing study during the Arctic-ICE program in the Resolute Passage, and the LiDAR study during the ICE-CAMPS program in Dease Strait, to examine how snow cover affects C-band microwave backscatter from ridges, and how different types of snow covers have the potential to change the surface topography and scattering response.

4.2 Data and Methods

4.2.1 Study Areas

In May 2014 a non-invasive slightly rough FYI sampling site was set up for modelling surface topography in Dease Strait, Nunavut at 69.03033°N, 105.352°W. The site was set up around a roughness feature on the surface of the ice and foot and snowmobile traffic were limited in the area surrounding the site. Three custom made platforms were frozen into the ice at locations that created the least amount of shadowing (data gaps) with LiDAR data collection. Three High Definition Surveying (HDS) targets

were frozen on tripods into the ice at locations that could be acquired with each scan. The non-invasive sampling site set up is shown in Figure 4.1 and a photograph of the laser scanner set up is shown in Figure 4.2. Physical sampling took place in an undisturbed area adjacent to each platform, and snow and ice thickness transects were collected in various areas outside the non-invasive sampling site (within 500 metres). Data was acquired opportunistically from May 5-22, 2014.

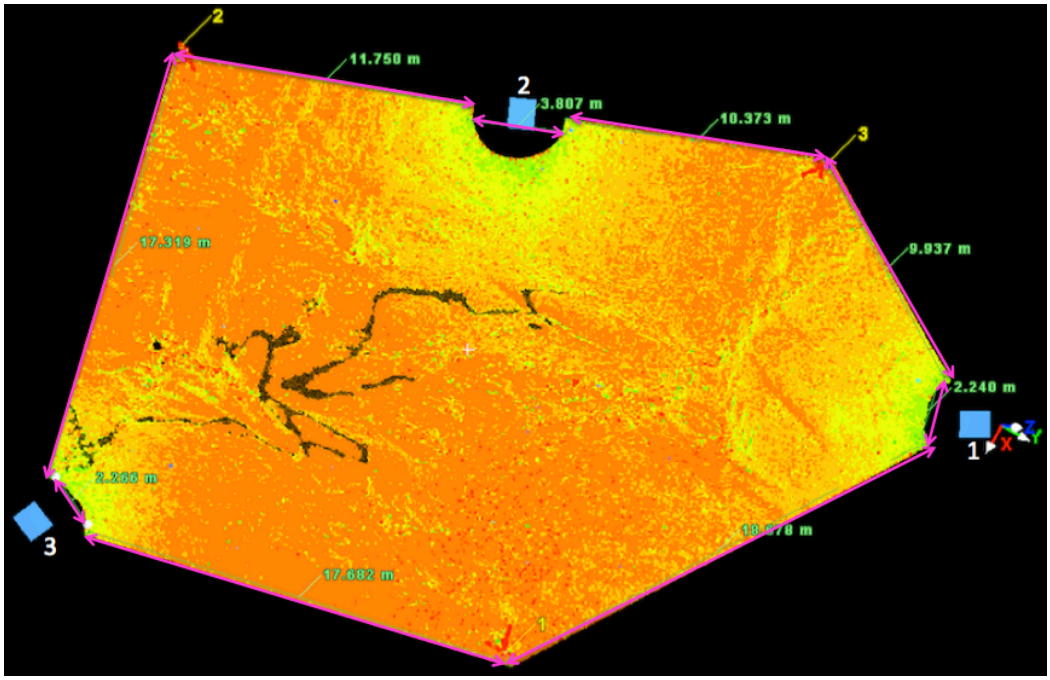

Figure 4.1. Point cloud model displayed by intensity of the non-invasive sampling site in Dease Strait. Scanning platform locations are shown in blue, and HDS target locations are shown as red tripods (yellow numbers point to the location). Measurement values around the sampling site are displayed in metres.

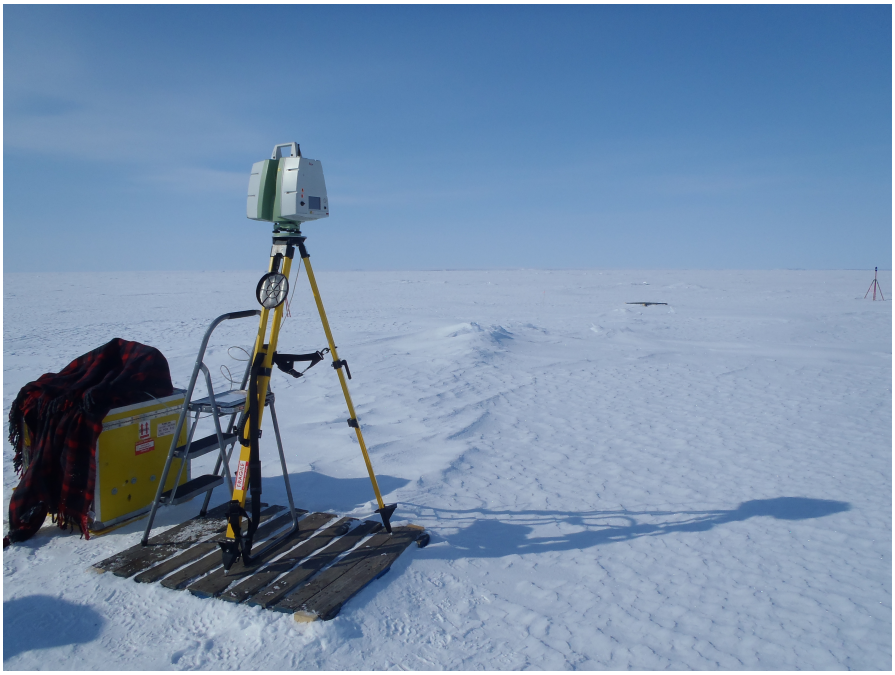

Figure 4.2. The LiDAR scanner set up on platform 3 at the non-invasive sampling site in Dease Strait. The small surface roughness feature is visible.

During the 2012 Arctic-ICE project in the Resolute Passage sampling was completed three times; once before the onset of melt, once during early melt, and once during advanced melt. Each sampling period was timed to RADARSAT-2 overpasses, in order to sample physical parameters as close as possible to the satellite acquisition time. The sampling dates were May 21, June 5, and June 20, 2012. Each rough ice site contained ridge features varying in size. A custom made movable platform was used for the LiDAR scanner and three or four scans were completed at each site to reduce shadowing. Again, HDS targets on tripods were acquired with each scan. An example of what the set up for these sampling sites looked like is shown in Figure 4.3, and site photographs from the three sites are shown in Figure 4.4. The coordinates for the corners of each site are shown in Table 4.1.

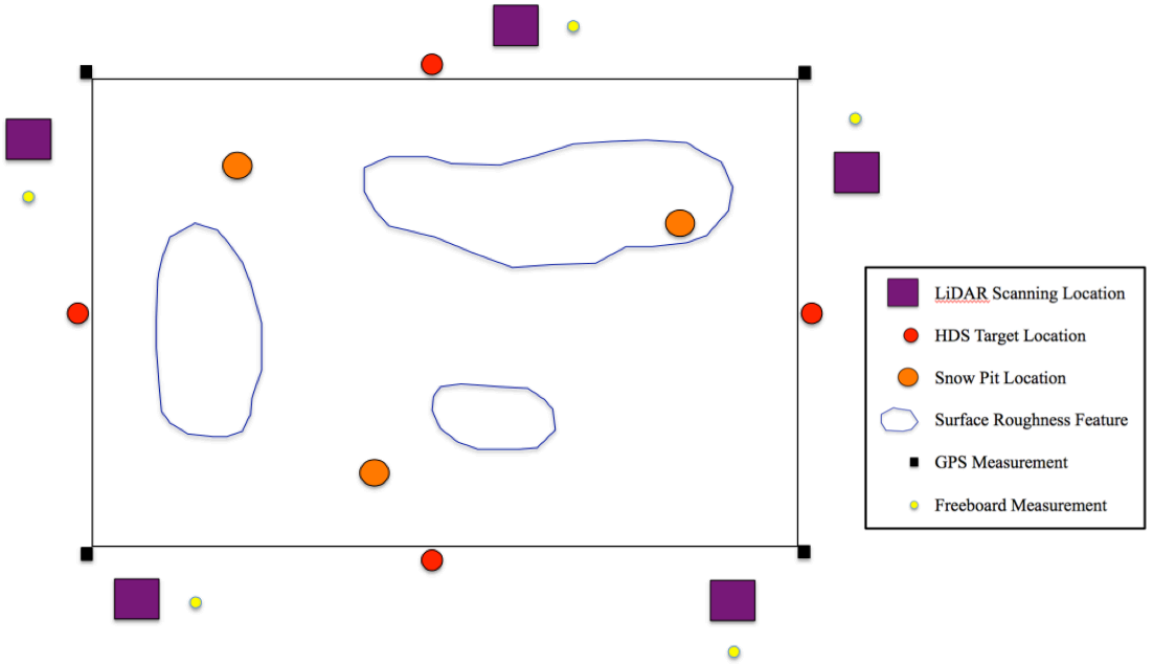

Figure 4.3. An example of what a rubble ice sampling site looked like during the Resolute Passage study. Each sampling site had a similar set up to this schematic.

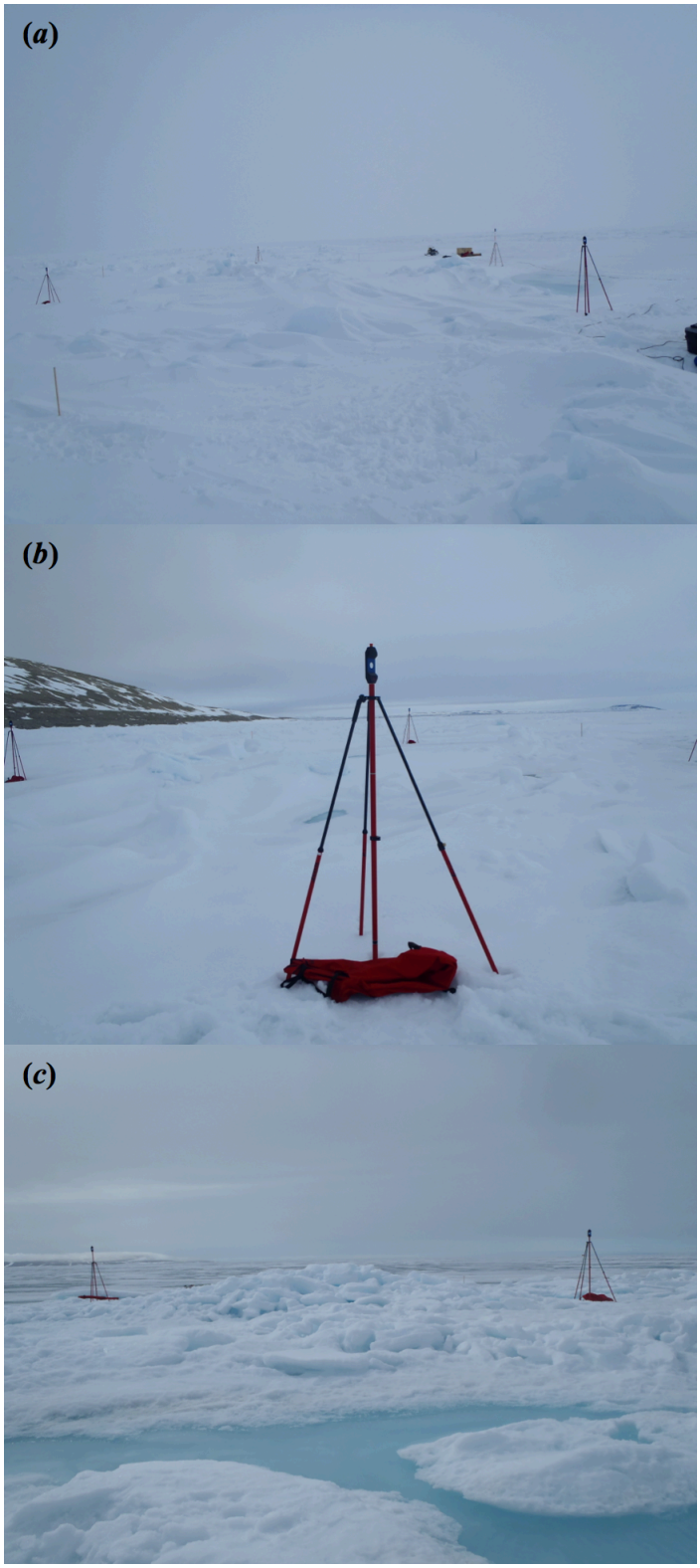

Figure 4.4. Site photographs from each sampling day; (*a*) the cold sampling period on May 21, 2012, (*b*) the early melt sampling period on June 5, 2012, and (*c*) the advanced melt sampling period on June 20, 2012. Red tripods are the HDS tripods and wooden stakes are the corners of the sampling sites.

Table 4.1. The GPS coordinates (written in decimal degrees) for each corner of the sampling sites in the Resolute Passage.

Sampling Site	Corner 1	Corner 2	Corner 3	Corner 4
Cold Season Site	74.74677°N 95.54524°W	74.74696°N 95.54529°W	74.74665°N 95.54371°W	74.74665°N 95.54379°W
Early Melt Season Site	74.74611°N 95.53435°W	74.74618°N 95.53421°W	74.74623°N 95.53514°W	74.74606°N 95.53522°W
Advanced Melt Season Site	74.73240°N 95.50858°W	74.73251°N 95.50827°W	74.73242°N 95.50759°W	74.73232°N 95.50779°W

The study area for the artificial ridge SERF study during February 2014 is described in Section 3.2.1 of Chapter 3. Figure 3.1 depicts the sampling set up and Figure 3.2 is a photograph of an artificial pressure ridge with the remote sensing instrumentation scanning the ridge. During experiment C, each ridge was sampled as a bare-ice ridge and as a snow-covered ridge. Each ridge height was sampled exactly the same with and without a snow cover for comparison purposes. Snow could not be blown over the ridges due to a missing piece of equipment on a snowmaking machine, so instead snow was added to the bare ice ridges by shoveling snow on top of the ridges, as well as through natural snowfall in one case. Figure 4.5 shows an artificial ridge covered in snow (snow was a combination of shoveling and snowfall).

Figure 4.5. An artificial ridge with snow cover sampled during experiment C at SERF. Snow was shovelled on to the ridge, and approximately 10 cm of snow fell and accumulated over and around the ridge before sampling.

Figure 4.6. Map of Canada depicting where each study site was located (modified from Google Maps™). Study site locations are labeled with black dots outlined in pink.

4.2.2 Radar Parameters

The C-band microwave scatterometer used to examine *in situ* backscatter during the SERF study is described in Section 3.2.2 of Chapter 3. During the Resolute Passage experiment a scatterometer was not available for *in situ* microwave measurements, so RADARSAT-2 fine-beam images were acquired just before LiDAR and physical sampling took place. The specifications for the scatterometer used in the SERF study and the RADARSAT-2 satellite used in the Resolute Passage study are shown in Table 4.2. The RADARSAT-2 images were collected on May 21, 2012 at 23:24 UTC during the ascending pass, on June 5, 2012 at 23:49 UTC during the ascending pass, and on June 20, 2012 at 12:51 UTC during the descending pass. The raw microwave images were post-processed in Nest 4C 1.1 software. The images were undersampled (2 by 2), calibrated to σ°, converted from slant range to ground range, had 3 by 3 mean speckle filters applied, and then were georeferenced to the UTM Zone 15N (WGS 1984) projection. The GPS positions from the corner of each site were used to identify the pixels where the sites were located in the post-processed satellite imagery. The images had a 25 m pixel size, and each site ended up covering portions of four pixels. Each pixel was expressed as σ° and measured in power form (intensity), which was then converted to decibels to get a scattering coefficient value for each site pixel.

Table 4.2. Specifications for the microwaves scatterometer used in the SERF study, and the RADARSAT-2 sensor used in the Resolute Passage study.

	Scatterometer	**RADARSAT-2 Sensor**
Antenna Height	2.14 m	798 km
Microwave Band	C-Band	C-Band
Centre Frequency	5.5 GHz	5.4 GHz
Bandwidth	500 MHz	100 MHz
Polarization	HH, VV, HV, VH	HH, VV, HV, VH

4.2.3 Target Parameters

The LiDAR laser scanner used to model the surface of each sampling site in all three studies is described in Section 3.2.2 of Chapter 3. Three HDS targets were used in the Dease Strait study, four in the Resolute Passage study, and two in the SERF study. A summary of dates that 5 mm resolution scans were acquired in Dease Strait is shown in Table 4.3. One 5 cm resolution LiDAR model was created each sampling day in the Resolute Passage. LiDAR data acquisition for the SERF study is described in Section 3.2.2 of Chapter 3. During SERF experiment C, LiDAR models were acquired of each ridge with and without snow cover. Freeboard was measured relative to the height of the scanner during each study, so that surface roughness heights relative to freeboard could be calculated from the LiDAR models.

Table 4.3. The acquisition dates of LiDAR data in Dease Strait. Scan 1 is the scan from platform 1, Scan 2 the scan from platform 2, and Scan 3 the scan from platform 3. Scans 2 and 3 were not acquired on May 10th due to a snowfall event (surface topography was altered).

Acquisition Date	Scan 1	Scan 2	Scan 3
May 5 and 6, 2014	Acquired May 5	Acquired May 5	Acquired May 6
May 10, 2014	Acquired May 10	Scan not acquired	Scan not acquired
May 12 and 13, 2014	Acquired May 12	Acquired May 12	Acquired May 13
May 17 and 18, 2014	Acquired May 17	Acquired May 17	Acquired May 18
May 22, 2014	Acquired May 22	Acquired May 22	Acquired May 22

The LiDAR models from each study were post-processed using Cyclone 9.0, Quick Terrain (QT) Modeler 7.1.6, and ArcGIS 10.2.2. The Dease Strait data used above ground level (AGL) analysis and continuous filtering to filter out precipitation and any other unwanted artefacts. Gridded surfaces with a grid sampling of 0.01 m, and a smoothing filter Z tolerance of 0.01 m were created, and elevation and surface volume changes between models were calculated to examine snowfall, drift, and erosion.

Changes between models greater than 5% were calculated, and the surface areas of these areas of significant change (>5%) were measured. The Resolute Passage data were cleaned up of precipitation and unwanted artefacts, and then made into gridded surfaces with grid sampling of 0.01 m spacing, and smoothing filter Z tolerances of 0.01 m. LiDAR post-processing for the SERF study is described in Section 3.2.2 of Chapter 3.

During the Dease Strait study, ice thicknesses and snow depths were measured adjacent to each platform as each LiDAR scan was taken. A meteorological tower was set up approximately 5 km away from the sampling site in Dease Strait, and so the data from this tower is not very useful, as it is not localized. In the Resolute Passage study various physical sampling was completed, including snow and pond depth transects throughout the sites (to obtain a minimum of 50 surface depth samples), sail block salinity measurements, sail block orientations were noted, and snow pits were taken in areas of different snow cover to examine snow structure properties, such as temperature, density, salinity, surface roughness, and grain size. An ice core was taken at each sampling site using a Kovacs Mark II 9 cm diameter ice core barrel to examine temperature and salinity profiles through the ice column. The physical and meteorological sampling from the SERF experiment is described in Section 3.2.2 and Table 3.1 of Chapter 3. During each study, ice temperatures were measured using a Traceable® Digital Thermometer temperature probe, which is accurate to ±0.1°C, and salinity values were measured using a Hach SensION5 conductivity metre, which is accurate to ±0.01 practical salinity units (psu). During the Resolute Passage study YSI 44212 Thermilinear Probes, which contain Vaisala capacitive relative humidity sensors

and 44212 thermistors housed in 41003-X 10 plate grill radiation shields, measured air temperature and relative humidity at 2 and 4 m above the ice surface.

4.2.4 Statistical Analysis

Basic statistical analysis was run on all of the data to determine significant variables and trends. Principal Components Analysis (PCA) was run on the experiment C SERF data using the independent variables incidence angle, polarization, ridge height, and snow cover, and the dependent variable the backscatter coefficient, to determine which independent variables are significant in changing the backscatter received by the scatterometer. PCA is a statistical factor analysis that breaks down a group of variables from a dataset into a smaller group of variables that represent a majority of the information in the original dataset. This type of factor analysis reduces the dimensionality of the original dataset and highlights which variables contribute the most to the outcome of the dataset (Dunteman, 1989). A multiple regression analysis (MRA) was run using the independent variables incidence angle, polarization, ridge height, and snow cover, and the dependent variable the backscatter coefficient, to further examine the relationship the independent variables have with the dependent variable. A MRA is useful for understanding how the dependent variable changes when the independent variables are changed. A step-wise MRA was also run on the data to determine which independent variables explain a significant portion of variability in a dependent variable. This type of regression analysis runs a sequence of f-tests and uses backward elimination where all the independent variables are included in the model at the start, and then

removed as the model is run, until only the independent variables that improve the model remain.

4.3 Results and Discussion

4.3.1 Dease Strait

During the time period of the Dease Strait study (May 5-22, 2014), the ice continuously grew, and snow depths generally increased at measurement sites due to snowfall events. Table 4.4 shows ice and snow thicknesses adjacent to platforms during scanning. Snow depth decreased adjacent to platform 1 from May 12 to 17, likely due to wind erosion. A continuous growth of ice was expected for this time period as temperatures were consistently below freezing.

Table 4.4. Snow and ice thickness values measured adjacent to scanning platforms during each LiDAR scan acquisition of the 2014 Dease Strait study.

	Snow Thickness (cm)			Ice Thickness (cm)		
Date	Platform 1	Platform 2	Platform 3	Platform 1	Platform 2	Platform 3
May 5	25	20		171	175	
May 6			14			181
May 10	26			172		
May 12	29	22		172	178	
May 13			16			184
May 17	24	22		174	179	
May 18			18			192
May 22	27	23	18	193	187	212

The digital elevation models (DEMs) and gridded surface elevation models for each sampling date produced from the LiDAR data are shown in Figure 4.7. For the DEMs (left images), brighter values equal higher surface topography, and for the surface elevation models (right images), red represents areas of highest elevation, and dark blue

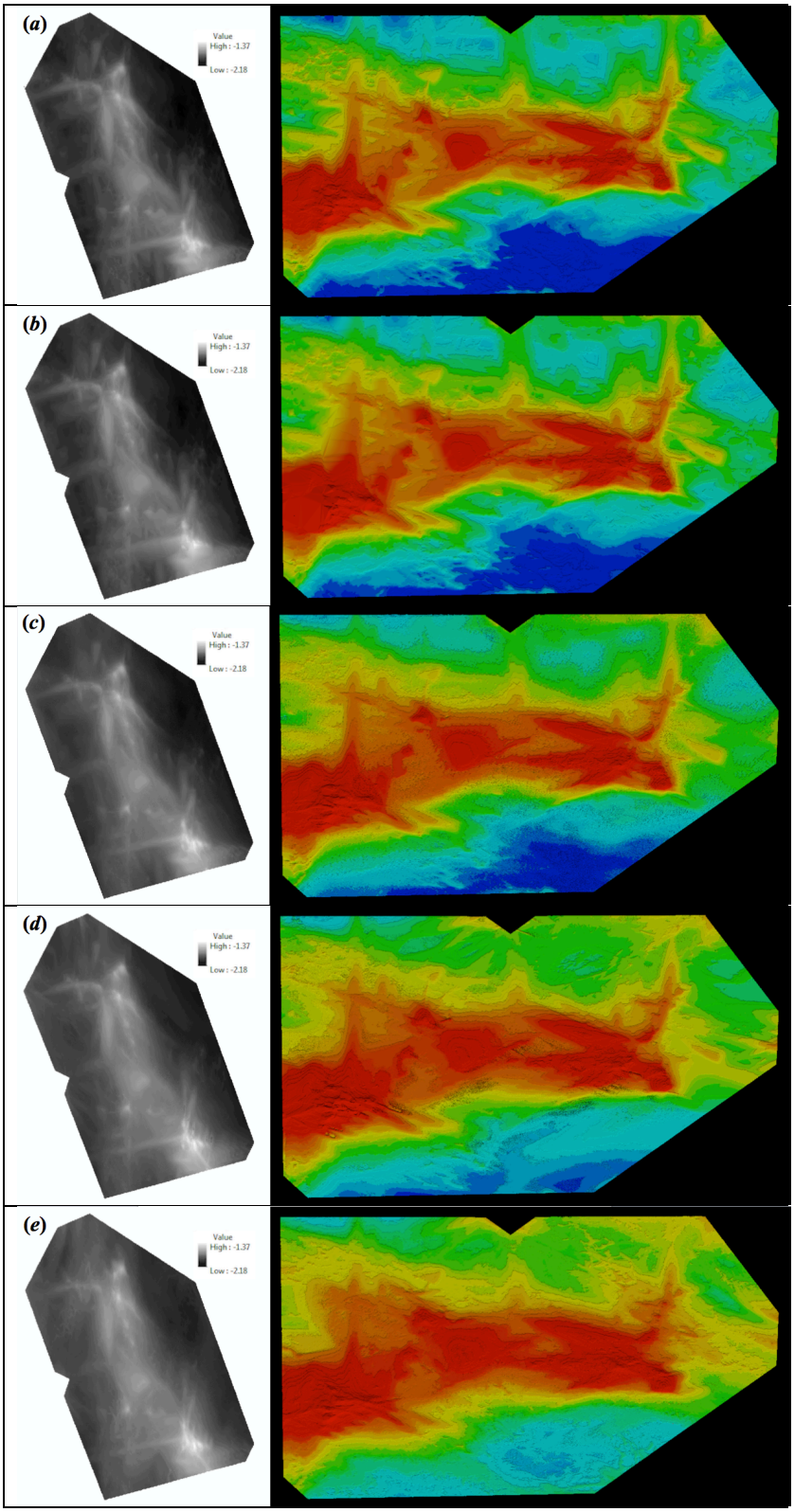

Figure 4.7. DEMs (left) and gridded surface elevation models (right) created from LiDAR data for (*a*) May 5/6, (*b*) May 10, (*c*) May 12/13, (*d*) May 17/18, and (*e*) May 22. Red represents areas of highest elevation, and blue lowest elevation.

areas of lowest elevation. The elongated surface roughness feature is located in the highest elevation area. It is apparent that snow depth increased over the sampling period, as areas of lowest elevation increased significantly, and areas of highest elevation increased slightly. Figure 4.8 shows change in snow cover for the sampling site between each sampling date. Areas outlined in black within the site represent areas with a change greater than 5%. There was no significant snow erosion (or melt), and snow generally increased across the sampling site throughout May. Figure 4.9 is the surface change model from the first day of sampling to the last. Again, areas outlined in black within the site represent areas that had a surface change greater than 5%. Figures 4.8 and 4.9 show that the majority of significant change (greater than 5%) during the study occurred alongside the surface roughness feature, as snow generally drifted up against it. The total surface areas with a change greater than 5% between sampling dates are shown in Table 5.5. The greatest increases in surface topography occurred from May 12 to 22, due to a large snowfall event. The total surface area with a change greater than 5% during the entire study was 359 m^2. Table 5.5 also shows the change in surface volume over the entire non-invasive site between measurement dates. The surface volume continuously increased over the study period, with a total increase of 1.62 m^3 during the sampling period.

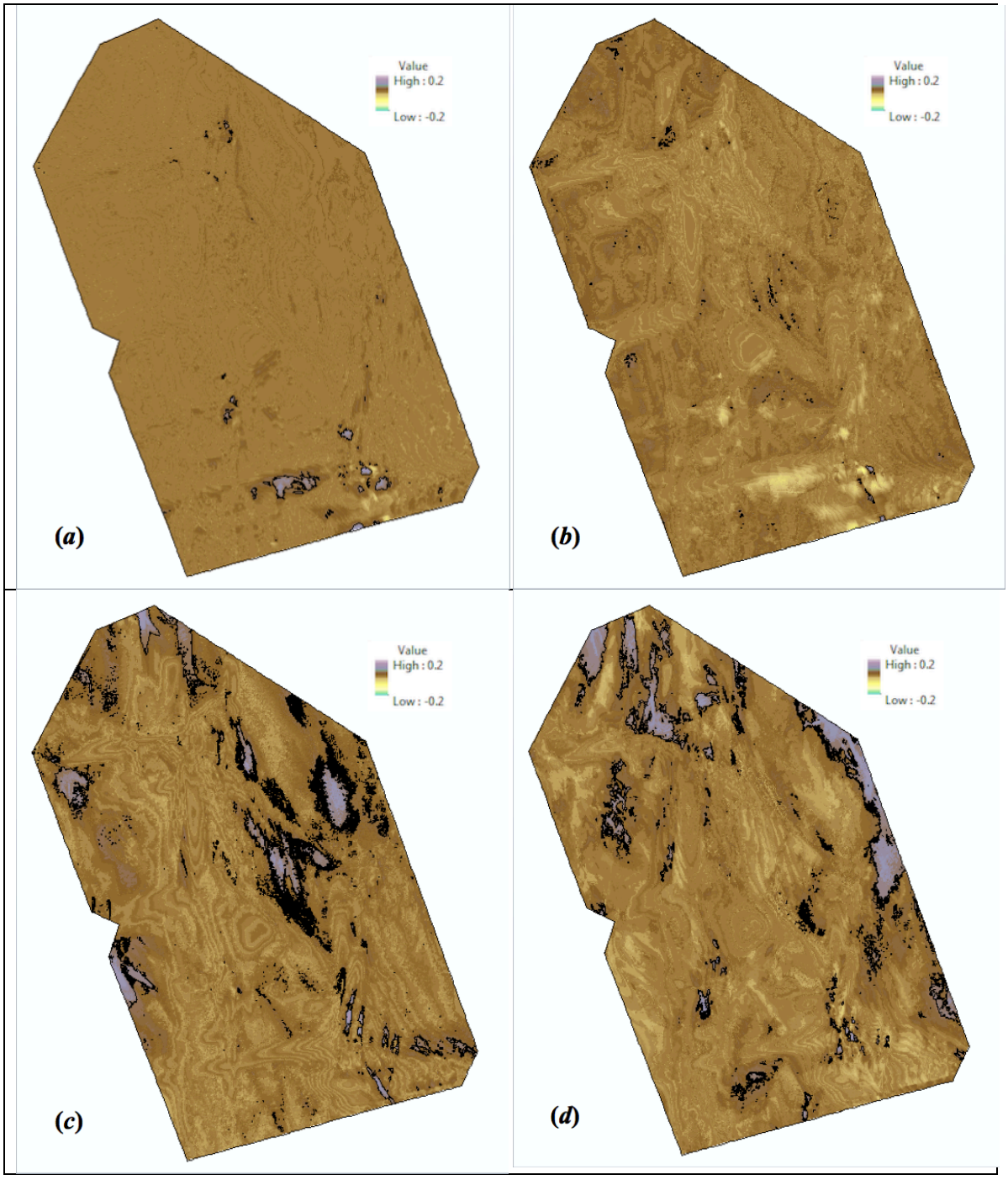

Figure 4.8. Surface change models created from LiDAR data for the surface change between (*a*) May 5/6 and May 10, (*b*) May 10 and May 12/13, (*c*) May 12/13 and May 17/18, and (*d*) May 17/18 and May 22. Areas outlined in black represent a change of greater than 5% between the sampling dates.

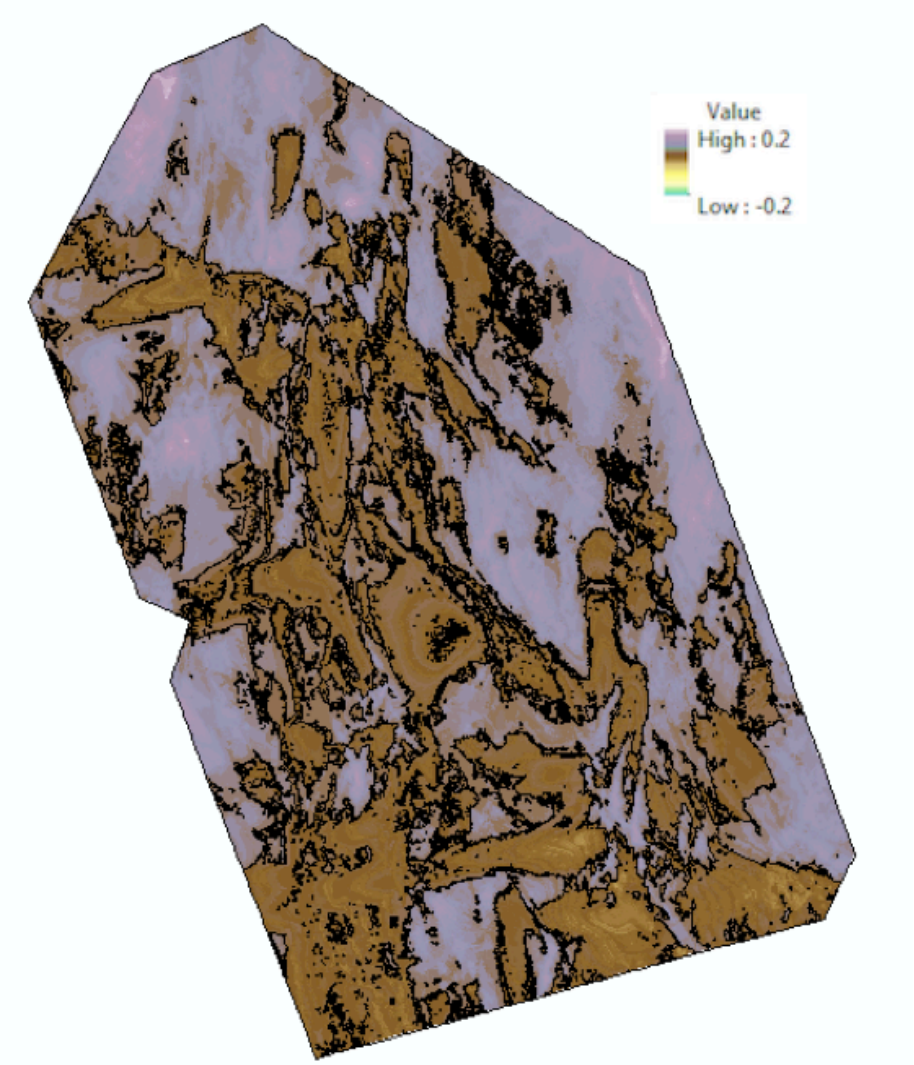

Figure 4.9. Surface change model created from LiDAR data for the surface change during the entire Dease Strait sampling period (May 5 to 22, 2015). Areas outlined in black represent a change of greater than 5% during the study.

Table 4.5. Total surface area with a change greater than 5%, and change in surface volume between Dease Strait site measurements.

	Total area with a change greater than 5% (m^2)	Change in volume of the entire study site (m^3)
May 5/6 to May 10	3.97	0.0550
May 10 to May 12/13	0.783	0.538
May 12/13 to May 17/18	37.4	0.340
May 17/18 to May 22	43.0	0.684

The data collected and processed from the non-invasive sampling site in Dease Strait in May 2014 show that even very small roughness features on an ice surface can cause snow to drift and build up in an elongated fashion against the roughness feature. This significantly changes the surface composition and topography of localized areas. In the case of ridges, which are considered very large roughness features in terms of FYI, this drifting of snow is even more pronounced (especially over the time period of an entire winter). Since snow has the potential to affect backscatter from ridges, snow drifting over and against ridges could significantly change microwave backscatter responses.

4.3.2 Resolute Passage

During the sampling times for the Resolute Passage study, physical and meteorological parameters were collected, which are summarized in Table 4.6. Air temperature was measured every minute at heights of 2 and 4 m above the ice surface at a meteorological tower approximately 2 km away from the sampling sites. Air temperatures averaged from minute readings are shown in Table 4.6. As expected for the time period, air temperature increased throughout the melt season and snow depth decreased. A range of salinity values were found in the snow at the May 21 sampling site due to an unexpected short warming period mid-May, when some surface melting occurred, and then was re-frozen when temperatures dropped back below freezing. During this brief warming event, brine expulsion at the surface likely occurred, creating a saline snow-ice interface. Some of this salinity would have been expelled or wicked into the snow layer, creating the range of snow salinity values. May 21 surface

Table 4.6. Physical and meteorological parameters collected at the three rubble ice sites during the Resolute Passage study.

	May 21 Site	**June 5 Site**	**June 20 Site**
Air Temperature Mean at 1 m (°C)	-5.13 ± 0.754	0.800 ± 0.400	1.38 ± 0.187
Air Temperature Mean at 4 m (°C)	-5.19 ± 0.757	0.710 ± 0.390	1.31 ± 0.202
Snow Depth Range (cm)	0 – 122	0 – 65	2 – 20
Snow Depth Mean (cm)	43.1 ± 24.0	18.6 ± 14.2	7.69 ± 6.33
Snow Salinity Range (‰)	0.10 – 7.0	All Values were 0	All Values were 0
Snow Salinity Mean (‰)	1.6 ± 1.6	0 ± 0	0 ± 0
Pond Depth Range (cm)	No Melt Ponds	10 – 14	6 – 15
Pond Depth Mean (cm)	No Melt Ponds	11.6 ± 1.82	10.3 ± 2.98
Pond Salinity Range (‰)	No Melt Ponds	5.3 – 13	0 – 0.40
Pond Salinity Mean (‰)	No Melt Ponds	10 ± 3.3	0.20 ± 0.13
Sail Block Volume Range (cm^3)	3600 – 387600	12920 – 7564000	2880 – 1172080
Sail Block Volume Mean (cm^3)	150814 ± 114247	769341 ± 1559040	107706 ± 282585
Sail Block Salinity Range (‰)	No Data	0 – 0.100	All Values were 0
Sail Block Salinity Mean (‰)	No Data	0 ± 0.0435	0 ± 0

scrapes of relatively smooth ice in the sampling site were a mean of 8.40 ± 7.89‰, with a minimum value of 1.9‰, and a maximum value of 19‰. Ponding began after May 21, but before June 5, as a few small, shallow melt ponds were present in the June 5 sampling site (can be seen in Figure 4b). Melt ponds increased significantly in size and numbers between June 5 and 20, and were drained almost completely of salinity content. On June 20 the top 5 cm of the ice core was 0‰, as significant brine drainage had occurred. The volumes of sail blocks were variable at each site, which is expected for a FYI ridge. 60%

of the sail blocks sampled were flat relative to the ice surface, while 40% were tilted. Sail blocks were almost completely drained of salinity content during the melt season.

Figures 4.10 and 4.11 show intensity and elevation images created from the LiDAR data of the June 5 and 20 sampling sites. The ridges at the June 20 sampling site were larger than the June 5 site. The areas of lowest elevation were deeper and wider at the June 20 site, as melt ponds had spread outwards and deepened downwards into the ice. The elevation differences between the two sites are highlighted at a different angle in Figure 4.12. As the melt season progressed, ridges protruded more on the surface and were more easily identifiable, due to a greater topographic difference (i.e. snow had significantly melted and melt ponds had formed).

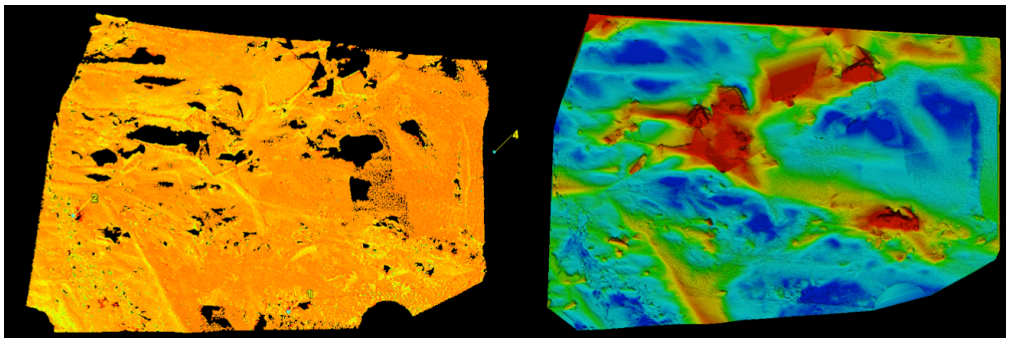

Figure 4.10. Images created from LiDAR data displayed by intensity (left) and elevation (right) for the June 5 sampling site. Red represents areas of highest elevation, and dark blue lowest elevation.

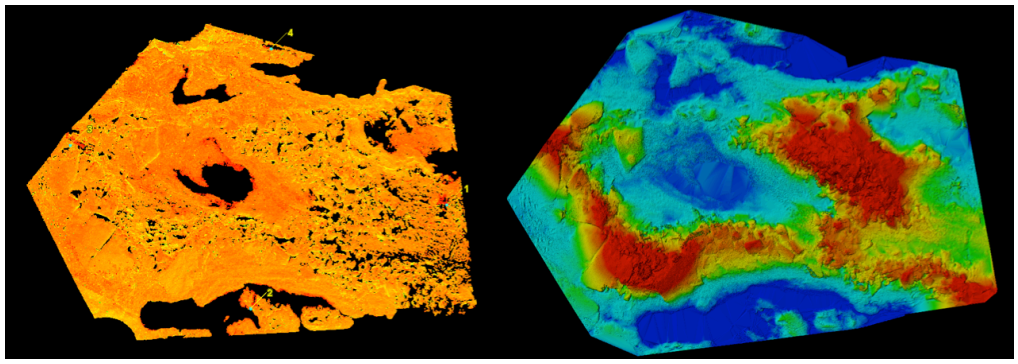

Figure 4.11. Images created from LiDAR data displayed by intensity (left) and elevation (right) for the June 20 sampling site. Red represents areas of highest elevation, and dark blue lowest elevation.

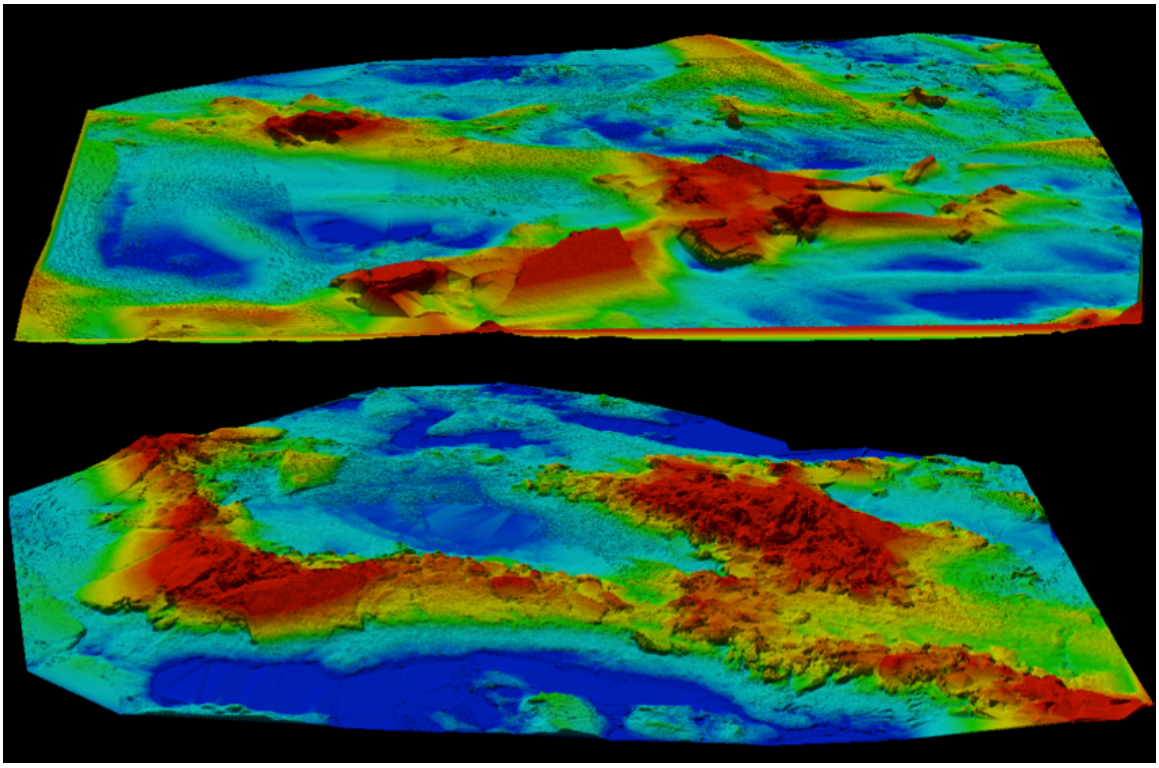

Figure 4.12. Elevation models created from LiDAR data for June 5 (top) and June 20 (bottom).

Figures 4.13 (May 21), 4.14 (June 5), and 4.15 (June 20) show the post-processed RADARSAT-2 images displayed by intensity from each sampling date for each polarization (VV, HH, HV, VH). The sampling sites were located within four pixels displayed within the red circles. It is obvious from examining these images that using different polarizations produces different images, and therefore different microwave scattering responses. The scattering coefficient (σ°) values associated with each pixel containing a portion of a sampling site are shown in Table 4.7. The cross-polarized values are greater than the co-polarized values as expected, however there are some extremely high HV and VH values for May 21. Table 4.8 shows the average scattering coefficient values for each sampling site. The average scattering coefficient increased throughout the sampling period for copolarized responses, with a greater increase in

backscatter after melt onset. This is likely due to the increased wetness and salinity content of the surface, which as previously mentioned increases microwave backscatter. The average cross-polarized responses are more variable due to the five high values seen in the May 21 sampling site, however if these values are removed, the scattering coefficient also consistently increases throughout the sampling period.

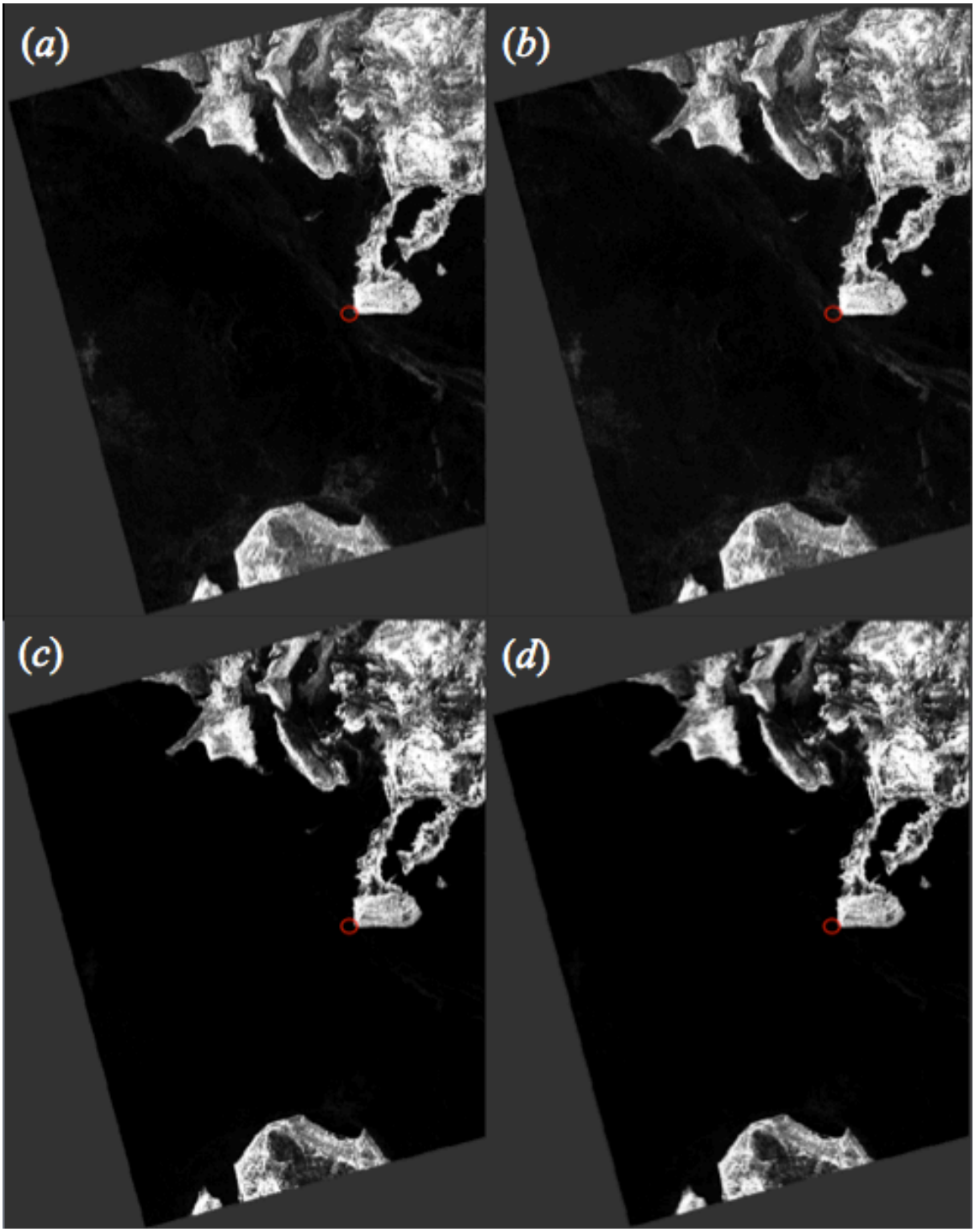

Figure 4.13. Post-processed RADARSAT-2 images displayed by intensity (power) for May 21; (*a*) VV, (*b*) HH, (*c*) HV, and (*d*) VH polarization. Pixels containing the sampling site are located within the red-circled areas. Images were acquired at an average incidence angle of 35.4°.

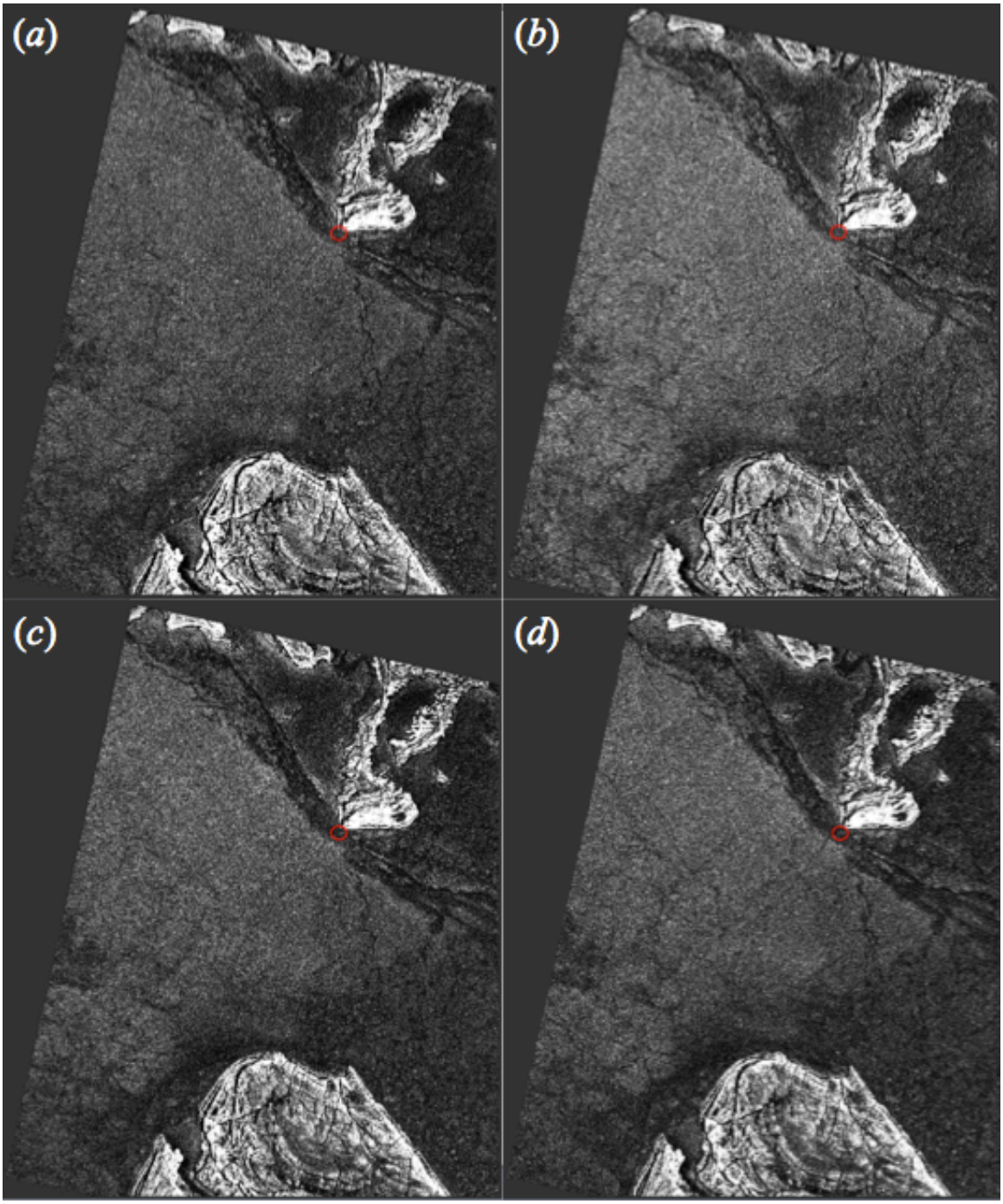

Figure 4.14. Post-processed RADARSAT-2 images displayed by intensity (power) for June 5; (*a*) is VV, (*b*) HH, (*c*) HV, and (*d*) VH polarization. Pixels containing the sampling site are located within the red-circled areas. Images were acquired at an average incidence angle of 46.8°.

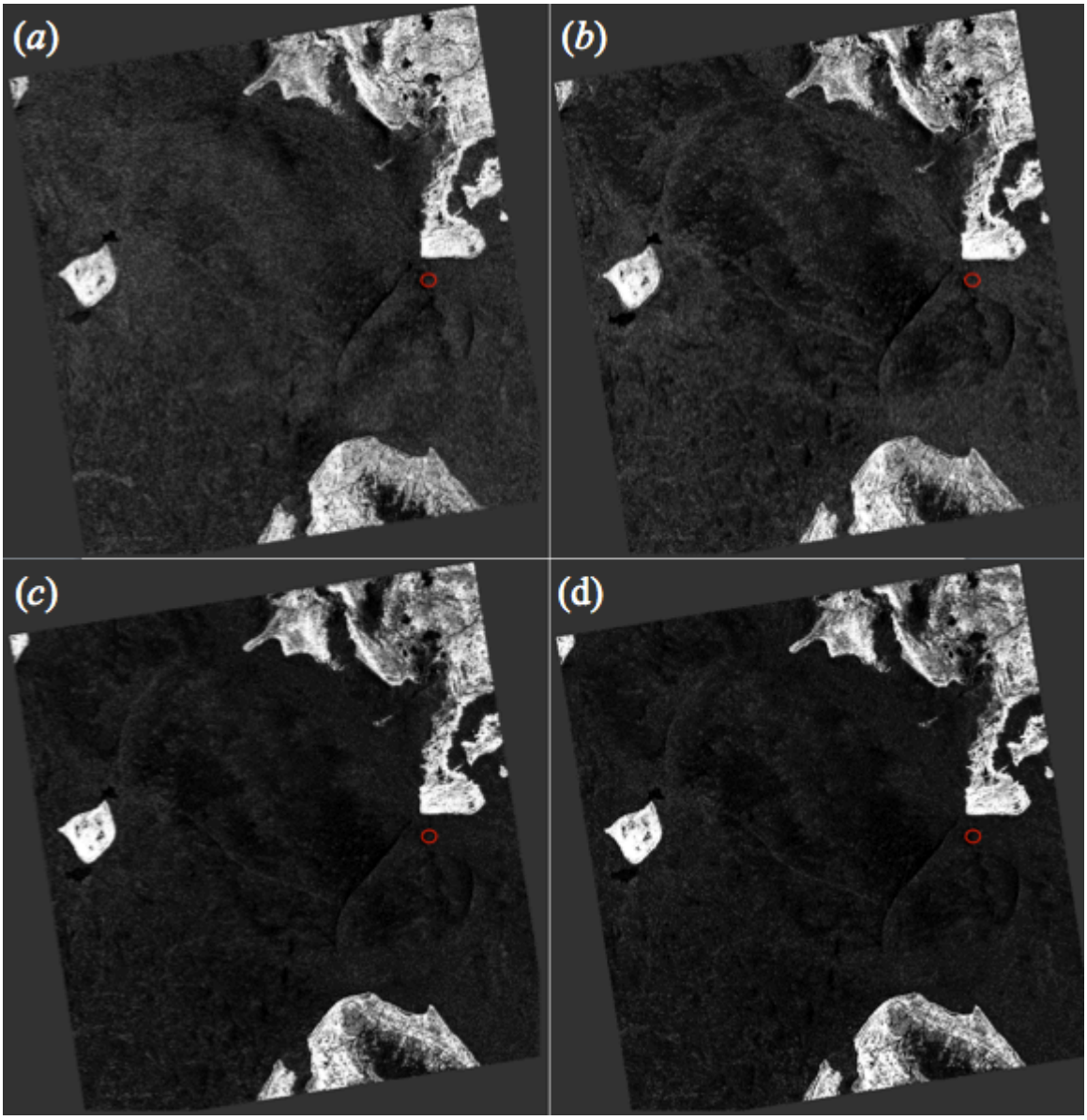

Figure 4.15. Post-processed RADARSAT-2 images displayed by intensity (power) for June 20; (*a*) is VV, (*b*) HH, (*c*) HV, and (*d*) VH polarization. Pixels containing the sampling site are located within the red-circled areas. Images were acquired at an average incidence angle of 44.7°.

Table 4.7. The scattering coefficient values for each polarization associated with each pixel (labelled A to L), containing a portion of a sampling site.

		VV (dB)	HH (dB)	HV (dB)	VH (dB)
May 21	Pixel A	-18.8	-18.7	8.37	-29.7
	Pixel B	-19.8	-19.9	8.80	-29.9
	Pixel C	-19.3	-17.9	-30.0	9.58
	Pixel D	-19.1	-18.9	9.10	9.74
June 5	Pixel E	-20.1	-20.5	-28.9	-26.6
	Pixel F	-19.5	-18.2	-27.6	-26.7
	Pixel G	-16.4	-16.4	-27.9	-25.6
	Pixel H	-17.9	-16.9	-27.6	-25.6
June 20	Pixel I	-15.4	-15.6	-26.6	-26.9
	Pixel J	-4.75	-16.2	-25.5	-25.8
	Pixel K	-15.5	-16.6	-25.3	-25.9
	Pixel L	-15.7	-16.9	-27.2	-25.9

Table 4.8. The average scattering coefficient values for each Resolute Passage sampling site.

Average σ°	VV (dB)	HH (dB)	HV (dB)	VH (dB)
May 21	-19.3	-18.8	-0.928	-10.1
June 5	-18.5	-18.0	-28.0	-26.2
June 20	-12.8	-16.3	-26.2	-26.1

The data collected and processed from the Resolute Passage in May and June 2012 show that throughout the Arctic spring microwave backscatter responses from areas of ridged ice will change temporally, due to changes in air temperature, snow cover, surface salinity content, and the wetness content at the surface. In general, the scattering coefficient will increase over ridges throughout the melt season.

4.3.3 Sea-ice Environmental Research Facility

The data and results from the December 2013 and February 2014 SERF experiments with no snow cover were examined in depth in Chapter 3. The February 2014 experiment (called experiment C) also measured microwave backscatter from the same ridges with and without a snow cover. Figure 4.16 shows the LiDAR models from

the SERF experiment with and without a snow cover. Unfortunately due to an equipment issue during the SERF study, snow could not be blown over the ridges to mimic natural snowdrifts, and so snow was shoveled on top of the ridges instead. This created a snow cover that was not blown across the ridge, like would be seen in the Arctic. Between sampling the second ridge height (0.48 m) with no snow cover and with a snow cover, it snowed approximately 10 cm, creating a more natural snow cover. This is apparent in Figure 4.16, where the snow cover over the second ridge height (*b*) is a natural drifted snow cover, compared to the first (*a*) and third (*c*) ridge heights. The snow shoveled over each ridge was taken off the surface of the smooth ice outside of the sampling area, and was extremely saline. This was due to snowfall during ice formation and brine expulsion at the surface. This type of snow does not represent snow that would be seen over winter FYI ridges, as dry snow with very little to no salinity content would be expected. Several snow samples were taken across each ridge to examine salinity. For the ridge that was 0.27 m snow was extremely saline, with an average salinity content of 16.3‰, a minimum of 13.9‰, and a maximum of 18.0‰. For the ridge that was 0.48 m some of the snow was saline (the snow shoveled over the ridge) and some had no salinity content (natural snowfall). The average salinity content was 3.5‰, with a minimum of 0‰, and a maximum of 14.2‰. For the ridge that was 0.60 m the snow was much less saline, with an average content of 0.4‰, a minimum of 0‰, and a maximum of 1.2‰. These salinity values must be kept in mind when examining backscatter, as salinity can increase the backscatter coefficient.

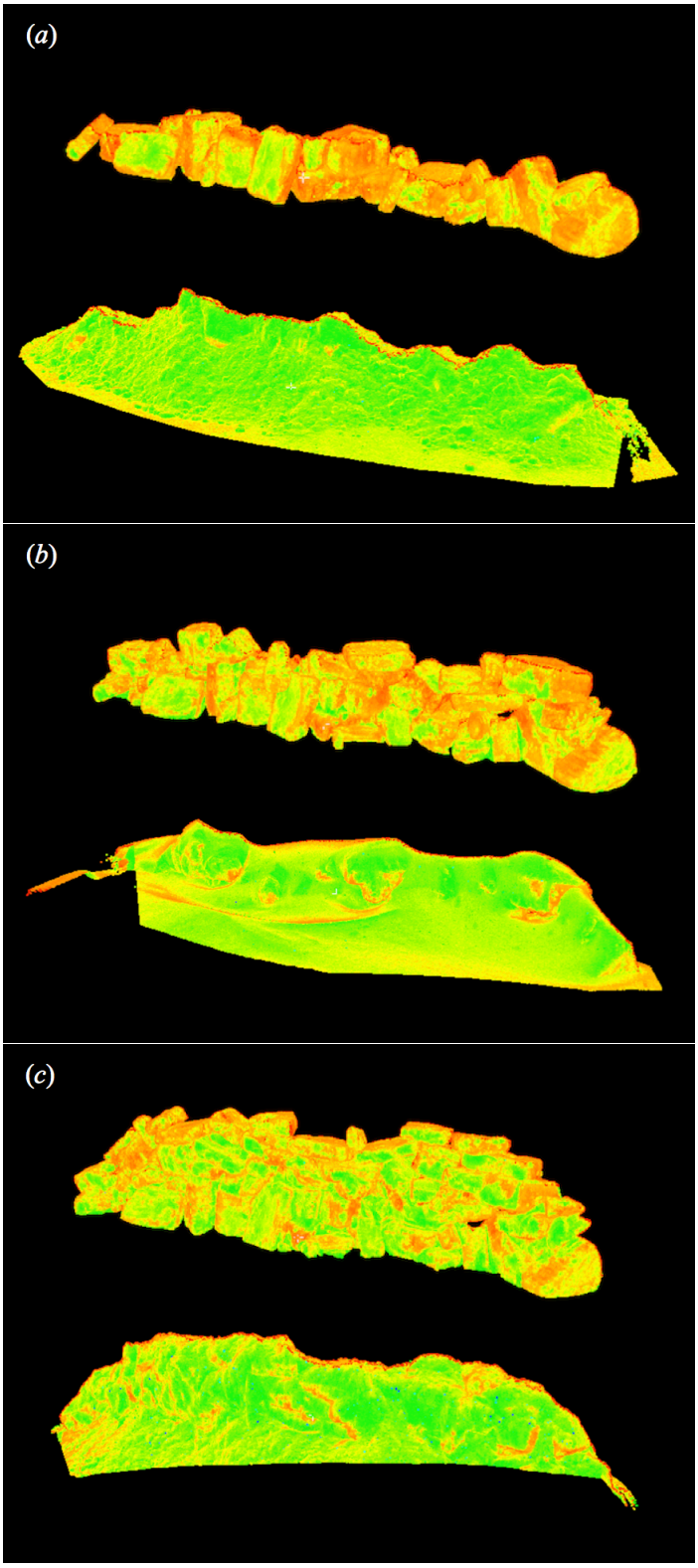

Figure 4.16. Screenshots of the LiDAR point cloud SERF ridges with and without a snow cover for an average ridge height of (*a*) 0.27 m, (*b*) 0.48 m, and (*c*) 0.60 m.

During the SERF study, 58% of the time backscatter increased from a ridge with no snow to a ridge with snow cover, with an average increase of 4.7 dB, a minimum increase of 0 dB, and a maximum increase of 17.9 dB. When backscatter decreased from a bare ice ridge to a snow-covered ridge, it decreased on average 4.1 dB, with a minimum of 0.4 dB, and a maximum of 11.3 dB. When snow versus no snow backscatter was examined for ridges under 0.50 m, backscatter increased 60% of time with an added snow cover, with an average increase of 4.9 dB, while when it decreased it decreased on average 4.0 dB. When snow versus no snow backscatter was examined for ridges under 0.30 m, backscatter increased 83% of the time with an average increase of 5.0 dB, while when it decreased it only decreased on average 1.2 dB. This trend is likely a result of several things. The Chapter 3 finding that backscatter responses become extremely variable once ridges reach a height of ~0.50 m is apparent here. Also, the salinity values were a lot higher with the 0.27 m ridge, which is likely a contributing factor to the fairly consistent increase in backscatter from a bare-ice ridge to a snow-covered ridge at this ridge height. Figure 4.17 shows the backscatter plots for each ridge at each polarization with a 40° incidence angle, with and without a snow cover. For smooth ice and for the 0.27 m ridge, the ridge with snow cover produces higher backscatter, while for the 0.48 and 0.60 m ridges the results are more variable (and in the case of a 40° incidence angle, associated with polarization for this experiment).

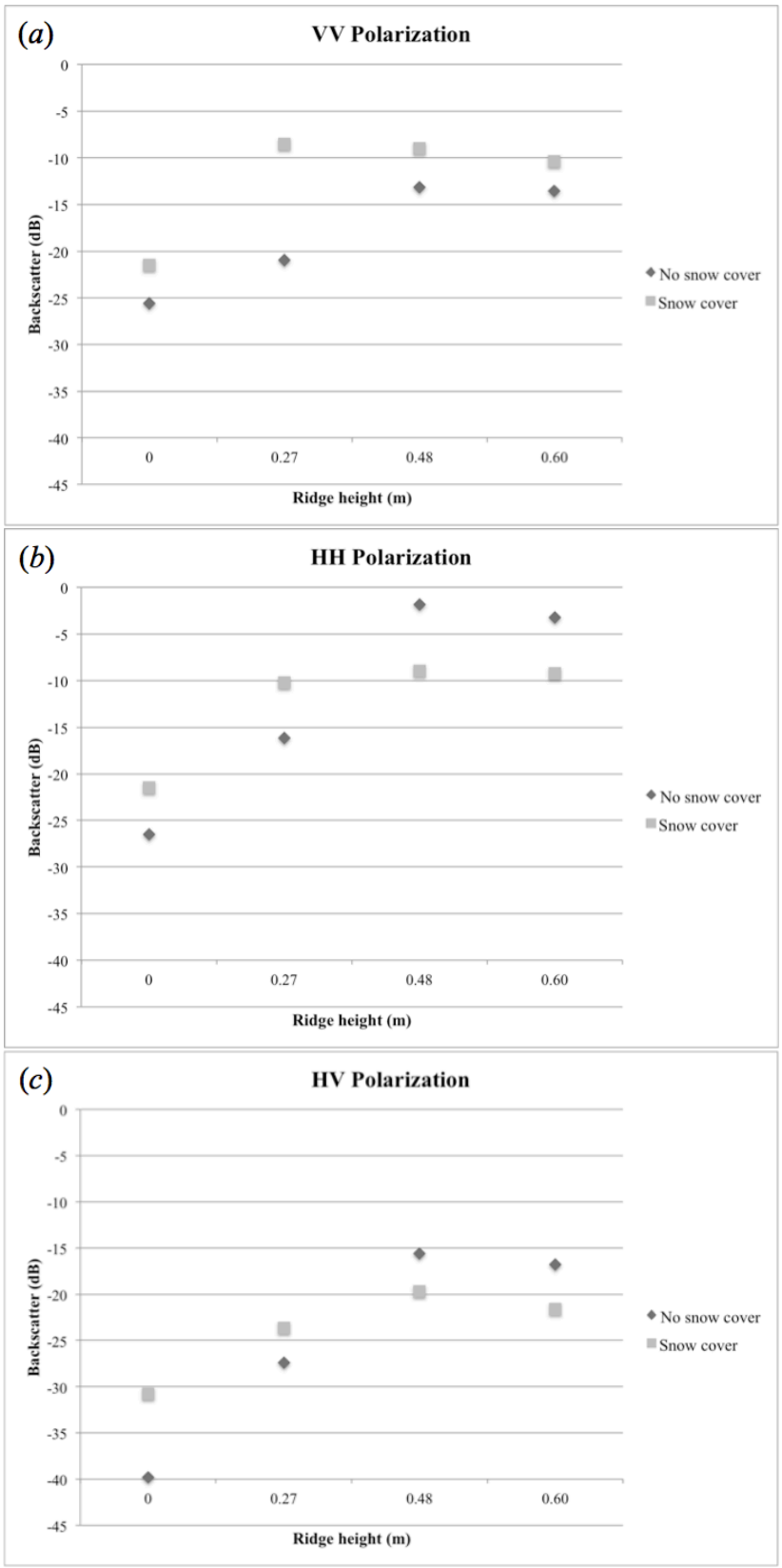

Figure 4.17. The (*a*) VV, (*b*) HH, and (*c*) HV backscatter plots for each ridge height at an incidence angle of 40° for ridges with and without snow cover.

The R-square value produced by the MRA, which is the proportion of variance in backscatter explained by the independent variables (incidence angle, ridge height, polarization, and snow cover), was 0.65. The B value from the regression equation (predicts the dependent variable from the independent variable) for ridge height is significantly greater than the other independent variables, with a value of 26.8, meaning that for this model only ridge height is predicted to significantly change backscatter. The step-wise MRA removed the independent variables incidence angle, polarization, and snow cover, while ridge height remained in the model. When an MRA was run without ridge height as an independent variable to examine how snow cover plays a role in changing backscatter, the R-square value was 0.20, and so the model did not represent a significant proportion of variance in backscatter. Ridge height was the only component extracted during the PCA, meaning that ridge height explains nearly 88% of variability in backscatter when incidence angle, polarization, ridge height, and snow cover are used as independent variables.

The data collected and processed from SERF in February 2014 show that when examining microwave backscatter from a snow layer over a ridge, the salinity and wetness content of the snow plays a significant role. Even though ridge height was the only principal component significant in changing backscatter for this dataset, snow cover still obviously contributes to a change in backscatter between a bare-ice ridge and a snow-covered ridge (as seen in Figure 4.17 when ridge height, incidence angle, and polarization were held constant). Due to the inconsistent snow contents, the results of this study are quite variable, but it is clear that saline snow increases the backscatter

response. In the Arctic, for FYI winter ridges there should be a zero to small increase in backscatter from a ridge with no snow cover to one with a dry snow cover.

4.4 Conclusions

The goal of this chapter was to use data from the May 2014 Dease Strait study, the May and June 2012 Resolute Passage study, and the February 2014 SERF study, to examine how snow cover affects C-band microwave backscatter from FYI ridges, and how different types of snow cover have the potential to change the surface topography and scattering response. A LiDAR laser scanner was used to model surface topography during all three studies, RADARSAT-2 fine beam images were used to examine C-band backscatter during the Resolute Passage study, and a C-Band scatterometer was used to examine backscatter during the SERF study. The RADARSAT-2 sensor and the C-Band scatterometer have many of the same parameters (i.e. comparable frequencies and fully-polarimetric capabilities), allowing for microwave backscatter responses to be comparable between the two instruments. The main conclusions from this chapter are as follows.

The data from the Dease Strait study showed how snow drifts and piles against surface roughness features. In the case of ridges, this drifting of snow is much more pronounced, leading to a significant change in the surface composition (as snow becomes hard and compacted over time due to wind and weathering) and topography of ridged ice areas. Even small amounts of snowfall or snow erosion due to wind events can significantly change the snow cover and the surface topography of a localized area, or

even a large region. If this snow layer contains significant salinity or wetness content, changes to the snow layer have the potential to change microwave backscatter responses.

The data from the Resolute Passage study showed how microwave backscatter responses from areas of ridged ice change temporally due to changes in air temperature, snow cover, surface salinity content, and the wetness content at the surface. Once air temperatures are above freezing significant changes to backscatter occur due to the saline slush layer that forms on the surface. Over the Arctic melt season microwave backscatter will increase over ridged ice.

The data from the SERF study showed how salinity in the snow layer over a ridge has the potential to change the microwave backscatter response. The SERF results also point toward results becoming more variable once a ridge reaches a height of ~0.50 m, but more data is needed to further examine this relationship.

Overall, further data and analysis is needed to examine how a snow cover over a winter FYI ridge has the potential to change microwave backscatter, but it is clear that changes to the snow layer (i.e. snowfall, snow erosion, salinity content, wetness content) has the potential to affect backscatter responses.

Chapter Four References

Armstrong T., Roberts B. and Swithinbank C. (1973). Illustrated glossary of snow and ice. *Scoot Polar Research Institute, University of Cambridge*, 69.

Arons E.M. and Colbeck S.C. (1995). Geometry of heat and mass transfer in dry snow: a review of theory and experiment. *Reviews of Geophysics*, 33 (4): 463–493.

Barber D.G. (2005). Microwave remote sensing, sea ice and arctic climate. *La Physique Au Canada*, 105-111.

Barber D.G., Fung A.K., Grenfell T.C., Nghiem S.V., Onstott R.G., Lytle V.I., Perovich D.K., and Gow A.J. (1998). The role of snow on microwave emission and scattering over first-year sea ice. *IEEE Transactions on Geoscience and Remote Sensing*, 36 (5): 1750-1763.

Barber D.G. and Nghiem S.V. (1999). The role of snow on the thermal dependence of microwave backscatter over sea ice. *Journal of Geophysical Research*, 104 (11): 25789-25803.

Barry R.G. (1996). The parameterization of surface albedo for sea ice and its snow cover. *Progress in Physical Geography*, 20: 63–79.

Beaven S.G., Lockhart G.L., Gogineni S.P., Hosseinmostafa A.R., Jezek K.C., Gow A.J., Perovich D.K., Fung A.K., and Tjuatja S. (1995). Laboratory measurements of radar backscatter from bare and snow-covered saline ice sheets. *International Journal of Remote Sensing*, 15: 851-876.

Carlstrom A. (1995). Modelling microwave backscattering from sea ice for synthetic-aperture radar applications. *Chalmers University of Technology*, Technical Report 271: 1-23.

Carsey F.D., Barry R.G., and Weeks R.F. (1992). Introduction. In: Carsey F.D., Microwave remote sensing of sea ice. *American Geophysical Union*, 1-7.

Crocker G. (1992). Observations of the snowcover on sea ice in the Gulf of Bothnia. *International Journal of Remote Sensing*, 13 (13): 2433–2445.

Curry J.A., Schramm J.L., and Ebert E.E. (1995). Sea ice-albedo climate feedback mechanism. *Journal of Climate*, 8: 240–247.

Eicken H. (2003). Chapter 2: From the microscopic to the macroscopic to the regional scale: Growth, microstructure and properties of sea ice. In: Thomas D.N. and Dieckmann G.S., Sea Ice: An Introduction to its Physics, Biology, Chemistry and Geology, *Blackwell Scientific Limited, London*, 22–81.

Eicken H., Fischer H., and Lemke P. (1995). Effects of the snow cover on Antarctic sea ice and potential modulation of its response to climate change. *Annals of Glaciology*, 21:

369–376.

Fuller M.C., Geldsetzer T., Gill J.P.S., Yackel J.J., and Derksen C. (2014). C-band backscatter from a complexly-layered snow cover on first-year sea ice. *Hydrological Processes*, 28: 4614-4625.

Geiger R. (1957). The climate near the ground. *Harvard University Press, Cambridge, Massachusetts*, 494.

Grenfell T.C. and Lohanick A.W. (1985). Temporal variations of the microwave signatures of sea ice during the late spring and early summer near Mould Bay NWT. *Journal of Geophysical Research,* 90: 5063–5074.

Grenfell T.C. and Maykut G.A. (1977). The optical properties of ice and snow in the Arctic Basin. *Journal of Glaciology, 18*: 445-463.

Guneriussen T. (1997). Backscattering properties of a wet snow cover derived from ERS-1 SAR data. *International Journal of Remote Sensing*, 18 (2): 375-392.

Hudier E. (2006). Low back-scattering bands paralleling pressure ridges on first year sea-ice. *IEEE*, 6: 772-725.

Iacozza J. and Barber D.G. (2010). An examination of snow redistribution over smooth land-fast sea ice. *Hydrological Processes*, 24: 850-865.

Langlois A., Mundy C.J., and Barber D.G. (2007). On the winter evolution of snow thermophysical properties over land-fast first-year sea ice. *Hydrological Processes*, 21: 705-716.

Lubin D. and Massom R. (2006). Polar remote sensing (atmosphere and oceans). *Springer-Praxis Books in Geophysical Science*, 1: 309-616.

Lytle V.I., Jezek K.C., Gogineni S., and Hosseinmostafa R. (1993). Laboratory microwave backscatter from simulated sea ice with a snow cover. *IEEE Transactions on Geoscience Remote Sensing*, 31: 1009–1016.

Maykut G.A. (1978). Energy exchange over young sea ice in the central Arctic. *Journal of Geophysical Research*, 83 (7): 3646-3658.

Maykut G.A. (1982). Large-scale heat exchange and ice production in the Central Arctic. *Journal of Geophysical Research*, 87 (10): 7971–7984.

Maykut G.A. (1986). The surface heat and mass balance. In *The Geophysics of Sea Ice*, Untersteiner N. (ed.). Martinus Nijhoff Publishers: Dordrecht; 395–463.

Nghiem S.V., Kwok R., Yueh S.H., and Drinkwater M.R. (1995). Polarimetric signatures of sea ice 1. Theoretical model. *Journal of Geophysical Research*, 100 (7): 13665-13679.

Onstott R.G. (1992). SAR and scatterometer signatures of sea ice. In: Carsey F.D., Microwave remote sensing of sea ice. *American Geophysical Union*, 73-104.

Petrich C. and Eicken H. (2010). Growth, structure and properties of sea ice. In: Thomas D.N. and Dieckman G.S., Sea ice. *John Wiley and Sons Limited*, (2): 23-77.

Richards J.A. (2009). Remote sensing with imaging radar. *Springer-Verlag Berlin Heidelberg*, 1-320.

Sturm M, Holmgren J., and Perovich D.K. (2002). Winter snow cover on the sea ice of the Arctic Ocean at the Surface Heat Budget of the Arctic Ocean (SHEBA): Temporal evolution and spatial variability. *Journal of Geophysical Research*, 107 (10): 23 - 1-23 - 17.

Winebrenner D.P., Nelson E.D., Colony R., and West R.D. (1994) Observation of melt onset on multi year Arctic sea ice using the ERS-1 synthetic aperture radar. *Journal of Geophysical Research,* 99 (22): 425–441.

Chapter Five – Conclusions and Recommendations

5.1 Summary

This M.Sc. thesis presented unique ridged sea ice microwave remote sensing data collected at a sea ice mesocosm. The primary goal of the thesis was to better understand *in situ* C-band microwave scattering from first-year sea ice (FYI) ridges during winter, and to examine how C-band backscatter can vary with changes to radar and target parameters. The research objectives were (1) to examine the relative contribution of C-band microwave scatterometer parameters (incidence angle, and linear and polarimetric parameters) relative to variable target parameters (ridge height, surface roughness, slope values, approximate air space volumes in bare ice ridges, and snow cover) on the overall backscatter of first-year ridged sea ice; and (2) to determine the optimal backscatter parameter, incidence angle, and polarization, for identifying ridged ice from smooth ice, and for detecting variations in ridge height.

Chapter one provided an introduction to remote sensing in the Arctic and rationale for why a better understanding of scattering from ridges is necessary. Chapter two provided essential background and contextual information on FYI thermodynamic and dynamic processes, ice roughness measurements, thesis instrumentation, and microwave remote sensing. Chapter three addressed thesis objectives (1) and (2) over non-snow covered ridges, and chapter four addressed parts of thesis objective (1) over snow-covered ridges.

5.2 Results

Results from chapter three shows that a significant proportion of the variance in the C-band backscatter responses comes from the incidence angle, ridge height, and polarization parameters. Statistical analysis showed that ridge height was the only principal component extracted for each Sea-ice Environmental Research Facility (SERF) experiment, as well as all of the experiments combined, meaning that ridge height explains nearly 88% of variability in backscatter when incidence angle, polarization, and ridge height are used as independent variables. When different polarimetric (VV/HH, HV/HH, VV-HH phase difference, and depolarization ratio) and non-polarimetric (total power) parameters are used as the output variable, ridge height is still the only principal component extracted. The backscatter signal consistently increased on average 15.3 dB from a smooth ice surface up to an average ridge height of ~0.50 m 80% of the time during the three SERF experiments. Once the ridge heights were greater than ~0.50 m the backscatter returns were more variable, likely due to the increased amount of randomly oriented surfaces, the greater potential for volume scattering, and an increasingly filled radar field of view.

Analysis from chapter three further shows that when using a radar incidence angle range of 20 to 60°, there is a slight decreasing trend in the backscatter coefficient as incidence angle increases. When the average change in backscatter between ridge heights was examined there were similar values in backscatter change for each polarization, which suggests that as long as polarization is held constant, or all polarizations are examined, polarization is likely not a significant contributing parameter to changing backscatter values in the case of ridges (strong volume scatterers such as

ridges generally show no preferential scattering based on polarization). Results show that using an incidence angle between 30 and 50° with HV polarization will best enable distinguishing between smooth and ridged ice, while using an incidence angle of 40° with HV or HH polarization will best enable detecting variations in ridge height.

Analysis from chapter four shows that snow drifts and piles against surface roughness features, and in the case of ridges, this drifting of snow is much more pronounced, which leads to a significant change in the surface topography and composition of ridged ice areas. Results and contextual information show that microwave backscatter responses from areas of ridged ice change temporally due to changes in air temperature, snow cover, surface salinity content, and the wetness content at the surface. Once air temperatures reach above freezing, significant changes to backscatter occur due to the saline slush layer that forms on the surface. Over the Arctic melt season microwave backscatter will increase over ridged ice due to increasing wetness and salinity content at the surface.

Overall thesis results show that high-resolution terrestrial LiDAR models can be used to precisely model snow and sea ice surfaces, as well as measure ridge heights relative to freeboard, ridge volume estimates, macro and micro-scale surface roughness, slope angles of sail blocks, and general slopes of ridges. When examining sea ice ridges in cold temperatures with no snow cover for this study, 69% of the variance in the backscatter responses can be explained by incidence angle, polarization, and ridge height, with almost 88% of the variability in the backscatter attributed to ridge height. Ridge height is the significant parameter affecting C-band microwave scattering for snow-free FYI ridges during winter. Further data and analysis is needed to examine how a snow

cover over a winter FYI ridge has the potential to change microwave backscatter, but it is clear that changes to the snow layer (i.e. snowfall, snow erosion, salinity content, wetness content) will affect backscatter responses. Results from this M.Sc. thesis provide new *in situ* information on FYI ridges that could be scaled to satellite resolution for use in ridge detection and monitoring.

5.3 Recommendations

Studying areas of ridging *in situ* in the Arctic is prohibited by a number of factors, while using microwave remote sensing to examine ridges provides a time and cost-effective way to collect data. This thesis provides a baseline understanding of some of the changes to microwave C-band backscatter when radar and target parameters are changed, however there is a need for further experimentation to better understand areas of ridging as the Arctic Ocean moves to a predominantly FYI pack. The main recommendations for further research coming out of this thesis are; (1) Continued mesocosm or on-ice ridge studies that examine the relative contribution of other radar and target parameters, such as frequency (P or L-band), surface temperature, surface salinity, and the dielectric properties at the surface, to microwave backscatter. Also, a further examination of how different snow covers over ridges affects backscatter is needed; (2) A dedicated diurnal Arctic melt season study that examines backscatter from FYI ridges throughout the entire melt season (from the cold season to ice breakup). This would provide a detailed base of knowledge on how air and surface temperatures, and the wetness and salinity content at the surface affect backscatter; and (3) Acquire coincidental synthetic aperture radar (SAR) imagery with each *in situ* dataset collection

to compare scattering coefficient results at the pixel resolution, with the backscatter coefficient collected *in situ*. From this, a method should be developed to acquire specific ridge information (i.e. approximate ridge height) from SAR imagery with no *in situ* datasets.

The rapidly occurring changes to Arctic sea ice, and the increased potential for ridged ice features deemed hazardous to navigation and exploration has increased the need for a better understanding of ridge features in microwave remote sensing data. A better understanding of ridge features, and the ability to detect ridge parameters in SAR imagery would provide easily accessible ways to identify and monitor ridges for navigation, exploration and scientific purposes. These suggested recommendations for further research would significantly add to the current knowledge base of FYI ridge scattering.